UNIVERSITAT POLITÈCNICA DE CATALUNYA BARCELONATECH

Development of a high intensity Mid-Ir OPCPA pumped by a HO:YLF amplifier

Daniel A. Sánchez Peacham

DEVELOPMENT OF A HIGH INTENSITY MID-IR OPCPA PUMPED BY A HO:YLF AMPLIFIER

a dissertation submitted in partial fulfilment of the requirements for the degree of Doctor of Philosophy

Author: Daniel A. Sánchez Peacham

Thesis advisor: Prof. Dr. Jens Biegert

ICFO - Institut de Ciències Fotòniques

UPC - Universitat Politècnica de Catalunya

PUBLICATIONS

- **D. Sánchez**, M. Hemmer, M. Baudisch, S. L. Cousin, K. Zawilski, P. Schunemann, O. Chalus, C. Simon-Boisson, and J. Biegert, "7 μm, ultrafast, sub-millijoule-level mid-infrared optical parametric chirped pulse amplifier pumped at 2 μm," Optica **3**, 147-150 (2016).

- I. Pupeza, **D. Sánchez**, J. Zhang, N. Lilienfein, M. Seidel, N. Karpowicz, T. Paasch-Colberg, I. Znakovskaya, M. Pescher, W. Schweinberger, V. Pervak, E. Fill, O. Pronin, Z. Wei, F. Krausz, A. Apolonski, and J. Biegert, "High-power sub-two-cycle mid-infrared pulses at 100 MHz repetition rate," Nat. Photonics **9**, 721 (2015).

- H. Pires, M. Baudisch, **D. Sánchez**, M. Hemmer, J. Biegert, "Ultrashort pulse generation in the mid-IR," Prog. in Quant. Electr. **43**, 130 (2015).

- M. Hemmer, **D. Sánchez**, M. Jelínek, Vadim Smirnov, H. Jelinkova, V. Kubecek, and J. Biegert, "2 μm wavelength, high-energy Ho:YLF chirped-pulse amplifier for mid-infrared OPCPA," Opt. Lett. **40**, 451-454 (2015).

- **D. Sánchez**, M. Hemmer, M. Baudisch, K. Zawilski, P. Schunemann, H. Hoogland, R. Holzwarth, and Jens Biegert, "Broadband mid-IR frequency comb with $CdSiP_2$ and $AgGaS_2$ from an Er,Tm:Ho fiber laser," Opt. Lett. **39**(24) 6883 (2014).

- H. Hoogland, A. Thai, **D. Sánchez**, S. L. Cousin, M. Hemmer, M. Engelbrecht, J. Biegert, and R. Holzwarth, "All-PM coherent 2.05 μm Thulium/Holmium fiber frequency comb source at 100 MHz with up to 0.5 W average power and pulse duration down to 135 fs," Opt. Express **21**, 31390-31394 (2013).

CONTENTS

LIST OF FIGURES

LIST OF TABLES

1

INTRODUCTION

It is hard to overstate the impact the laser has had on experimental science. It would be no exaggeration to say that over the last 50 years, the study and control of light-matter interactions has been largely driven by developments in laser science and technology. The invention of the laser [1, 2, 3] provided unprecedented control over the generation of light, completely transforming science and technology, from experimental optics to the natural sciences. It also enabled the generation of electromagnetic fields intense enough to be comparable to the forces binding electrons to the atom, which quickly lead to the first observation of nonlinear optical phenomena just one year after the first laser was demonstrated [4]. As laser technology has advanced over the years, light sources producing a vast range of optical fields in terms of wavelength, energy, pulse duration, etc, have become readily available for science and industry and opened up uncountable avenues for research. Famously described by skeptics as a "solution looking for a problem", Maiman's pioneering ruby laser marked the starting point of a development race that quickly put the laser at the centre of multiple fields, to the extent that frequently scientific progress has run parallel to advances in laser technology. Thus the ongoing development of laser science is currently being driven by the increasingly demanding requirements of novel experimental techniques. It is fair to say that there are now many research areas with "problems looking for a solution".

I would argue that strong-field physics is one such area. This field is concerned with the interaction between matter and ultra-intense electromagnetic fields. Experimental investigations into strong-field

phenomena strongly rely on advances in state-of-the-art laser technology. Currently the main area of activity in strong-field physics relates to processes associated with the recollision of electrons after ionisation under the influence of intense laser light. These processes include high-harmonic generation (HHG), above threshold ionisation and laser induced electron diffraction (LIED) to name a few [5, 6, 7]. Among these strong-field processes, HHG is of particular interest since it is a key technique in the closely related field of attoscience, which involves the study of phenomena on the sub-femtosecond time scale. The central experimental tool in this field are optical pulses with attosecond pulse durations (10^{-18} s). These pulses, with carrier frequencies corresponding to extreme ultraviolet and x-Ray wavelengths, are produced by up-converting radiation from the near-IR through HHG [8]. At present, there is no other experimentally verified technique to generate attosecond pulses.

Strong-field physics is currently undergoing a shift towards mid-IR driving lasers (2 μm < λ < 20 μm) [9]. Employing long wavelength driving laser systems presents several advantages over standard 0.8 μm sources based on Ti:sapphire. The impact of the driving wavelength on strong-field processes can be illustrated using the semiclassical recollision model [10]. This model explains the main properties of strong-field recollision using a three step process. In a first step, an applied electric field causes a bound electron to tunnel-ionise from the atom. Next, classical mechanics is used to trace the trajectory of the electron as it is accelerated by an oscillating electric field. Finally, the electron recollides with the parent ion. This model predicts that the maximum return energy is $E_r = 3.17\,U_p$, where $U_p \propto \lambda^2\, I$ is the ponderomotive energy, and I and λ are the intensity and wavelength of the driving electric field. The recollision of the electron with the parent ion can lead to several processes, including elastic and inelastic scattering off the parent ion. Another possible outcome is the recombination of the electron and the ion which can lead to emission of light via HHG. The energy emitted upon recollision is given by the ionisation potential I_p of the atom plus the return energy E_r of the free electron in the laser field. The maximum frequency of the emitted photon is:

$$\nu_c = \frac{I_p + 3.17U_p}{h}, \tag{1}$$

where ν_c is the cut-off frequency of HHG.

Since the range of I_p values is limited, Eq. 1 implies that extending the cut-off frequency of HHG requires increasing U_p. In principle this can be done by either increasing the intensity of the laser field or scaling the interaction to longer wavelengths. In practice the former is limited by strong-field ionisation: as soon as a significant fraction of the atoms are ionised the conversion efficiency of the process decreases dramatically due to nonlinear effects such as plasma induced dispersion and depletion of the atomic levels contributing to the HHG process. Wavelength scaling on the other hand has shown to be a feasible approach to extend the cut-off both theoretically [11, 12, 13] and experimentally [14, 15]. Theoretical work has even proposed the possibility of obtaining sub-attosecond duration waveforms and photon energies higher than 10 keV using long wavelength laser pulses to drive HHG [16, 17].

The shift in strong-field experiments toward longer wavelengths may lead to unexplored physics beyond HHG. This includes such exotic phenomena as the direct reshaping of the carrier field [18], scaling of quantum path dynamics [19], the breakdown of the dipole approximation [20] and dielectric laser acceleration [21]. The Attoscience and Ultrafast Optics (AUO) group at the Institute of Photonic Sciences (ICFO) has pioneered the field of ultrafast mid-IR laser sources and applications. The development of novel mid-IR sources has enabled milestone experimental work such as the extension of HHG into the X-ray water-window [22, 23, 24, 25] and the use of the LIED technique to image the structure of molecules and track dynamic changes during bond-breaking processes [26, 27, 28].

The demand for new laser systems providing intense laser pulses at long wavelengths presents a serious challenge, as conventional laser sources are unsuited for this and the development of novel techniques and materials are required. Nevertheless, the last decade has seen tremendous advances in the development of such lasers. Optical

parametric chirped pulse amplification (OPCPA) has established itself as the most promising architecture due to its inherent flexibility in operating wavelength and peak power scalability. The demonstration in the late 2000s of the first mid-IR OPCPAs represented a milestone in the development of long wavelength high intensity lasers [29, 30]. These systems relied on parametric processes to generate and amplify few-cycle duration pulses at 3 μm using high-repetition rate 1 μm pump lasers. Over the subsequent decade, 3 μm OPCPAs have experienced numerous developments [31, 32, 33, 34] and have become an indispensable tool for mid-IR strong-field experiments. However, the use of 1 μm lasers as pump source sets an inherent limit to the scalability of these systems to longer wavelengths.

The next generation of mid-IR OPCPAs has overcome this limitation with the development of 2 μm wavelength pump lasers, enabling the demonstration of OPCPA at wavelengths longer than 4 μm. The system presented in this thesis was the first demonstration of this novel approach and is currently the longest wavelength OPCPA with an operating wavelength of 7 μm [35]. In addition, the pump laser exhibits the highest energy of any 2 μm picosecond source. The current output parameters of the laser are 0.7 mJ pulse energy at 188 fs duration with an available pump energy of 220 mJ at a repetition rate of 100 Hz [36]. Since our first demonstration of 2 μm pumped OPCPA in 2016, two other systems using a similar architecture have been reported [37, 38]. The laser system described in [37] delivers 100 fs, 40 μJ CEP stable pulses at a centre wavelength of 5.2 μm. The pump source is a Ho:YAG based chirped pulse amplifier (CPA) delivering up to 3 mJ of pulse energy at 1 kHz repetition rate. In [38], the authors report an impressive 80 fs pulse duration at 5 μm with an energy of 1 mJ. The pump laser is a Ho:YLF CPA operating at 1 kHz and delivering up to 50 mJ of pulse energy. In comparison to our OPCPA, these lasers operate at a higher repetition rate and exhibit a shorter pulse duration, but at shorter centre wavelength. The main drawback of the system described in [37] is the low available pump energy, limiting the peak power scalability of the output. While the system described in [38] does have sufficient pump energy for peak power scaling, the architecture is inherently incompatible with CEP stability, thus limiting the usefulness of this source for strong-field

experiments.

The topic of this thesis is the development of a long wavelength pumped, mid-IR OPCPA. Our aim is to show the feasibility of this concept for generating high intensity pulses in the mid-IR, overcoming many of the drawbacks limiting other approaches. This work includes the development of two novel sub-systems: a seeder generating broadband, mid-IR pulses with a bandwidth supporting a few-cycle pulse duration and high energy, picosecond long wavelength laser suitable for pumping mid-IR optical parametric amplifiers (OPA). The thesis is organised as follows. The theoretical concepts required to develop an OPCPA are discussed in **Chapter 2**. Basic notions of nonlinear optics are given, with special emphasis on three-wave mixing processes. The development of the seed source is the topic of **Chapter 3**. The seed source consists of two sub-systems. The first is a fibre laser which constitutes the front-end of the OPCPA. The second sub-system is a difference frequency generation (DFG) stage, which generates the seed pulses for the OPA line. A review of nonlinear crystals for mid-IR application is presented. The design and implementation of a 2 μm wavelength, high energy pump source is shown in **Chapter 4**. The available laser gain media for high energy, picosecond operation at 2 μm wavelength are discussed. **Chapter 5** is dedicated to the parametric amplifier stages and dispersion management of the OPCPA. The 7 μm OPA line and stretcher/compressor assemblies are discussed. The characterisation of the final output of the OPCPA is presented. A brief summary of the main results and future work is given in **Chapter 6**.

The author would like to acknowledge the following contributions to the work presented in this thesis. Dr. H. Hoogland and A. Thai designed and built the fibre laser described in Chapter 3. Dr. M. Hemmer and the author characterised the laser and developed the compressor for the 2 μm broadband output. The author designed the mid-IR DFG stage described in Chapter 3. The experimental work was undertaken by Dr. M. Hemmer and the author. Dr. M. Hemmer designed the regenerative amplifier and single-pass booster described in Chapter 4. The experimental work was undertaken mainly by Dr. M. Hemmer with some assistance from Dr. M. Jelínek and the author.

The multi-pass amplifier described in Chapter 2 was designed by the author. The experimental work was undertaken mainly by the author, with some assistance from Dr. G. Matras and Dr. T. Kanai. Finally, the author designed the OPA stages and compressor presented in Chapter 5. The experimental work was carried out mainly by the author, with some assistance from Dr. M. Hemmer and U. Elu.

2

THEORETICAL CONCEPTS FOR OPCPA

The theoretical formulation used to describe parametric processes was developed shortly after the first demonstration of nonlinear optical phenomena [39, 4]. Understanding the physical processes involved is crucial to enable optimum design of a laser source based on nonlinear processes. This is of particular importance for complex, multi-stage architecture such as OPCPA, where the experimental parameter space is large. Multiple design aspects of the system, including thickness and optical properties of the nonlinear media, intensity, polarisation and direction of the interacting beams, etc., need to be chosen carefully for several stages in the laser system involving nonlinear processes. This chapter deals with the basic theoretical notions required for the development of an OPCPA. Most of the concepts presented here are well known from nonlinear optical theory and the full mathematical details can be found in standard optics text books [40, 41]. The aim is to focus on the aspects that are most relevant to the development of the laser system presented in this thesis.

The chapter is organised as follows. The basic model describing perturbative nonlinear phenomena based on the nonlinear polarisation is presented. The coupled differential equations used to model DFG are given. Based on these equations, the intensity and phase evolution in DFG and OPA are presented and the impact on laser design is discussed. Next, the concept of phase-matching is presented. Finally, the generation and control of the carrier-to-envelope phase (CEP) of an ultrashort pulse is discussed.

2.1 THE NONLINEAR POLARISATION

The simplest model to account for a pulse propagating through a material is one in which an external electric field instantaneously rearranges the charge distribution in the material. Macroscopically, this is described by the electric polarisation $\vec{P}$, which is the average induced dipole moment per unit volume. For weak fields, the charge distribution around the atom will follow the applied electric field such that a linear dependency is established between the induced dipole moment and the applied field, meaning that the atoms will oscillate and radiate at the same frequency as the applied field. For stronger fields however, the response of the system can be more complex and the effects of a nonlinear dependency need to be accounted for. Classical nonlinear optics generally deals with fields that are strong enough for nonlinear effects to be observable but weak enough that photoionisation or other strong-field processes are negligible. In this intermediate regime, we expect the relation between $\vec{P}$ and $\vec{E}$ to be linear for small values of $\vec{E}$, and to deviate from linearity for larger values. This can be expressed by expanding $\vec{P}$ as a Taylor series. Assuming that the medium is isotropic and the response to the applied field is instantaneous, the polarisation can be written as:

$$\vec{P}(t) = \epsilon_0 \chi^{(1)} \vec{E}(t) + \epsilon_0 \chi^{(2)} \vec{E}^2(t) + \epsilon_0 \chi^{(3)} \vec{E}^3(t) + \cdots , \qquad (2)$$

where the proportionality between the electric field and the polarisation is the scalar susceptibility $\chi^{(n)}$ times the vacuum permittivity ϵ_0. For anisotropic media, the tensor nature of $\chi^{(n)}$ needs to be accounted for. $\chi^{(1)}$ is the linear susceptibility which describes the linear response of the medium, while $\chi^{(2)}, \chi^{(3)}$ and so on, represent the higher order susceptibilities which characterise the nonlinear response.

Equation (2) gives some insight into fundamental nonlinear optical phenomena. Consider the simple case of two plane waves oscillating at ω_1 and ω_2 with amplitudes $E_1 = 1$ and $E_2 = 1$ and $\omega_1 > \omega_2$. The total electric field can be written as the superposition of the two plane waves:

$$E_{sum}(t) = e^{-i\omega_1 t} + e^{-i\omega_2 t} + c.c.\,, \tag{3}$$

where c.c. is the complex conjugate and scalar fields are considered for simplicity. For strong enough fields, the nonlinear polarisation induced as the waves propagate through the medium needs to be taken into account. The lowest order nonlinear term is the second-order polarisation, which can be calculated using Eq. (2):

$$\begin{aligned} P^{(2)}(t) &= \epsilon_0 \chi^{(2)} (E_{sum}(t))^2 \\ &= \epsilon_0 \chi^{(2)} \left[e^{-2i\omega_1 t} + e^{-2i\omega_2 t} + 2e^{-i(\omega_1-\omega_2)t} + 2e^{-i(\omega_1+\omega_2)t} + \cdots \right]. \end{aligned} \tag{4}$$

This simple calculation accounting only for the lowest order nonlinear processes, shows that two propagating plane waves can induce a polarisation oscillating at new frequencies in a nonlinear medium. As we will show, the nonlinear polarisation behaves as a source term in the optical wave equation, leading to the generation of new waves oscillating at different frequencies from the driving fields. The generation of the new frequencies $2\omega_1$ and $2\omega_2$, $\omega_1 + \omega_2$ and $\omega_1 - \omega_2$ are known as second harmonic generation (SHG), sum frequency generation (SFG) and DFG respectively. By convention, the indices typically used in the context of DFG are $\omega_1 = \omega_p$ (for pump), $\omega_2 = \omega_s$ (for signal) and $\omega_1 - \omega_2 = \omega_i$ (for idler). This notation is used throughout this thesis.

These nonlinear processes are referred to as three-wave mixing processes. The generation of new frequencies automatically satisfies energy conservation via $\hbar\omega_1 = \hbar\omega_2 + \hbar\omega_3$ (assuming that $\omega_1 > \omega_2 > \omega_3$). Momentum conservation on the other hand is not fulfilled as, in general, $\hbar\vec{k_1} = \hbar\vec{k_2} + \hbar\vec{k_3}$ is not satisfied. As we will show, momentum conservation is related to the efficiency of the nonlinear process.

2.2 THE COUPLED WAVE EQUATION FOR DFG

As discussed in the previous section, DFG is a second-order $\chi^{(2)}$ three-wave mixing process in which two optical fields oscillating at $\omega_p > \omega_s$ are combined in a nonlinear medium to generate a third field oscillating at a lower frequency $\omega_i = \omega_p - \omega_s$. In order to study how the three waves interact and evolve as they propagate in the nonlinear medium, a wave equation containing a nonlinear term is used:

$$\nabla^2 \vec{E} - \frac{1}{c^2}\partial_t^2 \epsilon_r \vec{E} = \frac{1}{\epsilon_0 c^2}\partial_t^2 \vec{P}^{NL}\,, \tag{5}$$

where ϵ_r is the relative permittivity of the nonlinear medium, defined as $\epsilon_r = \chi^{(1)} + 1$, c is the vacuum speed of light and $\vec{P}^{NL}$ is the nonlinear part of the polarisation such that $\vec{P} = \vec{P}^{L} + \vec{P}^{NL} = \epsilon_0 \chi^{(1)} \vec{E} + \vec{P}^{NL}$. Equation 5 is referred to as the nonlinear wave equation and it is derived from Maxwell's equations by adding a source term in the form of the nonlinear polarisation. Note that due to the linearity of this equation, each frequency component in the nonlinear polarisation acts as a source for the corresponding frequency components in the optical field, which must satisfy the wave equation independently.

For a negligible nonlinear polarisation, the nonlinear wave equation takes a homogenous infinite plane wave as a solution. A reasonable trial solution for the full nonlinear equation is an infinite plane wave, but allowing the amplitude to vary with propagation. We can assume that the wave is linearly polarised and propagating in the z-direction such that Eq. 5 can be treated as a scalar equation. The electric field can be written as $E(z,t) = A(z)e^{i(kz-\omega t)} + c.c$, where the wavevector is defined as $k = n\omega/c$ in order to satisfy the wave equation, and the linear refractive index n is related to the susceptibility by $n^2 = 1 + \chi^{(1)}$. For simplicity, we consider only the polarisation term contributing to DFG. Using Eq. (2) the polarisation oscillating at the idler frequency can also be written as a plane wave $P_i(z,t) = B_i e^{-i(\omega_i t)} + c.c$. As can be deduced from Eq. (2), the amplitude of the polarisation at the idler frequency B_i, will depend on the amplitude of the pump and signal fields, A_p and A_s:

$$B_i = 4\epsilon_0 d_{eff} A_p A_s^* e^{i(k_p - k_s)z}\,, \tag{6}$$

where we have introduced d_{eff} which is the effective nonlinear coefficient defined as $d_{eff} = \chi_{eff}/2$ where χ_{eff} is the scalar value of the second-order nonlinear susceptibility for a given polarisation and propagation direction.

Once the idler field E_i and the idler polarisation P_i have been defined they can be introduced into the the nonlinear wave equation, which will account for all waves oscillating at ω_i. A further approximation is often used at this point which consists of neglecting the term containing the second derivative on the left hand side of the Eq. 5. This approximation is known as the slowly varying amplitude approximation and is equivalent to assuming that the amplitude term A_i varies little over a distance comparable to the optical cycle. This is a reasonable approximation given that the energy transfer between the fields is usually only relevant after a propagation much longer than an optical cycle. The resulting differential equation becomes:

$$\frac{dA_i}{dz} = i\frac{2d_{eff}\omega_i^2}{k_i c^2} A_p A_s^* e^{i\Delta k z}\,, \tag{7}$$

where the term $\Delta k = k_p - k_s - k_i$, known as phase mismatch, has been introduced. Analogous equations can be obtained for the pump and signal fields:

$$\frac{dA_p}{dz} = i\frac{2d_{eff}\omega_p^2}{k_p c^2} A_s A_i e^{-i\Delta k z} \tag{8a}$$

$$\frac{dA_s}{dz} = i\frac{2d_{eff}\omega_s^2}{k_s c^2} A_i^* A_p e^{i\Delta k z}\,. \tag{8b}$$

Solving the coupled wave equations (7) and (8) for the appropriate boundary conditions will yield the evolution of the fields during the nonlinear interaction. Without any further assumptions, Eq. (7) and (8) are typically solved numerically. However, in many practical cases there are orders of magnitude of difference in the amplitude of the three interacting waves and simplifying assumptions can be made. Note that Eq. (7) and (8) neglects to account for numerous

effects that are crucial in an actual experimental setting, particularly for ultrashort pulses. These effects include the difference in group velocities between the interacting waves, pulse broadening due to dispersion and spatial walk-off due to birefringence in the nonlinear medium. Nevertheless, useful physical insight can be drawn from these equations for the two nonlinear processes that are central to this thesis: DFG and OPA. These are physically the same nonlinear process described by the same set of equations, but with different boundary conditions. DFG is employed in Chapter 3 as a means of generating broadband mid-IR pulses. OPA underlies the amplification scheme of the OPCPA described in Chapter 5.

2.2.1 *Intensity evolution*

In an experimental DFG setup, the pump and signal typically have comparable intensities. In addition, in many cases the conversion efficiency is low enough that there is no appreciable depletion of the input pulses. Therefore a reasonable assumption for simplifying the coupled wave equations is that the amplitude of the signal and pump fields are constant throughout the nonlinear process while the initial idler amplitude is zero. In this case the amplitude of the idler field at an arbitrary propagation length z can easily be found by integrating Eq. (7). The intensity can be calculate from the amplitude using: $I = 2n\epsilon_0 c|A|^2$. The intensity of the idler after a propagation distance z can be computed using:

$$I_i(z) = I_p I_s \left(\frac{2d_{eff}\omega_i z}{k_i c^2} \right)^2 \mathrm{sinc}^2\left(\frac{\Delta k z}{2}\right). \tag{9}$$

This expression gives some useful insight. The first terms are the pump and signal peak intensities, reflecting the fact that DFG is driven by the intensity of the input fields. The terms inside the parenthesis take into account the properties of the nonlinear medium. Importantly, this terms shows that the idler intensity is proportional to the square of both d_{eff} and the propagation distance z, highlighting the importance of the length and nonlinearity of the nonlinear medium. Finally, the modulating sinc^2 dependency accounts for the

difference in phase velocity of the interacting waves through the phase mismatch Δk. Specifically, the term Δkz quantifies the accumulated phase mismatch after a given propagation length. Ensuring that the phase relation between the interacting waves minimises Δk is known as phase-matching. In the case of perfect phase-matching, $\Delta k = 0$, the sinc function has a value of 1, and in this case the idler intensity is a quadratic function of propagation distance. For $\Delta k \neq 0$ however, there is decrease in efficiency as the sinc functions drops for increasing values of Δk down to zero at $\Delta kz/2 = \pi$, and then oscillates around decreasingly small values. The experimental techniques used to achieve phase-matching are discussed in the following section.

OPA can be viewed as a special case of DFG in which a strong pump is used to amplify a weaker seed wave, which can either be the idler or the signal. In this scenario, reasonable assumptions allowing a solution to the wave equations are that the pump field is undepleted, that the idler and signal field amplitudes are low in comparison to the pump throughout the interaction and that either the idler or signal amplitude are zero at the input. These assumption are useful for describing the initial stages of amplification where the intensity of the pump is several orders of magnitude higher than the seed. Typically, in the last amplifier stages of an OPCPA the pump and seed intensities become comparable and pump depletion cannot be neglected. Using these assumptions, and taking the idler as zero at the input, the idler and signal intensities evolve according to [42]:

$$I_i(z) = I_s(0)\frac{\omega_i}{\omega_s}\frac{\Gamma^2}{g^2}\sinh^2(zg)\,, \tag{10a}$$

$$I_s(z) = I_s(0)\left(1 + \frac{\Gamma^2}{g^2}\sinh^2(zg)\right) \tag{10b}$$

where g is the parametric gain, given by $g = \sqrt{\Gamma^2 - (\Delta k/2)^2}$, Γ is the gain coefficient:

$$\Gamma^2 = d_{eff}^2 \frac{2\omega_s\omega_i I_p}{c^3\epsilon_0 n_p n_s n_i}\,, \tag{11}$$

and n_p, n_s and n_i refers to the refractive index at the pump, signal and idler wavelengths.

Note that in this case, the gain depends only on the pump and not on the signal intensity, pointing to the relevance of pump intensity in OPA performance. In addition, this dependency implies that fluctuations in the shot-to-shot pump energy will have a large impact on output stability. Similarly to the equation given for intensity evolution in DFG, these results also highlight the importance of the nonlinearity d_{eff} and the propagation distance z.

2.2.2 *Phase evolution*

As mentioned, the relative phase ϕ between the interacting waves affects parametric gain. The evolution of the phase of the interacting waves in DFG is given by a set of equations analogous to the coupled wave equations for amplitude [43]. The equations show that the highest conversion efficiency from the pump to the signal and idler fields is achieved when the phase between the three waves is $\phi = \Phi_p - \Phi_s - \Phi_i = -\pi/2$, where Φ_p, Φ_s and Φ_i are the phase of the pump, signal and idler waves. For increasing values of ϕ the efficiency of the process is reduced until reaching $\phi = 0$ when back-conversion occurs and energy is transferred from the idler and signal back to the pump field.

In most DFG and OPA schemes, only two waves are present at the start of the nonlinear process. Assuming that the seeded wave is the signal and that the initial idler field is zero, the phase of the generated wave at $z = 0$ takes the initial value $\Phi_i = \Phi_p - \Phi_s + \pi/2$, which maximises the parametric gain. However as the waves propagate in the medium, the three phases evolve according to [43]:

$$\Phi_i(z) = \Phi_p(0) - \Phi_s(0) + \frac{\pi}{2} - \frac{\Delta k z}{2} \tag{12}$$

$$\Phi_s(z) = \Phi_s(0) - \frac{\Delta k z}{2} + \frac{\Delta k \gamma_s^2}{2} \int \frac{dz}{f + \gamma_s^2} \tag{13}$$

$$\Phi_p(z) = \Phi_p(0) - \frac{\Delta k z}{2} \int \frac{f dz}{1-f}, \tag{14}$$

where f is the fractional pump depletion $f = 1 - I_p(z)/I_p(0)$ and γ_s is the ratio between the signal and pump intensity at $z = 0$, $\gamma_s = \omega_p I_s(0)/\omega_s I_p(0)$. Note that identical equations can be derived assuming that the idler is the seeded wave and the initial signal amplitude is zero.

The evolution of the phase in DFG and OPA has several important implications for laser design. First, the equations above show that the phase of the generated wave depends on the other two fields, in this case the pump and signal, only through the initial phase $\Phi_p(0) - \Phi_s(0)$. This means that if phase fluctuations of the input waves are identical, they will cancel out such that the phase of the generated wave is insensitive to these fluctuations. This concept is explored in the next section in the context of CEP stability in DFG. Secondly, the phase of the amplified field does not depend on the phase of the pump field, and therefore optical aberrations and chirp in the pump are not transferred to the seed during amplification. However, the phase does depend on the pump intensity, implying that fluctuations in the pump can affect the amplified phase. This deleterious effect is particularly problematic close to pump depletion. Finally, since the phase mismatch Δk is frequency dependent, so is the phase accumulated by the three waves. The implication for broadband operation is that energy exchange in general is not uniform across the spectrum of the three fields, leading to re-shaping of the input spectrum during amplification.

2.2.3 *The Manley-Rowe relations*

The Manley-Rowe relations were originally developed in the late 50s to predict energy transfer between waves in nonlinear electrical circuits [44]. More generally, these relations account for energy conservation in a nonlinear process, and as such also apply to three-wave mixing. The relations can in fact be derived directly from the coupled

wave equations. The Manley-Rowe relations for DFG are typically written as:

$$\frac{d}{dz}\left(\frac{I_i}{\omega_i}\right) = \frac{d}{dz}\left(\frac{I_s}{\omega_s}\right) = \frac{d}{dz}\left(\frac{I_p}{\omega_p}\right) . \tag{15}$$

Since the energy of a photon is $\hbar\omega$, the quantity I/ω is proportional to the photon flux N per unit area per unit time. Therefore the Manley-Rowe relations can also be written as:

$$\frac{dN_i}{dz} = \frac{dN_s}{dz} = \frac{dN_p}{dz} . \tag{16}$$

This relation states that the rate at which photons are created and destroyed throughout the nonlinear process is identical for the three waves. In other words, for each pump photon that is destroyed during amplification, a signal photon and an idler photon are necessarily created. The implication is that energy transfer between the waves depends on the frequency relations between the three fields. It can be easily deduced from the equation above that there is a set ratio of energy transfer from pump to idler and pump to signal, given by ω_i/ω_p and ω_s/ω_p respectively. This is an important result for OPCPA design, since it implies that the wavelength relation between the pump and seed impacts the efficiency of the amplification process. This design aspect will be discussed in more detail in Chapter 4.

2.3 PHASE-MATCHING

The basic principle behind phase-matching in DFG involves ensuring a phase relation between the interacting fields such that the generated wave can build up through constructive interference during the nonlinear interaction. The means to achieve this can be understood considering the simple case of collinear interaction, where the wave-vectors of the three interacting fields are parallel to each other. In this case the phase-matching condition $\Delta k = 0$ is met if:

$$\omega_p n_p = \omega_s n_s + \omega_i n_i . \tag{17}$$

This condition cannot be fulfilled in isotropic media. The most common way of achieving phase-matching is by making use of birefringence in anisotropic crystals. This technique, referred to as birefringence phase-matching, exploits the fact that in these materials the index of refraction depends not only on frequency but also on the the polarisation and propagation direction of the optical waves. In a uniaxial crystal, light polarised perpendicular to the plane containing the wave-vector $\vec{k}$ and the optical axis is known as the ordinary ray, experiencing a refractive index n_o, while light that is polarised in the plane containing $\vec{k}$ and the optical axis is know as the extraordinary ray, experiencing a refractive index n_e. Equation 17 implies that for the phase-matching condition to be fulfilled, the pump field must be polarised such that it experiences the lower of the two refractive indices. In a negative uniaxial crystal this corresponds to the extraordinary ray, while in a positive uniaxial crystal this corresponds to the ordinary ray. Depending on the dispersive properties of the medium, the signal and idler fields can either have parallel or orthogonal polarisation with respect to each other. These arrangement are referred to as Type I and Type II phase-matching respectively.

The refractive index of the extraordinary wave can be adjusted by changing the propagation direction with respect to the optical axis of the crystal. The refractive index can be calculated according to:

$$\frac{1}{n_e^2(\theta)} = \frac{\sin^2\theta}{n_e^2} + \frac{\cos^2\theta}{n_o^2}\,, \tag{18}$$

where θ is the angle between the wave-vector $\vec{k}$ and the optical axis and n_e is the refractive index of the extraordinary wave when $\theta = 90°$. A similar calculation can be used for biaxial crystals, where the phase-matching condition depends on the polar and azimuthal angle, θ and ψ.

An alternative approach to birefringence phase-matching is so-called quasi-phase-matching (QPM). This technique involves introducing a periodic spatial modulation in the nonlinear medium such that the sign of d_{eff} is changed after a certain propagation length.

A phase mismatch is allowed to build-up, but before the accumulated phase causes the energy flow to reverse back into the pump, the crystal axis are flipped and the direction of energy flow from pump to signal and idler is conserved. Since during the nonlinear process there is always a phase mismatch present, the conversion efficiency is lower than in the case of perfect phase-matching for an equal value of d_{eff}. However since this approach does not depend on the birefringent properties of the crystal, it allows a greater freedom to choose polarisation and propagation direction, which enables maximisation of the nonlinear coefficients. QPM also allows the use of highly nonlinear materials that are not suited for birefringence phase-matching due to low birefringence or an isotropic structure.

2.3.1 *Broadband phase-matching*

Broadband DFG and OPA require taking into account that the phase-matching condition needs to be satisfied for a range of wavelengths. Even if perfect phase-matching is achieved at the centre wavelength of the pump, signal and idler pulses, phase mismatch at other wavelengths can limit the effective interaction bandwidth. In order to account for a certain spectral width $\Delta\omega$, the phase mismatch Δk can be expanded as a Taylor series:

$$\Delta k = \Delta k_0 + \frac{\partial k_p}{\partial \omega_p}\Delta\omega_p - \frac{\partial k_s}{\partial \omega_s}\Delta\omega_s - \frac{\partial k_i}{\partial \omega_i}\Delta\omega_i + \dots , \tag{19}$$

where Δk_0 is the phase mismatch for the centre wavelengths of the three waves. Note that the derivatives of the wave-vector in Eq. 19 are the inverse of the group velocity v_g for the first derivative in the expansion to first order, the inverse of the group velocity dispersion (GVD) for the second derivative in the expansion to second-order and so on.

Further insight can be attained by assuming perfect phase-matching at the centre wavelengths, $\Delta k_0 = 0$, and re-writing the expansion to first order using energy conservation for the spectral width $\Delta\omega_i = \Delta\omega_p - \Delta\omega_s$:

$$\Delta k = (\frac{1}{v_{gp}} - \frac{1}{v_{gi}})\Delta\omega_p - (\frac{1}{v_{gi}} - \frac{1}{v_{gs}})\Delta\omega_s, \tag{20}$$

where v_{gp}, v_{gs} and v_{gp} are the group velocities of the pump, signal and idler waves. Equation 20 points to the difference in group velocity between the three waves as a source of phase mismatch for broadband interaction. Expansion of the Taylor series to higher orders leads to similar results, suggesting that fine-tuning of broadband phase-matching can be achieved by canceling out successively higher order terms. In the case of OPA, the pump is generally narrowband in comparison to the signal and idler, such that $\Delta\omega_p << \Delta\omega_s = \Delta\omega_i$. In this case, the group velocity of the pump is unimportant and the difference in group velocity between the signal and idler dominates the phase mismatch. This explains why degenerate Type I OPA, in which $\omega_s = \omega_i$, can exhibit a broad amplification bandwidth since the higher order terms automatically cancel out.

A different arrangement that can provide a large interaction bandwidth in DFG and OPA is known as non-collinear phase-matching [45, 46]. The technique involves introducing an angle between the input beams such that each wave propagates at a different direction with respect to the optical axis. Figure 1 shows a schematic of the geometric arrangement. According to this convention, θ is the angle between the optical axis and the pump, α and β are the non-collinear angles between the pump and the idler and signal respectively. The vectorial nature of the phase mismatch can be accounted for by projecting the wave-vectors of the signal and idler on the pump:

$$\Delta k_{\parallel} = k_p - k_s cos(\beta) - k_i cos(\alpha) \tag{21a}$$

$$\Delta k_{\perp} = k_i sin(\alpha) - k_s sin(\beta) \tag{21b}$$

Non-collinear phase-matching can increase the interaction bandwidth by minimising the group velocity mismatch. In the time domain, this can be advantageous for the efficiency of femtosecond OPA, since it increases the effective temporal overlap of the pulses. This is less relevant when dealing with stretched pulses, since the

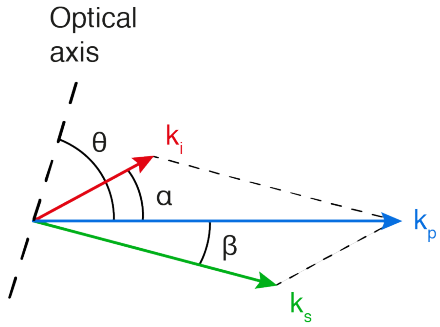

Figure 1: Schematic of phase-matching in non-collinear interaction showing the fixed geometric relation between the three wave-vectors.

effect of group velocity mismatch is typically negligible in comparison to the stretched pulse duration. For a narrowband pump, the phase-matching condition to first order can be found by projecting the group velocity of the idler on the signal:

$$v_{gs} = v_{gi} cos(\alpha + \beta). \tag{22}$$

The downside of this approach is that the generated wave becomes angularly dispersed. The reason for this is that the angle of the seeded wave with respect to the pump is fixed for the entire spectral width. However since the modulus of the wave-vector is proportional to the frequency, each frequency component of the generated wave is phase-matched at a different angle. This is generally not a concern in OPA, where the generated wave is usually discarded. However in a non-collinear DFG setup, as the one described in the following chapter, the angular dispersion of the generated wave needs to be taken into account.

2.4 CARRIER-TO-ENVELOPE PHASE IN DFG

A typical model used to describe the electric field of a pulse comprises a complex amplitude envelope modulated by a term oscillating at the centre (or carrier) frequency, of the pulse:

$$E(t) = A(t) exp(-i\omega_0 t + i\phi_o), \tag{23}$$

where $A(t)$ is the amplitude envelope of the pulse, ω_0 is the carrier frequency and ϕ_o represents the phase between the carrier wave and the envelope. The square modulus of $E(t,z)$ is proportional to the intensity of the pulse while the term $(-i\omega_0 t + i\phi_o)$ accounts for the oscillating electric field. Perturbative nonlinear processes such as DFG are driven by intensity and are insensitive to the electric field. However, some physical processes including strong-field phenomena related to electron recollision such as HHG, are driven by the electric field rather than by the intensity envelope. In this case, the phase of the electric field within the envelope of the pulse plays a central role [47, 48]. This is of course, particularly relevant for few-cycle duration pulses that contain only a few oscillations of the electric field within the envelope. ϕ_o is known as the CEP and together with the amplitude $A(t)$ it determines the waveform of the pulse (see Fig. 2). A CEP stable laser delivers a reproducible electric field from pulse-to-pulse.

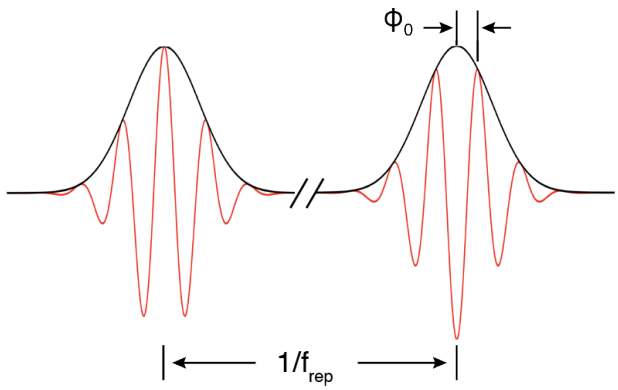

Figure 2: Schematic of a pulse in the time domain showing the oscillating electric field (red line) and intensity envelope (black line). The CEP ϕ_o is the phase between the peak of the intensity envelope and the oscillating carrier.

Mode-locked oscillators do not, in general, deliver a CEP stable output. The underlying reason for this is that dispersive elements inside the laser cavity lead to different phase and group velocities for the circulating pulse. Thus during a round-trip in the cavity the pulse accumulates a CEP, typically equivalent to tens or hundreds

of optical cycles. If the accumulated phase is not a multiple of 2π, successive pulses coupled from the oscillator exhibit a different CEP and therefore a different waveform. It can be useful to view the CEP of a train of pulses delivered by a mode-locked laser in the frequency domain [49, 50]. A Fourier transform of a train of identical pulses yields the spectrum of a single pulse, modulated at a frequency equal to the repetition rate of the laser, which is determined by $v_g/2L$, where v_g is the group velocity and L is the cavity length. This spectrum forms a comb-like structure around the centre frequency of the laser (see Fig. 3). The frequency of individual comb lines however is determined by their phase velocity rather than the group velocity, and so in general the frequency of the comb lines are not multiples of the repetition rate. The offset f_0, called the carrier-to-envelope offset frequency, and the change in CEP from pulse-to-pulse are related via:

$$2\pi f_0 = \Delta\phi_o f_{rep}, \tag{24}$$

where $\Delta\phi_o$ is the change in CEP from pulse-to-pulse and f_{rep} is the repetition rate of the laser. Accordingly, the frequency of the nth laser line is:

$$f_n = f_{rep} n + f_0. \tag{25}$$

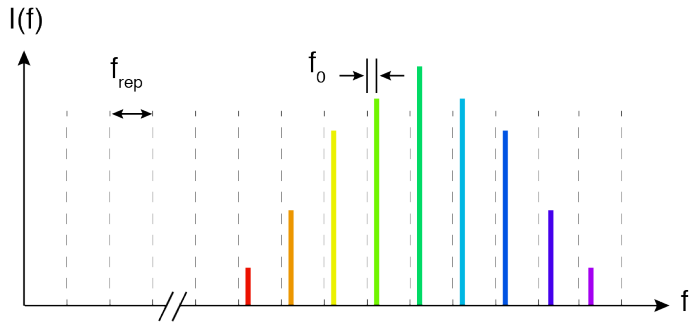

Figure 3: Schematic of the spectrum of a mode-locked pulse train in the frequency domain. The comb-like structure is offset from a integer multiple of the repetition rate f_{rep} by the carrier-to-envelope offset frequency f_0.

Numerous techniques have been developed to detect and correct CEP drift from mode-locked oscillators. Absolute CEP can only be measured using strong-field processes [51, 52], but changes in CEP can be measured using perturbative nonlinear optics and linear interference [53, 54]. Most of these stabilisation techniques use feedback loops that measure drift in the CEP and compensate for it by controlling dispersion or cavity length. As we have shown, OPA is a phase preserving process, and so if a train of CEP stable pulses are seeded into an OPA chain, a CEP stable output is expected.

DFG can be used to generate a CEP stable train of pulses by canceling out the CEP drift of the driving pulses [55]. Consider a set of comb lines constituting the pump and signal spectrum. The frequency of any two comb lines can be expressed as:

$$f_p = f_{rep} n + f_{0,p} \tag{26a}$$
$$f_s = f_{rep} m + f_{0,s}, \tag{26b}$$

where n and m are arbitrary integers and $f_{0,p}$ and $f_{0,s}$ are the carrier-to-envelope offset of the pump and signal respectively. If the pump and signal originate from the same oscillator, then $f_{0,p} = f_{0,s}$. Using energy conservation, any idler frequency generated via DFG can be computed by:

$$f_i = f_p - f_s \tag{27a}$$
$$= f_{rep}(n - m) \tag{27b}$$

This expression suggests that driving DFG with pulses with the same f_0 will lead to an intrinsically CEP stable output. In a real laser system, the pump and signal pulses will generally propagate through different dispersive media before the DFG stage. However, if the CEP accumulated during propagation is the same for successive pulses, as expected in the absence of turbulent air or vibrations, then the CEP shift from pulse-to-pulse is still the same for the pump and signal, and therefore the expression above still holds. Apart from turbulent air or vibrations, which can both be managed with careful design of the experimental setup, a possible source of problems in this approach are nonlinear effects coupling phase to intensity. In this case small fluctuation in intensity from pulse-to-pulse can affect the

phase of the driving pulses and therefore degrade the CEP stability of the DFG output.

3

GENERATION OF BROADBAND PULSES IN THE MID-IR

3.1 INTRODUCTION

For decades light sources operating in the mid-IR have been of interest mainly for their application in rotational-vibrational spectroscopy [56]. Owing to the rich absorption features present in this spectral region, this technique allows for unambiguous identification of numerous molecules, and is extensively used in various fields such as chemistry, biology and medicine [57, 58, 59]. Typically, experimental setups consist of a globar as a thermal light source and an infrared Fourier-transform spectrometer (FTIR) or scanning monochrometer for acquiring spectral data. A globar is the cheapest and most easily available source of broadband light. This type of light source generally exhibits low intensity noise, but the output is incoherent both spatially and temporally with a comparatively low spectral intensity.

Some applications, such as sensing of trace elements, hyperspectral imaging or micro-spectroscopy [60, 61, 62], require improved performance of the light source. The low brilliance of thermal sources can limit the signal-to-noise ratio and can hamper experiments requiring a high spatial resolution. In particular, chemical investigations of biological samples with microscopes, a field with tremendous potential for diagnostic medicine, require sub-cellular resolution. The use of more sophisticated sources such as synchrotrons, which can be configured to produce high brilliance mid-IR radiation up to 1000 times brighter than a thermal source [63], can overcome this limitation [64, 65]. However this improvement in performance comes at an extremely high economic cost and with the practical inconvenience of limited beam

time for experiments.

Broadband lasers emitting in the mid-IR are a rapidly evolving technology that may soon supersede both globar sources and synchrotrons for spectroscopic applications. Laser light can exceed by several orders of magnitude the brilliance of synchrotron sources, at a fraction of the cost and in a table-top setup [66, 67]. Aside from spectroscopy, sources of broadband mid-IR radiation have in recent years come into high demand as sub-systems required for building mid-IR OPCPA, where they are used as a seed source [29, 30, 31]. This application places strict demands on the seed laser, as many of the properties of the seed pulses largely determine the output parameters of the OPCPA. A suitable seed source needs to simultaneously provide a broad bandwidth compatible with a few-cycle pulse duration, exhibit good beam qualities, high pulse-to-pulse stability and preferably, CEP stability.

The topic of this chapter is the design and experimental realisation of a novel low energy (i.e. unamplified), broadband, coherent, mid-IR light source. The main application envisioned for this laser is seeding a high energy, ultrafast mid-IR OPCPA. The laser architecture described in this chapter is based on the pioneering development in the late 2000s of the first ultrashort, CEP-stable, mid-IR source by the AUO group at ICFO [29, 33, 34]. The work presented here extends these results from the short-wave IR deeper into previously unexplored wavelengths of the mid-IR range. The main results of this chapter were published in [68] and [69]. This chapter is structured as follows: first, the most common techniques for generating ultrashort mid-IR pulses using laser media and parametric processes are briefly reviewed. Next, the nonlinear media available for mid-IR applications are discussed. The most promising crystals are identified and their main characteristics are reviewed. The experimental setup is discussed next. This includes the fibre laser front-end and the DFG stage. Finally, the experimental results of the DFG stage and the characterisation of the mid-IR are presented.

3.2 PARAMETRIC DOWNCONVERSION

A major challenge to the development of ultrafast mid-IR sources is the scarcity of suitable laser media emitting directly in this spectral range. Currently, the most promising materials for direct emission

are transition metal doped laser chalcogenides such as ZnTe or ZnSe, featuring Cr^{2+} or Fe^{2+} as dopant [70, 71]. Cr^{2+} doped chalcogenide lasers have shown particularly promising results. These systems operate around a wavelength of 2.5 μm with an emission band spanning the spectral region from 2 to 3 μm. The absorption band is such that the medium can be conveniently pumped by Er:fibre and Tm:fibre lasers. Early experiments exploring mode-locking operation demonstrated the suitability of Cr^{2+} doped lasers to directly generate pulses shorter than 100 fs [72, 73, 74]. More recent results with improved intracavity dispersion management have shown the possibility of generating even shorter pulses with Watt-level average power and nJ level energies [75, 76]. The emission of Fe^{2+} doped crystals lie deeper in the mid-IR. These materials exhibit a broad emission bandwidth in the 3 to 5 μm range and have been successfully used to develop tuneable lasers [71, 77, 78]. In principle the emission bandwidth of Fe^{2+} doped crystals is broad enough to support femtosecond pulses. Mode-locking however, has not yet been demonstrated and therefore it remains to be shown if Fe^{2+} doped crystals are well suited for ultrashort pulse generation.

The standard route for generating ultrashort pulses in the mid-IR with lasers is not direct emission but rather through nonlinear frequency conversion of near-IR laser light [79]. Optical parametric oscillation (OPO) and DFG are popular experimental schemes. OPA can also be considered a technique for generating mid-IR pulses, but the term usually refers to amplification rather than generation. Physically these processes are examples of three-wave mixing, which was described theoretically in Chapter 2. Conceptually, parametric downconversion consists of using a nonlinear medium to transfer energy from a short wavelength to a longer wavelength via three-wave mixing. In practice, this is a convenient approach for reaching the mid-IR given the abundance of ultrafast laser sources at comparatively shorter wavelengths. One of the main interest in parametric sources is the flexibility they provide in output wavelength. In contrast to stimulated emission, the operating wavelength and bandwidth of these sources is not determined by laser transitions but rather by the dispersive properties of the nonlinear medium.

OPOs are parametric sources similar to laser oscillators. In an OPO, amplification occurs in a nonlinear crystal [80] placed inside an optical cavity which is usually resonant at either the signal or the idler wavelength. OPOs are a common light source of mid-IR light, specially for spectroscopic application due to their wavelength tuneability. Given that the amplified pulse duration is forced by the nonlinear process to be comparable to the pump duration, ultrashort operation is usually achieved by resonant pumping of the nonlinear crystal with mode-locked femtosecond lasers [81]. Even though intra-cavity dispersion is a serious challenge for few-cycle regime operation in the mid-IR, recent work has shown the feasibility of this approach [82]. The principle drawback of OPOs, particularly as a seeder for an amplifier line, is the complexity added by the cavity and additional effort required to maintain the output stability.

DFG setups are single-pass arrangements that generally use two broadband pulses to generate a third pulse at a longer wavelength. The conversion efficiency to the idler wavelength is low in comparison to OPO, where the efficiency can be high enough as to cause appreciable pump depletion. On the other hand DFG offers a much simpler and flexible setup. The generated bandwidth is only limited by the phase-matching properties and transparency of the crystal and the bandwidth of the driving pulses. DFG setups have been extensively used for mid-IR femtosecond pulse generation using various driving lasers such as Ti:Sapphire [83], Er:fibre [84] and Yb:fibre [85] based systems. As discussed in Chapter 2, mid-IR sources derived from DFG from a common mode-locked oscillator are of particular interest since such architecture directly provides CEP stable pulses and therefore mid-IR frequency commbs. In comparison to OPO, the simplicity of a DFG setup makes this technique better suited as a seed source for complex laser architecture such as OPCPA.

3.3 NONLINEAR MATERIALS FOR DOWN-CONVERSION TO THE MID-IR

The experimental feasibility of a given nonlinear process is largely determined by the existence of a suitable nonlinear medium. In the case

of parametric downconversion, the process requires three fundamental properties in order to be realised experimentally: transparency of the nonlinear medium at the pump, signal and idler wavelengths, appropriate phase-matching abilities and a large enough nonlinearity. Other secondary characteristics such a high damage threshold, good mechanical properties, ease of growth that guarantees samples of good quality and commercial availability also need to be taken into consideration. In the near-IR, these requirements are typically met by oxide crystals, such as BBO, $LiNbO_3$, LBO, etc. Oxides are the most widely used nonlinear crystals, for which there exists a well-established growth technology and high quality and off-the-shelf availability are common.

However the usefulness of oxide crystal in the mid-IR is limited by their transparency. Most of these crystal are hardly transparent above 2 μm due to multiphonon absorption. Even exceptional cases such as $LiNbO_3$ or KTA have limited use above 4 μm. Therefore, mid-IR applications require the employment of non-oxide crystals. Unfortunately, the technology for growing these materials is less developed than for oxides, leading to an increase in growth defects. Generally residual absorption in non-oxides is higher and the damage threshold is lower than in oxide nonlinear crystals. In addition, standard post-growth processes such as cutting and polishing can be challenging or in some cases impossible. Nevertheless over the last decades an intensive search for new nonlinear materials suitable for mid-IR applications has lead to an improvement of existing crystals as well as to the synthesis of promising new materials [86, 87].

Table 1 shows a list of nonlinear crystals exhibiting transparency in the mid-IR as well as relevant properties for nonlinear applications: type of birefringence, transmission range in the near-IR to mid-IR, the effective nonlinear coefficient d_{eff} and the thermal conductivity [88, 86]. The value of d_{eff} depends not only on the nonlinear material but also on the parameters of the interaction: wavelength and polarisation of the interacting fields and propagation direction in the crystal. The values of d_{eff} shown in this table correspond to the configuration used for the DFG stage described later in this chapter: phase-matching the following Type 1 DFG: 1.55 μm (e-wave) - 2 μm

(o-wave) = 7 µm (o-wave). The only exception is ZGP, which is not transparent at 1.55 µm. In this case the pump was set to 2 µm and the idler fixed at 7 µm. The calculation of d_{eff} was performed using the SNLO software and database [89].

Crystal	**Type**	**Tp [µm]**	d_{eff} **[pm/V]**	**Tc [W/mK]**
$AgGaS_2$ (AGS)	Neg. uniaxial	0.5-13	8.7	1.4
$AgGaSe_2$ (AGSe)	Neg. uniaxial	0.8-18	31.1	1
$ZnGeP_2$ (ZGP)	Pos. Uniaxial	2-11	79.5	35
GaSe (GS)	Neg. uniaxial	0.65-18	56.7	16
$CdSiP_2$ (CSP)	Neg. uniaxial	0.65-9	43	13.5
$LiGaS_2$ (LGS)	Biaxial	0.3-11.5	4.5	unkn.
$LiGaSe_2$ (LGSe)	Biaxial	0.4-13	7.7	unkn.
$LiInS_2$ (LIS)	Biaxial	0.4-11.5	4.8	6
$LiInSe_2$ (LISe)	Biaxial	0.5-12	5.8	4.5
GaAs	Isotropic (QPM)	0.8-17	70	55
GaP	Isotropic (QPM)	0.6 -13	70	110

Table 1: List of available mid-IR nonlinear crystals and relevant properties for their application in parametric downconversion. Tp, transparency; Tc, thermal conductivity.

The list includes common crystals as well more exotic and recent developments. Among the most popular are silver thiogallate ($AgGaS_2$ or AGS) and silver gallium selenide ($AgGaSe_2$ or AGSe) [90, 91, 92]. These are negative uniaxial chalcopyrites that have been widely used for downconversion to the mid-IR for over 30 years [93, 94]. High quality samples of both crystals can be acquired commercially. AGS and AGSe exhibit similar properties: low linear absorption, large transmission range in the mid-IR and low thermal conductivity and damage threshold. The comparatively large bandgap of AGS allows for high intensity pumping around 1 µm without two-photon absorption. AGSe exhibits a slightly higher nonlinearity and transmission deeper into the mid-IR. Both AGSe and AGS have anisotropic thermal expansion with different sign, making them un-

suited for high average power applications.

Gallium selenide (GaSe) is a well established material for long wavelength nonlinear applications [95, 96]. It is extensively used in the generation and detection of THz radiation with ultrashort pulses [97]. The crystal has excellent linear and nonlinear optical properties but poor mechanical characteristics. GaSe has a large nonlinearity and birefringence, with potentially broad phase-matching abilities. However it has a crystal structure such that it can only be cut perpendicular to the optical axis, making certain angular phase-matching configurations unattainable. It has a low damage threshold, suffers from two-photon absorption and is extremely soft and brittle (0 on the Mohs hardness scale) making it difficult to handle and to polish, leading also to serious technical challenges in regards to optical coatings.

Zinc germanium phosphide ($ZnGeP_2$ or ZGP) is a positive uniaxial crystal investigated since the late 60s exhibiting an unusually high nonlinearity (d_{eff} as high as 75 pm/V) [98, 99]. ZGP also presents a high thermal conductivity and relatively high damage threshold. A serious drawback for this crystal is residual and multiphonon absorption, which limit the transparency range in both the near-IR and mid-IR. Even though the band gap is 2 eV (~600 nm), residual absorption requires the crystal to be pumped above 2 μm, thus making the crystal unsuitable for 1 and 1.5 μm pumping. Nevertheless the attractive nonlinear properties of ZGP has led the crystal to be widely used for downconversion to the mid-IR region [100, 101]. Rapid advances in the quality and size of samples and improved polishing techniques [102] make it one of the most promising candidates for high intensity applications in the mid-IR. In Chapter 5 we show the performance of ZGP as an OPA crystal for amplifying 7 μm pulses using a 2 μm pump.

Cadmium silicon phosphide ($CdSiP_2$ or CSP) is a uniaxial chalcopyrite similar to ZGP that has drawn attention in recent years. CSP was first investigated in the 70s [103], but poor sample quality hampered practical applications until recent improvements in growth technology has enabled the production of large-aperture

high-quality samples [104, 105]. CSP has a nonlinearity comparable to ZGP ($d_{eff} = 85$) pm/V and a similar bandgap (2.2 eV). Unlike ZGP however, CSP is transparent at 1 μm. Though smaller than ZGP, the thermal conductivity is an order of magnitude higher than AGS and AGSe, making CSP a promising alternative for high average power applications. CSP is not yet commercially available, however it has been successfully used in OPO and OPG setups to generate broadband light around 6 μm with 1 μm pumping [106, 107]. We will show in this chapter the use of CSP for generating ultra-broadband 7 μm wavelength pulses via DFG.

The four ternary wide band-gap biaxial crystal $LiGaS_2$ (LGS), $LiGaSe_2$ (LGSe), $LiInS_2$ (LIS) and $LiInSe_2$ (LISe) are new additions to the list of commercially available mid-IR nonlinear materials [108, 109, 110]. These crystals were reported as early as the 50s, but growth related problems prevented proper characterisation until the last decade. Compared to the other crystals considered in this section, LGS, LGSe, LIS and LISe present the lowest nonlinearity, close to an order of magnitude less than CSP for example. The main interest is the unusually large band gap and transparency range. These are the only non-oxide crystals that allow high intensity pumping at 800 nm without two-photon absorption. To give an example, LGS has a bandgap as large as 3.7 eV and is transparent from 320 nm up to 11 μm. In addition, their thermo-mechanical properties and damage threshold are also superior to other mid-IR crystals which can be pumped at 1 μm, such as AGS and GaSe. In a recent work outside of the scope of this thesis [111], we used LGS to generate an ultra-broad bandwidth spanning the wavelength range from 6.8 μm to 16.4 μm via intra-pulse DFG. Using 20 fs duration pulses with a centre wavelength of 1030 nm from a 100 MHz Yb:YAG oscillator, we determined the damage threshold of LGS to be as high as 10^{12} W/cm^2.

Finally, notable advances in non-oxide QPM crystals require some attention [112]. For the last two decades, MgO-doped periodically poled $LiNbO_3$ (MgO:PPLN) has been the most common QPM crystal for long wavelength nonlinear devices [113, 84, 114, 33]. Notably, MgO:PPLN was the crystal employed by the AUO group at ICFO in

the development of the first mid-IR OPCPA as nonlinear medium in both the DFG and OPA stages [29]. Using temperature-controlled crystals, a spectrum spanning the range from 2.9 μm to 3.8 μm was generated via DFG and amplified to the μJ range using a Nd:YVO_4 mode-locked pump laser. Multi-phonon absorption above 4 μm however, has limited the use of MgO:PPLN in the mid-IR [115]. Semiconductor QPM materials, such as orientation patterned GaAs (OP-GaAS) and GaP (OP-GaP), exhibit transparency deep into the mid-IR as well as high nonlinearities and excellent thermal conductivity. OP-GaAs was the first QPM semiconductor to be developed [116], and has been shown to be an attractive material for parametric devices [117, 118] due to its high nonlinearity and transparency reaching 18 μm. Similarly to ZGP, the main drawback of Op-GaAs is that it requires pumping above 1.7 μm due to strong two-photon absorption. OP-GaP is the most recent QPM semiconductor [119] offering several advantages over OP-GaAs, particularly compatibility with 1 μm pumping. OP-GaP exhibits a similar nonlinearity to OP-GaAS with an extremely high thermal conductivity (T_c=110 W/mK), an order of magnitude higher than the birefringent crystals discussed in this section. Recent results have highlighted the potential of OP-GaP as the next generation of mid-IR QPM materials [120, 121].

3.4 EXPERIMENTAL SETUP AND RESULTS

3.4.1 *Front-end: two wavelength femtosecond fibre laser*

Fibre lasers are attractive contenders as front-end sources for OPCPA, offering a number of advantages over bulk solid-state lasers. The stability and robustness of fibre lasers, as well as alignment-free and hands-off operation are particularly beneficial for seeding complex laser architectures. OPCPAs typically have long propagation distances with multiple stages for beam conditioning, amplification and dispersion management. Therefore small changes in the seed, such as pointing or pulse duration, can have large effects on the behaviour of the laser, making daily maintenance time-consuming and long experiments difficult. Among the different available fibre-based systems, Er-doped fibre lasers operating around 1.55 μm have a particularly

well developed technology, the main driver of which has been applications in optical communications. A large variety of diode-pumped Er-doped fibre oscillators and amplifiers are commercially available. Using all-fibre schemes that include dispersion management stages, these systems are capable of delivering femtosecond pulses at nanojoule energy levels from compact and simple setups with excellent beam profile and long-term stability.

A simple calculation shows that in order to access the spectral range around 7 μm using an Er-doped femtosecond system centred at 1.55 μm, another femtosecond source centred at either 1.2 μm or 2 μm is required. While there are no commercially available broadband lasers operating around 1.2 μm, the recent development of diode pumped Tm/Ho co-doped fibre amplifiers allow amplification of broadband pulses around 2 μm. Used in combination with an Er-doped femtosecond fibre laser, a Tm/Ho co-doped laser would provide a robust all-fibre system for driving mid-IR DFG. Apart from the convenience of fibre lasers, this scheme offers another notable advantage. The Tm/Ho amplifier can be conveniently seeded by the 2 μm region of a supercontinuum (SC) driven by an Er:fibre system, thus providing a convenient route for generating synchronised and mutually coherent ultrashort pulses at 1.55 μm and 2 μm from an all-fibre source. As discussed in Chapter 2, this approach also guarantees passive CEP stabilisation of the DFG output.

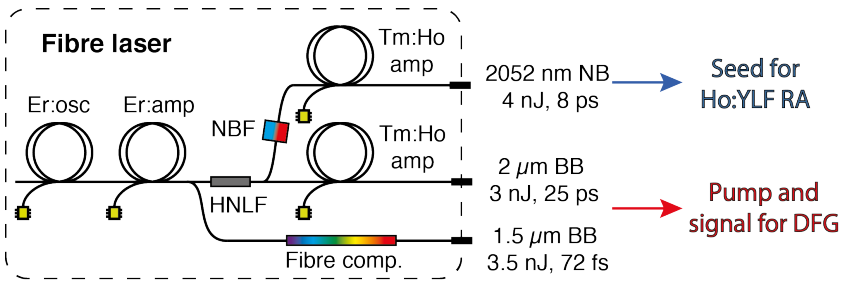

Figure 4: Schematic of the fibre laser showing the two femtosecond outputs at 1.55 μm and 2 μm used to drive the DFG stage and a third, narrowband output at 2 μm for seeding a picosecond amplifier; HNLF, highly nonlinear fibre; NB, narrowband; BB, broadband.

A fibre laser based on these considerations was designed and built by Menlo Systems GmbH in collaboration with the AUO group at ICFO. A detailed description of the laser can be found in [68]. Figure 4 shows a schematic representation of the fibre laser. The system was a two colour laser based on a 100 MHz mode-locked Er:fibre oscillator. The oscillator delivered 100 fs duration pulses at a centre wavelength of 1.55 μm which were subsequently amplified to 4 nJ in an Er:fibre amplifier. The output of the Er amplifier was then split into two arms. The first was sent to a 1.55 μm fibre compressor and subsequently used as the pump pulse for the DFG stage. The second was sent to a highly nonlinear fibre that broadened the spectrum to over an octave via SC generation. The broadened spectrum spanned from 1 μm to 2.4 μm. The output of the SC stage was split and used to seed two separate diode pumped Tm/Ho:fibre amplifiers. The first seeded a broadband Tm/Ho:fibre amplifier the output of which was subsequently used as the signal pulse for the DFG. The second output was used to seed a narrowband (NB) amplifier. Prior to amplification, the seed was narrowed spectrally to 3 nm bandwidth at FWHM centred at 2052 nm using a free space band filter consisting of a grating and a slit. This output was used to seed the 2 μm pump laser described in Chapter 4.

The spectra of the pump and signal beams, centred at 1.55 μm and 2.03 μm respectively, were measured using an FTIR spectrometer and a liquid nitrogen cooled HgCdTe (MCT) detector (Fig. 5). The typical average power measured at the output of the fibre system was 350 mW and 300 mW for pump and signal respectively, yielding pulse energies of 3.5 nJ and 3 nJ at the repetition rate of 100 MHz. A BBO based SHG frequency-resolved optical gating (FROG) was used for temporal characterisation. The FROG measurement revealed a pulse duration of 25 ps for the uncompressed signal output. The pulses carried a large second-order spectral phase, but due to the time-reversal ambiguity in the SH-FROG measurement, the sign of the chirp was unknown. Nevertheless, the chirp was expected to be negative due the dispersion characteristics of the fibre around the 2 μm region. An all-reflective positive dispersion free-space compressor was used to compress the chirped pulses. The compressor featured a 30-cm-focal-length spherical gold mirror, gold reflective

optics and an off-the-shelf aluminium coated diffraction grating with 360 lines/mm. The compressor throughput was measured to be 32 %, yielding compressed pulses at 2.03 µm with an energy of 1 nJ. Figure 5 shows the FROG retrievals of the compressed pump and signal pulses, revealing a pulse duration of 72 fs and 130 fs respectively. The characterisation of the NB output will be shown in the next chapter.

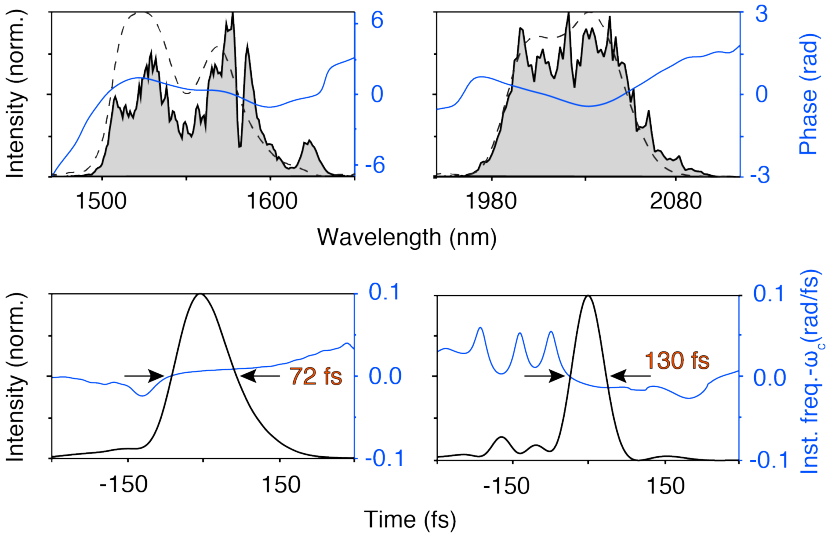

Figure 5: Characterisation of the femtosecond outputs of the two-color Tm/Ho:fibre fibre laser using FROG: (top) measured and retrieved (dotted line) spectrum and spectral phase (blue line), (bottom) retrieved temporal intensity and phase [69].

3.4.2 *Choice of nonlinear crystal: $CdSiP_2$*

Choosing a nonlinear crystal for mid-IR applications is far from straightforward. Widely used oxides such as BBO or KTP have limited or no transparency in the mid-IR, making it necessary to resort to less common non-oxide nonlinear crystals. For the application under consideration in this work, the crystal needs to fulfill two basic properties: high transparency at the pump, signal and idler wavelengths and phase-matching properties to allow the generation of few-cycle pulses via DFG. Apart from these two basic properties,

the crystal should also have a high nonlinearity in order for the downconversion process to be efficient while allowing the use of a short crystal. It is also highly desirable for the crystal to have good mechanical properties and a high damage threshold, even though the peak intensity and average power of the pump and signal are low. Finally, hydroscopic crystals should be avoided since they require a permanent dry air environment to avoid degradation.

In terms of transparency, the nonlinear medium should be able to accommodate the pump (1.55 μm), signal (2.03 μm) and idler (5-9 μm) wavelengths. This rules out ZGP, which must be pumped above 2 μm. Some of the more widely used mid-IR crystals such as GaSe, $AgGaS_2$ and $AgGaSe_2$ as well as more recently development lithium based crystals $LiGaS_2$, $LiGaSe_2$, $LiInS_2$ and $LiInSe_2$ satisfy this transparency condition. GaSe is a promising candidate, due to its high nonlinearity and birefringence. However, as we have discussed, GaSe is a soft and brittle crystal with a low damage threshold that cannot be easily cut, polished or coated. $AgGaS_2$ and $AgGaSe_2$ have a well developed growth technology and can be easily obtained commercially polished and AR coated, but they have unfavourable thermo-mechanical properties and a comparatively low d_{eff}. On the other hand, $LiGaS_2$, $LiGaSe_2$, $LiInS_2$ and $LiInSe_2$ all have excellent thermo-mechanical properties and good quality samples have recently become available, but they exhibit the lowest values of d_{eff} among the crystals considered here.

The negative uniaxial crystal CSP [105] is a promising alternative to these crystals due to its remarkably high effective nonlinear coefficient (as high as d_{eff} = 85 pm/V) as well as good thermal conductivity and phase-matching properties. In terms of d_{eff}, CSP outperforms all the crystals mentioned above and the transparency range that spans from 0.5 μm to 9 μm can comfortably accommodate our pump, signal and idler spectra for both linear and two-photon absorption. CSP has already shown great potential for downconversion to the mid-IR in non-critically phase matched schemes [106, 107], yielding high efficiency in limited bandwidth (100-200 nm). However a broader bandwidth could be achieved using a critically phase-matched con-

figuration. Based on these considerations, CSP was chosen as the nonlinear crystal for the DFG stage.

3.4.3 *Interpulse DFG in $CdSiP_2$*

In order to determine the optimum configuration of the input beams and the thickness of the crystal, a full 3D nonlinear wave propagation code [122] was used to simulate the DFG process in CSP. For comparison, the simulations were also performed using the common crystal AGS as the nonlinear medium. This code accounts for all the relevant phenomena involved in the DFG process, such as temporal and spatial walk-off, non-collinear geometry, linear and two-photon absorption, etc. The code has a proven ability for modelling complex laser systems [123]. The input pulses were modelled spectrally and temporally based on the FROG measurements shown in Fig. 5. The linear and nonlinear properties of the CSP crystal were taken from [124] and [125] respectively.

Phase-matching the DFG process 1.55 μm - 2.03 μm = 6.5 μm in CSP in collinear geometry is in principle possible in both phase-matching configurations, Type I (e-o=o) and Type II (e-o=e) for θ=52° and θ=65.5° respectively. Both configurations have a relatively broad phase-matching bandwidth, but neither of them allows phase-matching the full bandwidth provided by the fibre laser. The simulations suggested that in order to take full advantage of the bandwidth provided by the pump and signal pulses, which was required in order to generate a spectrum supporting few-cycle pulse, it would be necessary to resort to non-collinear geometry. This approach has the disadvantage that the idler beam will be generated with some angular dispersion. However, this problem can be corrected using a grating and telescope arrangement [126, 127].

According to the simulations, the broadest phase-matching was obtained for a propagation direction of the signal at θ = 66.5° with respect to the optical axis and an internal non-collinear angle between the signal and the pump of α = 1.85° for Type I (e-o=o) interaction. This corresponds to an external angle of α_{ext}=5.6°, and momentum

conservation predicts that the generated mid-IR beam will be emitted from the nonlinear crystal at an angle of 18° from the pump beam. For Type I interaction in a negative uniaxial crystal, the pump is the e-beam while the signal and idler are o-beams. For practical and safety reasons, it is desirable for the non-collinear angle between signal and pump to be contained in the horizontal plane, which forces the pump to be p-polarized and the signal and idler to be s-polarized. Figure 6 shows the geometric arrangement of the beams for the non-collinear DFG stage.

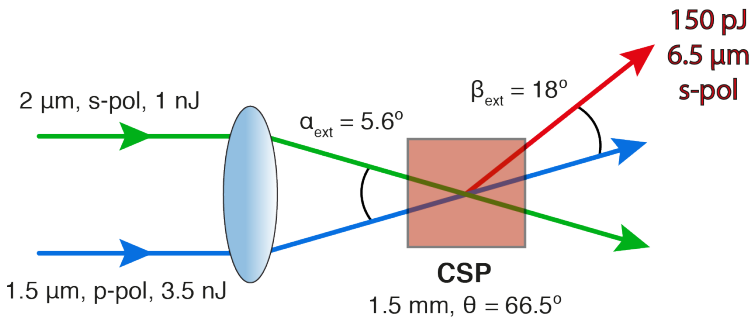

Figure 6: Schematic of the setup used for the non-collinear DFG showing the geometric arrangement and polarisation of the pump, signal and idler beams.

The optimum thickness of the nonlinear crystal is more difficult to determine. In general, due to the accumulation of phase mismatch, a thicker crystal will lead to higher efficiency at the expense of bandwidth, and a balance needs to be found between the two. In addition, in tight focusing schemes spatial overlap can limit the effective interaction length in the nonlinear medium. In our simulations, the optimum crystal thickness was determined by studying the evolution of the idler bandwidth and energy as a function of propagation distance. The simulations showed that the idler pulse energy increased linearly while the bandwidth slightly decreased over the first 2 mm of propagation, after which the combined effect of temporal and spatial walk-off as well as the non-collinear geometry caused both bandwidth and energy to remain constant as the temporal and transverse spatial overlap of the pump and seed reduced (see Fig. 7). In

addition, the non-collinear geometry caused the idler beam profile to be increasingly oval with propagation distance. Taking these simulation results into account, the crystal thickness was set to 1.5 mm as a tradeoff between optimum energy, bandwidth and beam profile. The simulations predicted an idler pulse energy of approximately 75 pJ and over 1500 nm of bandwidth at FWHM at a centre wavelength of 6.7 μm. In the case of AGS, a larger non-collinear angle required for phase-matching and group velocity mismatch caused the effective interaction length to be limited to around 1 mm. Taking these results into account, a high quality CSP crystal cut at $\theta = 66.5°$ was obtained via a collaboration with BAE Systems and subsequently AR coated for the pump, signal and idler wavelengths (Twinstar Optics). The crystal was 1.5 mm in length with an aperture of 5 x 6 mm^2.

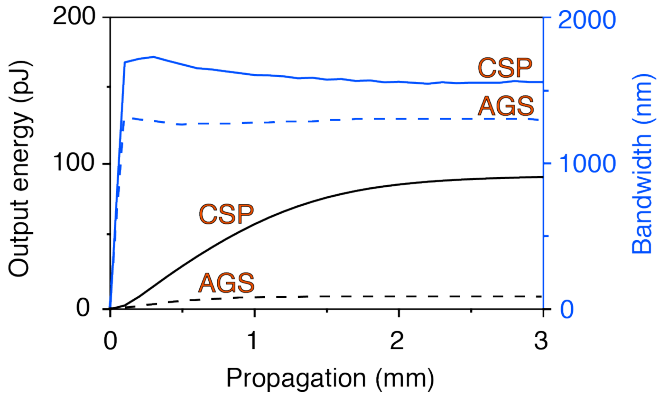

Figure 7: Simulation results for DFG in CSP and AGS: evolution of the idler pulse energy (black line) and bandwidth at FWHM (blue line) as a function of propagation distance in the CSP (solid line) and AGS (dashed line) crystals [69].

Due to the combined requirement of having a small angle between the pump and signal beams together with a tight focus, a single focusing lens was used for the DFG, such that the parallel input beams were spatially overlapped at the focus of the lens. Tuning of the non-collinear angle was achieved by displacing the pump beam from the centre of the focusing lens while keeping the input beams parallel to insure spatial overlap at the common focus. In order to

obtain a high intensity at the crystal and matching the focused beam sizes, the collimated radii of the input beams were conditioned using a telescope setup. Both input beams were focused to a FWHM diameter of 44 µm with a 5 cm CaF_2 lens into the 1.5 mm AR coated CSP crystal. Due to the absorption features in water vapor in this wavelength range, the entire setup was kept in a dry air environment (see Fig. 8).

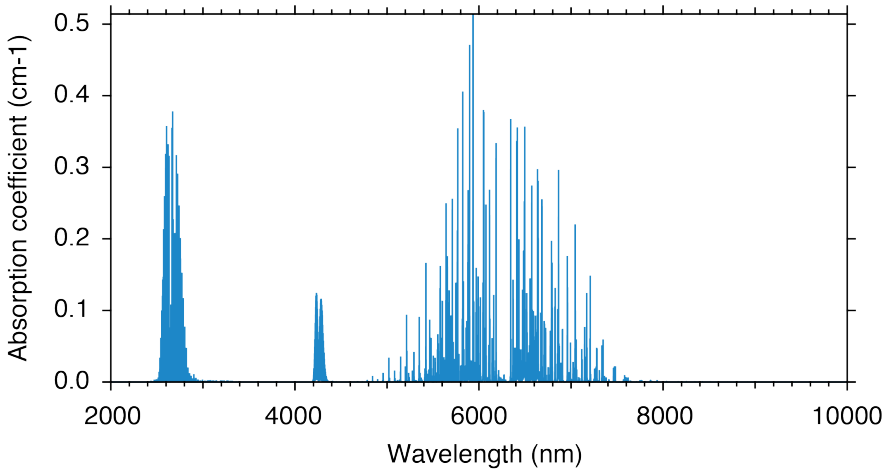

Figure 8: Simulated absorption profile of ambient water vapor in the mid-IR. Data taken from the HITRAN database [128].

The mid-IR beam generated in the DFG was collimated using a 4 cm focal length CaF_2 lens. No dichroic optics were required to separate the pump and signal beams from the idler, the angle between the beams was large enough to allow placing a beam dump before the collimating lens. An FTIR spectrometer equipped with a liquid nitrogen cooled MCT detector was used to acquire the spectral data. The generated mid-IR radiation was centred at 6.5 µm and exhibited a spectrum covering the range from 5.5 to 8 µm, supporting 50 fs transform-limited duration pulses, corresponding to less than 3 optical cycles at 6.5 µm (see Fig. 9). Note that some absorption in the collimating CaF_2 lens and optical components in the FTIR spectrometer is expected on the long wavelength side of the spectrum.

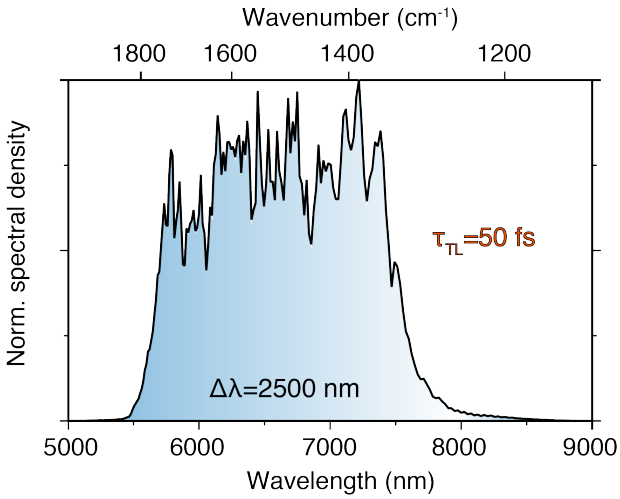

Figure 9: Spectrum of DFG output measured with an FTIR spectrometer. The generated bandwidth spanned 2500 nm from bottom to bottom with a transform limited pulse duration of 50 fs [69].

A pyroelectric detector (Ophir Nova) was used to measure average power. The mid-IR beam carried approximately 15 mW of average power, corresponding to a pulse energy of 150 pJ at the repetition rate of 100 MHz. The average power in the mid-IR beam was high enough to be visible on detector cards based on thermo-chromic liquid crystals. A micro-bolometer camera was used to record the beam profile at the output of the DFG. Figure 10 shows a typical measurement in the near and far field. Both the focused and collimated beams exhibit a slightly oval shape, caused by the non-collinear geometry of the DFG. The pulse-to-pulse stability of the DFG could not be measured due to the lack of fast photodiodes at this wavelength. The power stability, measured using a pyroelectric detector, was measured to be better than 0.9% of the rms over a period of 30 minutes (see Fig. 10).

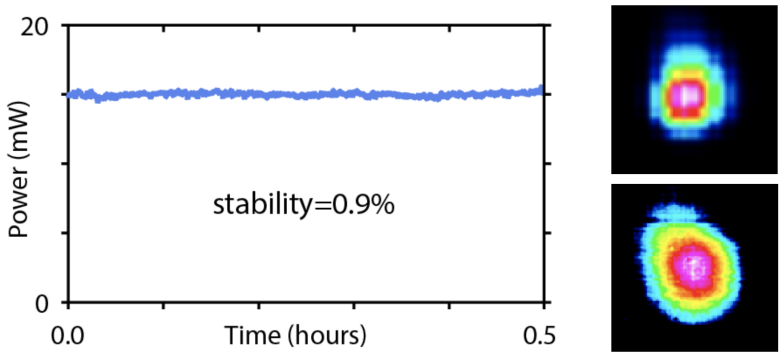

Figure 10: Power stability and beam profile of DFG output: (left) power stability measured over 30 minutes with a pyroelectric detector, (right, top) beam focused with a 50 cm uncoated BaF_2 and (right, bottom) collimated beam (right). The line that can be seen on the top half of the collimated beam is an artifact from the camera.

4

HIGH ENERGY PUMP SOURCE FOR MID-IR OPCPA

Since the first demonstration over 25 years ago [129], OPCPA has matured to the point of competing and even outperforming Ti:Sapphire lasers in the generation of high intensity pulses. The advantages of OPCPA are well known - a broad gain bandwidth, flexibility in operating wavelength and reduced thermal issues are among the most important. There is however a frequently overlooked caveat; OPCPA places extremely strict requirements on the pump laser. The underlying reason for this is the quasi-instantaneous nature of energy transfer in OPA. Due to the fact that there is no energy storage in the amplification medium, the pump and seed pulses need to perfectly overlap spatio-temporally in order for efficient amplification to occur. Precise temporal synchronisation between the pulses is crucial. In addition, the time-dependence of the instantaneous frequency of the stretched seed pulses means that timing jitter will not only affect the pulse-to-pulse stability, but also spectrum and phase. The spatial profile of the pump is also critical, as poor beam quality directly affects efficiency as well the profile of the amplified beam. Finally, even though in principle the stretched seed pulse duration can be chosen, practical considerations such as optical damage and dispersion management restrict the range of pulse duration of the pump.

The pump lasers employed in near-IR OPCPAs have become highly developed and varied in the last decades. Typically, these laser systems are based on Nd- and Yb- doped media operating around a wavelength of 1 µm. Numerous schemes have been demonstrated to produce pulses with energies ranging from microjoule to Joule level and pulse durations from a few picoseconds to hundreds of picoseconds [130]. Fibre-based pump architecture has shown to be suited for high average power systems reaching repetition

rates as high as the MHz range [131, 132]. Low repetition rate, high energy pump lasers producing over a Joule of pulse energy have been demonstrated using flashlamp pumped large aperture Nd:YAG based sources [133, 134]. The middle ground between these two extremes is covered with numerous diode pumped, solid state sources. Systems based on Nd:YVO_4 producing pulse energies of over 100 microjoule at 100 kHz are commercially available and have been successfully used to pump OPCPA [29]. Several other recent trends in OPCPA pumps, such as thin-disk technology [135] or cryogenically cooled Yb amplifiers [136] show great promise for further progress. In short, currently there exists a variety of pump lasers for near-IR OPCPA that meet a large range of experimental requirements.

However, for reasons that will be covered in this chapter, lasers operating around 1 µm are not ideally suited for pumping long wavelength OPAs. In recent years, in parallel to the emergence of mid-IR OPCPA, significant efforts have been invested toward developing novel laser systems specifically designed for pumping long wavelength OPAs. Spectroscopic investigations in the decades after the invention of the laser identified several gain media suitable for emission at long wavelengths, particularly around 2 µm [137, 138, 139, 140]. Ho-doped media have established themselves as the most promising material for high energy operation after overcoming a lack of suitable pump sources. This issue was solved with development and commercial availability of high-power CW Tm-doped fibre lasers in the early 2000s which enabled efficient pumping of Ho-doped media [141, 142]. A landmark experiment in 2007 showed the potential of Ho:YLF as laser medium for pumping long wavelength parametric oscillators [143]. In the last decade, largely driven by the development of mid-IR OPCPA, numerous Ho-based systems have been demonstrated with outputs ranging from nanosecond [144] to sub-picosecond [145] pulse durations, energies up to hundreds of mJ [146] and repetition rates up to the multi-KHz range [147, 148].

The topic of this chapter is the design and implementation of a 2 µm wavelength, high energy pump source for mid-IR OPCPA. The laser was designed with the aim of being integrated together with the 7 µm seed source described in Chapter 3 to pump a 7 µm OPCPA, which is the topic of Chapter 5 of this thesis. Partial results presented in this chapter were published in [149]. To the best of our knowledge, to date the pump laser described in this chapter is the highest energy picosecond source operating at

2 µm. It was also the first 2 µm laser to be used to pump a long wavelength OPCPA [35].

The outline of the chapter is as follows: first, the motivation for developing new laser sources specifically designed for pumping mid-IR OPCPA are discussed. Second, the properties of the most promising laser media emitting around 2 µm are reviewed. The impact of these properties on the laser architecture and the suitability of these materials for the generation of high energy, picosecond pulses is examined. Next, the experimental results are presented. The front-end of the CPA line is shown, consisting of a fibre laser and a temporal stretcher. A first amplification stage in the form of a fibre pumped Ho:YLF regenerative amplifier yielding mJ level pulses is described. Next, several development stages of a cryogenic booster amplifier delivering up to 260 mJ of pulse energy are presented. Finally, two different compressor setups, based on a chirped volume Bragg grating and dielectric coated diffraction gratings are described.

4.1 REQUIREMENTS FOR PUMPING MID-IR OPCPA

As we have mentioned, common near-IR OPCPA pump sources based on Yb- or Nd- doped media are not well suited for pumping long wavelength OPAs due to a lack of suitable nonlinear crystals and low efficiency. Nonetheless, considerable efforts are required for developing a new pump source with the stringent requirements placed on OPCPA pumps lasers. In order to justify this effort, in this section the benefits of using a longer wavelength for pumping mid-IR OPCPA are discussed.

The total energy transferred from pump to signal and idler in an OPCPA depends on several parameters: phase-matching, temporal and spatial matching of pump and seed, nonlinearity of the interaction medium, intensities of the beams, losses in the system, and so on. However, the ratio of energy transferred from the pump to the signal and idler beams is exclusively determined by the wavelength of the three interacting beams. This consideration is key when choosing a pump source for an OPA, particularly for amplification at long

wavelengths. As explained in Chapter 2, energy conservation during the OPA process requires that $1/\lambda_p = 1/\lambda_s + 1/\lambda_i$. A common way to interpret this relation is that for every pump photon involved in the nonlinear process, the ratio of energy transferred to the signal and idler is λ_p/λ_s and λ_p/λ_i respectively. The implication for parametric amplification is that the energy transfer from pump to idler is inversely proportional to the distance between their respective centre wavelengths.

A simple calculation can be used to illustrate the impact of the pump laser wavelength. As an example, consider the 7 μm seed laser described in Chapter 3. Using a pump operating at 1 μm, the generated signal wave would have a wavelength of 1.16 μm. The ratio of energy transfer from the pump would be 0.14 and 0.86 to idler and signal respectively. Assuming a typical value of 15% overall efficiency, this leads to a total energy transfer of only 2.1% to the longer wavelength. Using a 2 μm pump source on the other hand, which leads to a signal wavelength of 2.8 μm, doubles the energy transfer to the idler to 4.2%. This is a very significant difference considering the strict requirements many experiments place on the output energy of the driving laser. Consequently, in order for the OPAs to be efficient it is highly desirable for the pump laser of a mid-IR OPCPA to have an operating wavelength as close as possible to the output wavelength.

4.2 LASER GAIN MEDIA FOR HIGH ENERGY OPERATION AT 2 μM WAVELENGTH

The investigation of gain media emitting in the 2 μm region has been an active area of laser development since the 1960s, largely driven by applications in remote sensing and medical applications [150]. The rare earth ions Ho^{3+} and Tm^{3+} were identified in the early days of the laser as dopants that could be used for operation in this spectral range [137, 138]. Tm-doped media exhibits strong absorption at 790 nm, allowing for convenient diode pumping. However the cross-relaxation processes that are dominant in these materials are better

suited to a fibre-based architecture [151, 152]. In addition, crystals such as Tm:YAG exhibit an emission cross section over an order of magnitude lower than Ho-doped media [139], leading to lower gain and higher saturation fluence. The use of Ho-doped media on the other hand, was hampered until the early 2000s by a lack of high power lasers with an emission wavelength compatible with the corresponding absorption bands. Co-doping with Tm was used to overcome this limitation, but the resulting up-conversion losses have limited the performance of these lasers [153, 154]. The development over the last two decades of commercial Tm-fibre lasers operating around 1.9 µm has enabled direct pumping of Ho-doped crystals [141, 142].

Ho:YAG and Ho:YLF are the most established Ho-doped crystals for high peak power operation. Recent experiments have also shown promising results using CaF_2 as host [155, 156]. These results using Ho:CaF_2 are however preliminary, and this section will focus on the commercially available crystals Ho:YAG and Ho:YLF. In the context of laser media for an OPCPA pump source, both of this materials are attractive due to their comparatively large emission bandwidth, suitable for picosecond operation, and their compatibility with CW fibre laser pumping. Table 2 shows the main properties affecting laser design for Ho:YLF and Ho:YAG. For comparison purposes, the main properties of a popular laser material for OPCPA pump lasers, Nd:YVO_4, are also shown. Substantial differences between Ho-doped media and Nd:YVO_4 can be seen in several key characteristics, such as the emission cross section σ_{em} and the excited state lifetime τ_l, for which there are several orders of magnitude difference between the two types of gain media. The following section will address the impact these parameters have on laser design.

4.2.1 *Emission and absorption cross-section*

The emission and absorption cross-sections σ_{em} and σ_{abs} are arguably the most critical parameters of a laser medium. As can be seen in Tab. 2, the emission cross-section is nearly two orders of magnitude lower

	Ho:YLF	Ho:YAG	Nd:YVO_4
σ_{em} (m^2)	$18{\cdot}10^{-25}$	$9.8{\cdot}10^{-25}$	$11.4{\cdot}10^{-23}$
σ_{abs} (m^2)	$1.2{\cdot}10^{-24}$	$1.2{\cdot}10^{-24}$	$60{\cdot}10^{-24}$
τ_l (s)	$14{\cdot}10^{-3}$	$7{\cdot}10^{-3}$	$90{\cdot}10^{-6}$
Q_d (%)	5	10	25
κ (W/m·K)	6	14	5.1
α (K^{-1})	$(8 \times 13){\cdot}10^{-6}$	$8{\cdot}10^{-6}$	$4.4{\cdot}10^{-6}$
Mohs hardness	4-5	8.5	5-6
Structure	Birefringent	Anisotropic	Birefringent

Table 2: List of relevant properties for laser design for room temperature Ho:YLF, Ho:YAG and Nd:YVO_4 [157, 158, 139, 140]. σ_{em} and σ_{abs} correspond to peak values for operation at 2 µm for Ho:YLF and Ho:YAG and 1064 nm for Nd:YVO_4. The thermo-mechanical properties of the host medium are assumed to be independent of the dopant ion. Q_d, quantum defect; κ, thermal conductivity; α, thermal expansion coefficient.

in Ho:YLF and Ho:YAG in comparison to Nd:YVO_4. This significant difference is expected to lead to a comparatively low gain in the Ho-doped materials. The impact of the emission cross-section can be seen in the small signal gain g_0, which is determined by σ_{em} via $g_0 = \sigma_{em}\Delta N$, where ΔN is the population difference between the energy levels involved in the laser transition per unit volume.

The implication of low gain for the design of the amplifier using Ho:YAG or Ho:YLF is that a large number of passes in the laser medium are required for efficient amplification. A regenerative amplifier (RA) approach is therefore better suited than multi-pass geometry for the Ho-doped materials since it allows for a higher number of passes. A typical RA can be configured to deliver tens to a few hundreds of passes. In addition, the optical resonator used in the RA architecture typically guarantees a good beam profile when designed to operate in the lowest order spatial mode, which as mentioned is a critical requirement of an OPA pump. This approach does however demand careful design of the RA in order to avoid unstable energy output which can plague long lifetime, low emission cross-

section materials [159]. In addition, high quality and high damage threshold optical components such as HR mirrors and Pockels cells operating around 2 μm need to be acquired. This seemingly trivial aspect should not be overlooked, since a lack of high quality optics can pose a serious challenge to the implementation of the RA.

The saturation fluence F_s is another relevant parameter of a laser medium largely impacted by the emission cross-section. The saturation fluence is defined as $F_s = h\nu/(\sigma_{em} + \sigma_{abs})$, where ν is the emission frequency, and σ_{em} and σ_{abs} refer to the emission wavelength. Note that for a true four-level system, σ_{abs} at the emission wavelength is negligible. The saturation fluence is crucial in the design of a laser amplifier since it determines the fluence required to obtain efficient extraction from the gain medium. The saturation fluence is particularly important in the context of an OPA pump source because it is related to the fluence required to saturate the amplifier. Assuming that a stable pump source is used, operating the amplifier near saturation typically improves the stability of the output by reducing seed fluctuations. From the equation above, it is clear that a low emission cross-section will lead to an increase in the saturation fluence. This can be an advantage since it implies that high energy extraction from the medium is possible. However, a saturation fluence high enough as to be comparable to the damage fluence of the optical components will pose a challenge to the amplifier design which can limit high energy operation. As an example, the saturation fluence of Ho:YLF operating at 2052 nm is $F_s = 4\ \mathrm{J/cm^2}$ while for Nd:YVO_4 operating at 1064 nm, the value is an order of magnitude lower with $F_s = 0.2\ \mathrm{J/cm^2}$.

A low gain coupled with a high saturation fluence presents a challenge to the design of the amplifier. This is particularly problematic for short-pulse operation, where the peak intensity of the pulse usually determines the optical damage threshold of the components, rather than the fluence. Indeed since fluence is optical energy per unit area, typically measured in $\mathrm{J/cm^2}$, while peak intensity is optical power per unit area, typically measured in $\mathrm{W/cm^2}$, the pulse duration of the seed pulse needs to be increased in order to reduce the peak intensity. The implication for the design of the amplifier is

that a CPA based approach is desirable for high energy operation using Ho-doped materials.

4.2.2 *Excited state lifetime*

The excited state lifetime of a laser medium is a measure of the decay time of the upper-level population. Specifically, this value is the time required for 1/e of the population to decay to a lower state. In the absence of stimulated emission, this is equal to the spontaneous emission lifetime of the medium. For this reason laser materials with microsecond level lifetimes, such as Nd:YVO_4 or Ti:Sapphire, require pulse-pumping for high energy operation. The decay rate in these materials is so large that CW pumping cannot be used to reach a significant population inversion without using impractically large pump powers. The long lifetime of the Ho-doped materials makes them suited for CW pumping. A long excited state lifetime also means that a substantial population inversion can be achieved, an attractive property allowing high energy extraction. This requires identifying a suitable high power CW source with emission wavelength matching the absorption bands of the Ho-doped materials. As previously discussed, high power Tm-fibre lasers operating around 1.9 μm are an attractive option as pump source for both Ho:YLF and Ho:YAG.

The repetition rate of the laser is also impacted by the excited state lifetime. It has been shown that regenerative amplifiers operating at a repetition period shorter than the excited state lifetime exhibit unstable amplification dynamics [159]. The underlying reason for this is that a short period in comparison to the excited state lifetime does not allow the crystal to fully reach steady-state population inversion between pulses. This leads to coupling in the amplification of subsequent pulses and pumping cycles, leading to the emergence of complex behaviour. In this regime the output of the amplifier can suffer from period doubling or a chaotic energy distribution. In the case of Yb:YAG and Nd:YVO_4, which exhibit excited state lifetimes on the order of 1 ms and 0.1 ms, the unstable regime is reached for

repetition rates above 1 kHz and 10 kHz respectively. In the case of Ho:YLF and Ho:YAG this regime would be reached for operation in the few hundred Hz range. It must be noted that these issues with stability can be partially addressed with careful design of the amplifier [160]. This has been studied in detail both theoretically and experimentally in the case of Ho:YLF, and stable high energy multi-kHz operation has been demonstrated [161, 162, 163]. However the increase in repetition rate does reduce the output energy due to the reduced time between pulses to re-establish a high population inversion. A final aspect to consider is related to heat management. As a high energy pump source for OPCPA, an output energy ranging from tens to hundreds of mJ is required. With this high pulse energy, the repetition rate needs to be carefully chosen such that the average power remains manageable both in the pump laser and the OPAs.

4.2.3 *Spectroscopic properties*

Ho-doped media operating around 2 μm wavelength at room temperature behave as quasi-three-level laser systems. Quasi-three-level lasers are characterised by a strong overlapping of the absorption and emission bands. This is caused by the proximity between the ground state and lower lasing level leading to non-negligible thermal population in the lower lasing level, as opposed for example true four-level lasers where the lower lasing level is an excited state with negligible thermal population (Fig. 11). This implies that a certain level of pump intensity is required simply to overcome the lower lasing level thermal population and achieve inversion, rather than contributing to gain. However, excessive pumping can lead to bleaching of the ground state population, causing the medium to become transparent at the pump wavelength. In fact, a trade-off exists between efficient pump absorption and gain. In the case of Ho:YLF, calculations have shown that 22% of the Ho^{3+} ions need to be excited in order for gain to occur, while the medium will become transparent at the pump wavelength if this value exceed 56% [144]. The upside of the quasi-three level nature of the Ho-doped media is that the quantum defect for these materials is typically low. In the case of

Nd:YVO_4 pumped at 808 nm and emitting at 1064 nm, the quantum defect is 25%, while for Ho:YLF and Ho:YAG these vales can be as low as 5% and 10% respectively. These small values of quantum defect can lead to a high power efficiency and reduced thermal load in the laser medium.

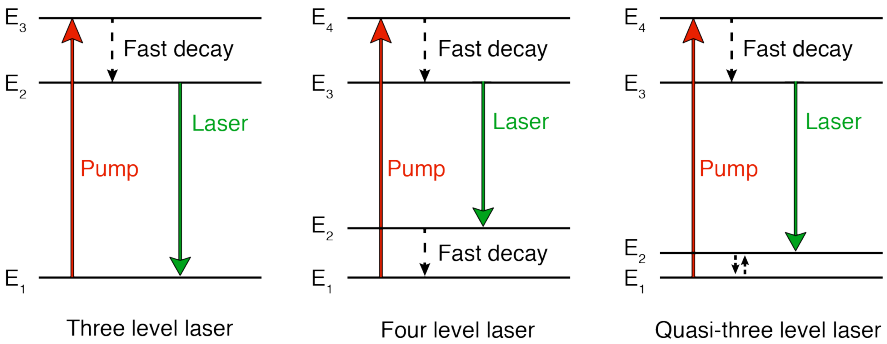

Figure 11: Energy level diagram of different laser systems: (left) where the laser transition ends on the ground state, (middle) where the lower lasing level is decoupled from the ground state and (right) where the lower lasing level is close enough to the ground state to be susceptible to thermal population. Typically, the fast, non-radiative decay times are 10^{-11} s to 10^{-14} s depending on the transition and medium.

Cooling of the gain medium can dramatically improve the performance of a quasi-three level laser system by reducing the thermal populating of the lower lasing level. In general, cooling also leads to an increased thermal conductivity and reduced thermal expansion of the gain medium, reducing beam distortion and other heat-related issues. This approach has been demonstrated using other quasi-three-level systems such as Yb:YAG [164, 136]. Early demonstrations of lasing in Ho-doped media were in fact performed at 77 K [137, 138]. In more recent work, cryogenic cooling of Ho-doped media has been successfully used to improve the performance of Ho:YLF [146, 149], Ho:YAG [165] and Ho:CaF_2 [155]. Figure 12 shows the absorption cross-section of Ho:YLF around the emission wavelength of 2052 nm from room temperature to cryogenic temperature. The data confirms that absorption at the emission wavelength reduces to negligible

values, but only after cryogenic temperatures are reached. While cryogenic cooling will clearly lead to an improved performance of the gain medium, the considerable engineering complexity this ads to the laser system needs to be taken into account.

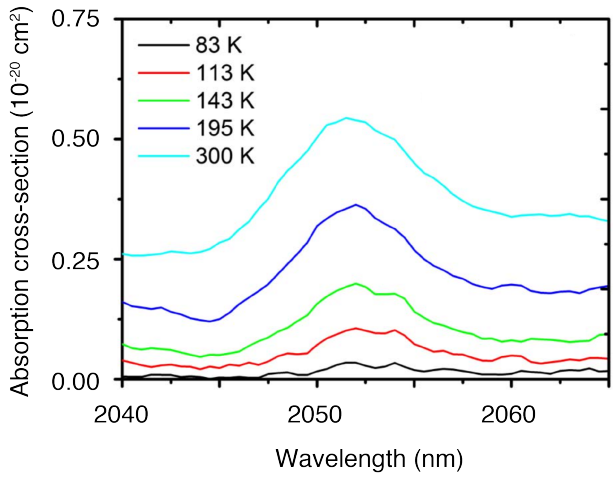

Figure 12: Ho:YLF absorption cross-section as a function of temperature. The measurements were performed using a 5-mm-thick, 0.5 at. % doped sample. The incoming light polarisation was along the c-axis of the crystal and propagation along the a-axis [149].

4.2.4 *Thermo-mechanical properties*

The mechanical properties of Ho-doped media are largely determined by the host material. Both YAG and YLF have been extensively studied with a variety of laser systems using different dopants, pumping schemes, cooling techniques, etc. YAG, an isotropic synthetic garnet, is known for being an extremely hard material with good thermal properties. The thermal conductivity is over twice as high as both YLF and YVO_4 and the thermal expansion coefficient of YAG is isotropic. This is not the case of YLF, where an anisotropic thermal expansion can cause stress in the crystal under high power pumping conditions, leading to optical aberration and possible damage of the crystal. In addition YLF, as other similar fluorides, is a comparatively

soft and brittle material. On the other hand, thermal lensing in YLF is weaker than in YAG and under equal pumping conditions the lower quantum defect of Ho:YLF compared to Ho:YAG will lead to less heat being generated in the crystal. Crucially, YLF is birefringent while YAG is isotropic and prone to thermally induced birefringence, which can lead to depolarisation effects under high power pumping conditions.

4.2.5 *Choice of laser gain medium*

The main properties of Ho:YAG and Ho:YLF and their impact on laser design have been covered in the previous section. In terms of gain and saturation fluence, Ho:YLF is a more attractive material than Ho:YAG due to it's twice larger emission cross-section. The excited state lifetime on the other hand is twice as long in Ho:YLF than in Ho:YAG. The effect however this parameter has on the choice of gain media is not as clear-cut as the emission cross-section. A long excited state lifetime allows large energy storage but places some constraints on the repetition rate at which the laser can operate. This means that Ho:YAG can be operated at a higher repetition rate than Ho:YLF before the bifurcation regime is reached. The difference however is slight in comparison with other media such as Nd:YVO_4 or Ti:Sapphire, which can comfortably operate at multi-kHz repetition rates. Higher repetition rates than a few hundred Hz are possible using Ho:YLF and Ho:YAG , but at the expense of stability and output energy. In terms of hardness, Ho:YAG is a superior material to the more brittle Ho:YLF. The thermo-mechanical properties of Ho:YAG are also better than Ho:YLF, but the latter exhibits a weaker thermal lens and a smaller quantum defect. In short, the comparison of Ho:YLF and Ho:YAG yields similar materials with good potential for high energy operation at 2 μm. Ho:YLF was finally chosen as material for the pump laser mainly for two reasons: the better gain and energy storage characteristics due to the higher emission cross-section and longer excited state lifetime, and the natural birefringence guaranteeing a clean polarisation throughout the amplifier line.

4.3 EXPERIMENTAL RESULTS

4.3.1 *Overview of laser architecture*

The previous section has highlighted some of the strengths and weaknesses of Ho:YLF as a gain medium for a high energy 2 μm OPCPA pump source. The fibre seeder for the amplifier line, described in the following section, delivered pulse energies of a few nJ. In order to seed a high energy amplifier stage potentially delivering up to hundreds of mJ, a reasonable pulse energy required from the first amplification stages is on the order of a few mJ. This requires a first amplifier stage with a gain on the order of 10^6. Due to the low single pass gain expected from Ho:YLF, a multi-pass arrangement is clearly unsuitable. As mentioned, a RA approach is better suited due to the high number of passes it allows and good beam quality this arrangement typically delivers. The high saturation fluence of Ho:YLF also demands careful control of fluence in the amplifier line for picosecond operation. Since the only parameter that can be adjusted in order to tolerate a high fluence together with a manageable peak power is the seed pulse duration, a CPA approach is necessary. This is a significant practical challenge to be overcome due to the low efficiency of diffraction gratings currently available for use at 2 μm wavelength. Finally, the quasi-three level nature of Ho:YLF presents an obstacle to high energy amplification in a multi-pass geometry. As discussed, cryogenic cooling of the gain medium can significantly improve the gain in Ho:YLF. As a compromise between simplicity and efficiency, room temperature operation for the RA and cryogenic cooling for the booster amplifier was chosen. An overview of the laser architecture is shown in Fig. 13.

4.3.2 *Front-end of CPA line*

The seeder for the 2 μm amplifier line, common to both the pump and OPAs, was described in the previous section. A detailed description of the fibre laser can be found in [68]. The narrowband output of the fibre laser carried an average power of 500 mW, corresponding to

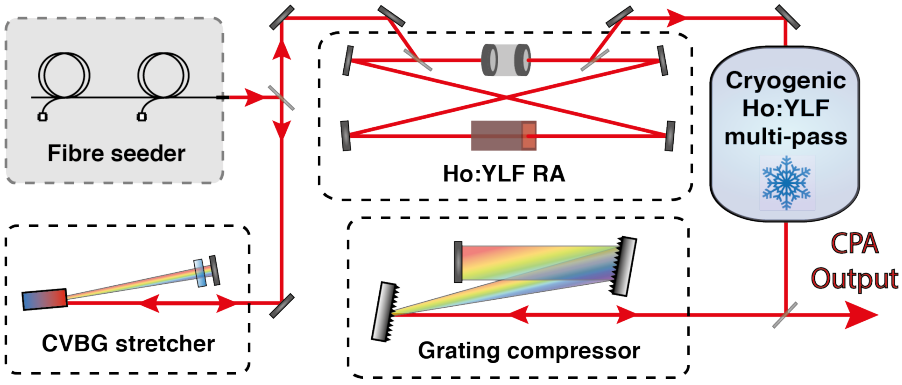

Figure 13: Schematic of the 2 μm OPCPA pump source featuring a Tm/Ho-fibre seeder, a CVBG stretcher, a Ho:YLF RA, a cryogenic Ho:YLF multi-pass amplifier and a grating compressor.

5 nJ at the repetition rate of 100 MHz. The spectrum of the pulses at the output of the fibre laser was measured with an FTIR spectrometer and liquid N_2 cooled MCT detector. The spectrum exhibited a 1.5 nm FWHM bandwidth centred around 2052 nm with small side-lobes around 2049 nm and 2055 nm. The side-lobes were attributed to the onset of nonlinear effects in the fibre amplifier. An intensity auto-correlation was used to measure the pulse duration and revealed a FWHM of 8 ps. This corresponded to 5.5 ps pulse duration assuming a Gaussian temporal profile.

The stretcher for the CPA line was based on a chirped volume Bragg grating (CVBG). The use of a CVBG as dispersive element instead of diffraction gratings provides several advantages, including a simpler and less sensitive alignment, a high efficiency and smaller footprint. The CVBG had a 5 x 8 mm^2 clear aperture and a broadband AR coating around 2050 nm. The design chirp rate was 150 ps/nm and the operating wavelength for use at normal incidence was 2053.5 nm. The Bragg condition for the shorter seed wavelength was met at an angle from normal incidence. Due to the moderate power levels used and low absorption in PTR glass, no active cooling was necessary. At the output of the fibre laser the beam was collimated and subsequently directed into the stretcher assembly. In order to use the CVBG stretcher in a two-pass configuration, the p-polarised 2 μm

beam was sent through a thin film polariser (TFP) and reflected from the CVBG at a small angle of 7° towards a quarter-wave plate (QWP) and reflecting mirror at 0°. The QWP was rotated such that the beam reflected back into the CVBG for the second pass was s-polarised and therefore ejected from the stretcher by the TFP. The overall efficiency of the compressor was 85%. The main factor contributing to the losses in the stretcher was the transparency of the CVBG at wavelengths outside of the 1.5 nm acceptance bandwidth around 2052 nm. The spectral side-lobes were filtered out by the CVBG. An intensity autocorrelation was used to measure the stretched pulses, which exhibited a FWHM of approximately 170 ps. A Rubidium Titanyle Phosphate (RTP) Pockels cell (PC) pulse picker at the output of the stretcher was used to reduce the repetition rate to 100 Hz before injection into the regenerative amplifier.

4.3.3 *Regenerative amplifier*

A ring resonator geometry with separate injection and ejection ports was chosen for the regenerative amplifier to minimise the possibility of sending an amplified pulse back into the fibre laser. A schematic of the layout is shown in Fig. 14. An RTP Pockels cell (PC) operated at half-wave voltage was employed to control injection and ejection of the pulses using two thin-film polarisers (TFP) and a half-wave plate. If no voltage was applied to the PC, the s-polarised seed pulses injected into the cavity made one roundtrip before being ejected. When a suitable voltage was applied to the PC, the seed pulses circulated inside the cavity until ejection. The total length of the cavity was 2.7 m, leading to a roundtrip time of 9 ns. The active medium consisted of a 3.5 cm long, 0.5% doped Ho:YLF crystal. The crystal was mounted in a water-cooled copper mount and kept at a constant temperature of 16 °C. The c-axis of the crystal was aligned horizontal and the pulses propagated along the a-axis. The TFPs ensured that only p-polarised light could circulate in the regenerative amplifier.

The pump laser was a diode-pumped CW Tm-fibre laser delivering up to 30 W of unpolarised light at 1940 nm (IPG Photonics).

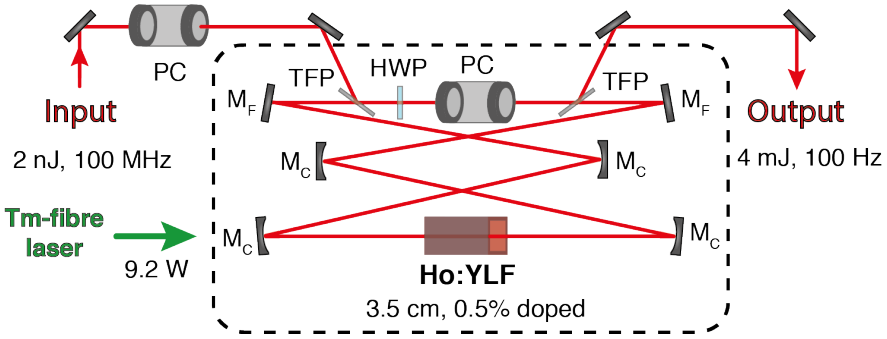

Figure 14: Layout of the 2 µm Ho:YLF ring regenerative amplifier; TFP, thin-film polariser; HWP, half-wave plate; PC, Pockels cell; M_F, flat mirror; M_C concave mirror.

After a short propagation distance, pointing fluctuations and beam profile distortions in the 1940 nm pump beam were observed. The distortions and pointing fluctuations were increasingly severe at higher powers. This behaviour was attributed to an absorption line in water around 1940 nm, leading to heating and turbulence in the pump beam path. This effect could be somewhat mitigated using a fan to cool the air. However, in order to avoid this issue and to improve the general stability of the laser, it was decided to keep the pump beam path in a low-humidity controlled atmosphere. A small airtight container pumped by a constant flow of dry air was built around the setup allowing a stable humidity level of 10% to 15% to be maintained. The dichroic mirrors used in the cavity were HR coated at 2052 nm and AR coated at 1940 nm, allowing longitudinal pumping of the active medium.

Figure 15 shows the output energy from the RA as a function of pump power and the number of passes required to reach saturation. Using a pump power of 9.2 W, the 2 nJ seed pulses from the CVBG stretcher were amplified to 4 mJ after 36 passes in the regenerative amplifier. Higher output energies of up to 5.5 mJ were achieved with increased pumping, but day-to-day the amplifier was operated at 4 mJ in order to keep the peak intensity in the cavity below 5 GW/cm^2. A Gaussian spatial profile was measured at the output of the regenerative amplifier. The power and pulse-to-pulse stability

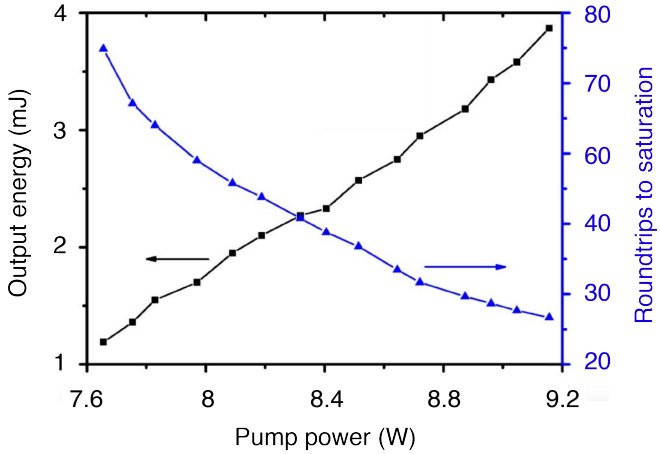

Figure 15: Measured output energy (black square) and number of passes required to reach saturation (blue triangle) of the Ho:YLF regenerative amplifier [149].

were measured using a pyro-electric detector and fast photodiode respectively. These measurements revealed fluctuations of less than 2% rms over 2 hours. The performance of the regenerative amplifier was entirely reproducible day-to-day.

4.3.4 *40 mJ, single-pass cryogenic amplifier*

Ho:YLF behaves as a quasi-three-level gain medium at room temperature, leading to a high thermal load in the crystal and low gain, making multi-pass arrangements for further amplification challenging. The coupling between the ground state and lower lasing level can be greatly reduced via cryogenic cooling, effectively turning Ho:YLF into a four-level system and dramatically improving its spectroscopic and mechanical properties. Based on these considerations, in a first attempt to boost the output of the RA to higher energies, a single-pass, cryogenically cooled Ho:YLF amplifier was built. A cryogenic cooler with a capacity of 50 W was used to achieve cryogenic temperatures. The active medium consisted of a 3.5 cm-long 1% doped Ho:YLF crystal with a clear aperture of 10 x 10 mm^2, AR-coated for both the pump and lasing wavelengths. Similarly to the RA, the

c-axis of the crystal was placed horizontally in order to operate the crystal in π-polarisation. The crystal was inserted in a copper mount and mounted to a cold finger inside a small vacuum chamber. The temperature of the crystal was monitored using a thermocouple attached to the copper mount and kept at a temperature of -230 °C under no load conditions. Figure 16 shows the schematic layout of the amplifier.

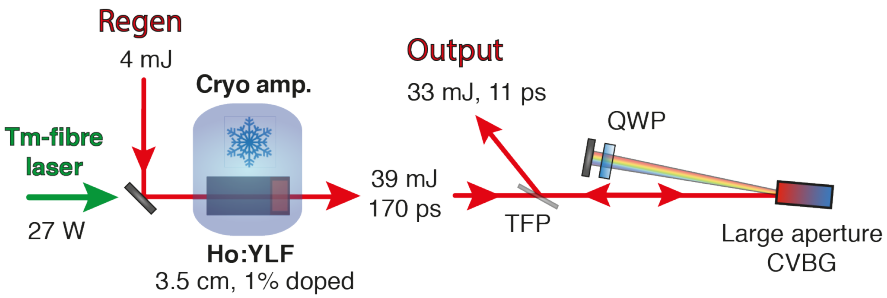

Figure 16: Layout of the 2 µm Ho:YLF cryogenic single-pass amplifier and large-aperture CVBG compressor; TFP, thin-film polariser; QWP, quarter-wave plate.

A diode-pumped Tm-fibre laser providing up to 120 W of CW unpolarised light at 1940 nm was used as the pump source (IPG Photonics). The pump beam was collimated at the output of the fibre laser using CaF_2 lenses and adjusted to a beam radius of 0.7 mm FWHM using a telescope arrangement. The unpolarised beam was p-polarised after passing through a TFP and HWP. Using a pump power of 27 W the amplifier yielded 39 mJ of pulse energy, corresponding to a single-pass gain of approximately 8. The power stability was measured over half a million shots using a pyroelectric detector and revealed fluctuations less than 0.8% rms and peak-to-peak fluctuations less than 3%. A knife-edge beam profile measurement showed that the Gaussian spatial profile from the RA was left unaffected by the amplification process. Higher energies could not be achieved in this configuration due to damage of the optical elements after the amplifier at higher pump powers.

An AR-coated CVBG with identical specifications to the CVBG used in the stretcher (2053.5 nm design wavelength and chirp rate of 150 ps/nm) was employed for compression. For high peak power pulses, self-phase modulation can limit the use of CVBGs as compressing element. In PTR glass, this effect is typically observed above $6{\cdot}10^{12}$ W/cm^2. In order to handle the pulse energies from the booster amplifier, a CVBG with a 25 x 27 mm^2 aperture and 40 mm thickness (OptiGrate Corp.) was acquired. With these dimensions, the CVBG can in principle handle energies up to 50 mJ. The angles used in the compressor were identical to the stretcher and the footprint was 50 cm x 10 cm. The throughput of the compressor was 85%. An intensity autocorrelation was used to measure the duration of the compressed pulses. Fig. 17 shows the autocorrelation trace exhibiting a FWHM of 16 ps, corresponding to a pulse duration of 11 ps assuming a Gaussian temporal profile. We believe that a slight mismatch between the stretcher and compressor CVBGs explains the shoulders that can be seen in the autocorrelation trace. The configuration of the pump laser described in this section was successfully used to pump the mid-IR OPCPA described in the following chapter [35].

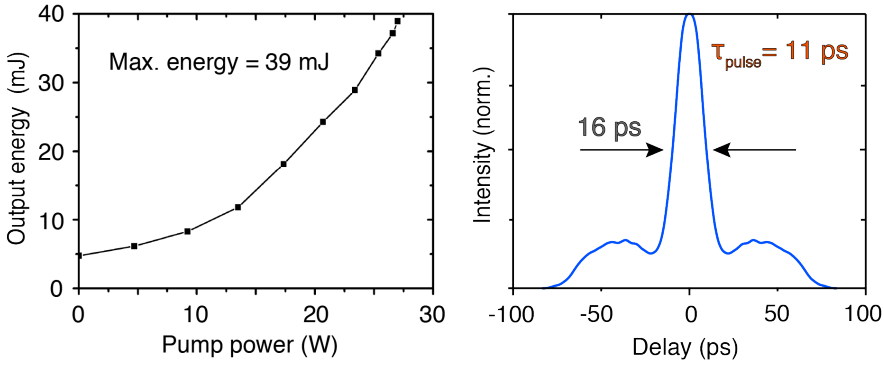

Figure 17: Performance of the cryogenic Ho:YLF single-pass amplifier: (left) output energy vs pump power and (right) intensity autocorrelation trace of the amplified pulses measured after the CVBG compressor. The FWHM of the trace was 16 ps, corresponding to a pulse duration of 11 ps.

4.3.5 *260 mJ, multi-pass cryogenic amplifier*

Scaling of the amplifier to higher energies was limited by the damage of the optical elements in the amplifier. In order to decrease the peak power and operate the booster further from the damage threshold of the optics, an increase in the seed pulse duration was required. This was achieved by adding a second pass to the CVBG stretcher prior to injection into the RA, such that the total number of reflections from the CVBG was four. The additional pass was added by placing a mirror at normal incidence at the output of the original stretcher arrangement and using an optical isolator at the input, see Fig. 18. The isolator served the purpose of avoiding feeding back into the fibre laser and separating the input and output beams. Due to the dispersion from the CVBG, the resulting pulse duration was expected to double. This was confirmed by an intensity autocorrelation which revealed a pulse duration of 340 ps, twice the duration of 170 ps measured in the previous single pass stretcher. The behaviour of the regenerative amplifier was unaffected by the increase in pulse duration.

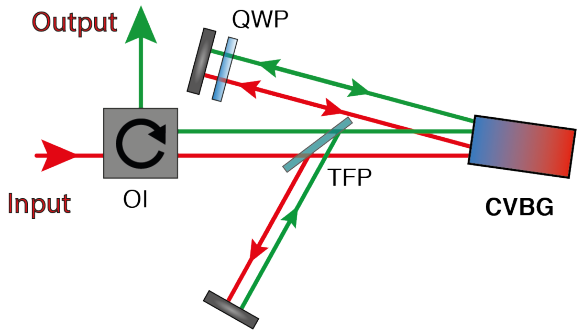

Figure 18: Schematic of the two-pass CVBG stretcher. For clarity, the first and second pass are separated and marked in red and green respectively. TFP, thin-film polariser; QWP, quarter-wave plate; OI, optical isolator

In a first attempt to increase the energy of the booster amplifier, a double-pass arrangement was implemented featuring the same Ho:YLF crystal used in the single-pass amplifier. A closed-cycle

cryostat with a cooling capacity of 100 W was employed to reach cryogenic temperatures. A thermocouple attached to the crystal was used to monitor the temperature in the amplifier, which measured a temperature of -173 °C under no load conditions. In order to reduce thermal stress on the crystal, the pumping scheme was modified to allow pumping from both sides. The unpolarised output of the 1940 nm CW Tm-fibre laser was split into two polarised beams using a TFP. A HWP was used to rotate the polarisation of the reflected beam to p-polarisation. The two beams were used to pump the crystal from both sides using 75 cm focal length lenses to achieve a beam size of 1.2 mm FWHM at the position of the crystal. At 50% of the total power available from the fibre laser, the two pump arms delivered 27.2 W and 23.5 W leading to a total pump power of 50.7 W directed toward the Ho:YLF crystal.

The amplifier was arranged in a bow-tie type geometry. A telescope was used to set the seed beam size to 0.9 mm FWHM at the position of the crystal. The output of the regenerative amplifier was sent with a small angle to a dichroic mirror that transmitted the pump and reflected the seed, which was then sent through the cryogenic amplifier such that the beams overlapped at the crystal. At the output a spherical dichroic mirror with a focal length of 2 m was used to both collimate the seed beam and transmit the second CW pump arm. After the spherical mirror, the seed beam was directed towards a rooftop mirror arrangement in order to separate the first and second passes. The return seed beam for the second pass was sent back on the 2 m spherical mirror, through the cryogenic amplifier, reflected off the flat input mirror and picked off before the input of the regenerative amplifier. The amplified beam was measured using a fan-cooled pyroelectric detector. The first pass yielded a comparable energy to the original single-pass design, with a measured power of 4.3 W, corresponding to a pulse energy of 43 mJ. At the output of the cryogenic amplifier after the second pass a maximum average power of 10.3 W was measured. This corresponds to 103 mJ at the repetition rate of 100 Hz. The stability was measured with a fan-cooled pyroelectric detector and showed an rms power stability of 0.5% at full power over 30 min. The power stability measurement is shown in Fig. 19. The increased heat load in the crystal did not lead to spatial

distortions in the beam. A measurement of the collimated beam at full power using a micro-bolometer array camera is shown in Fig. 19.

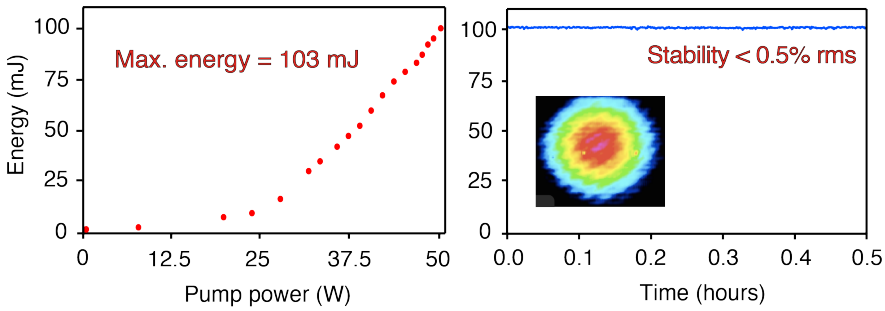

Figure 19: Performance of the cryogenic Ho:YLF two-pass amplifier: (left) output energy vs pump power and (right) power stability showing fluctuations smaller than 0.5% of the rms. The beam profile at the output of the amplifier measured with a micro-bolometer array camera can be seen in inset. The small features and fringes on the beam were artefacts caused by the filter on the camera.

Further amplification at higher powers was hindered by damage to the window of the vacuum chamber after the second pass. In order to decrease the peak power and reach higher output energies, the beam sizes were rescaled to 1.5 mm and 1.3 mm for the pump and seed respectively. A third pass was added to increase the extraction efficiency and also to reduce the thermal load on the cryogenic cooler. The maximum power available from the fibre laser was used to pump the three-pass amplifier. After separating the output of the fibre laser into two polarised beams, the average power from the pump arms was measured to be 57 W and 49.2 W, leading to a total pump power of 106.2 W. The first pass provided a similar gain to the previous amplifier designs, yielding a pulse energy of 42 mJ. The second and third passes delivered a pulse energy of 173 mJ and 260 mJ respectively providing an overall gain from the multi-pass amplifier of 65. The beam profile, shown in Fig. 20, exhibited a Gaussian profile. The stability of the amplifier, shown in Fig. 20, was measured with a fan-cooled pyroelectric detector over 20 min and revealed a power stability of 0.8%.

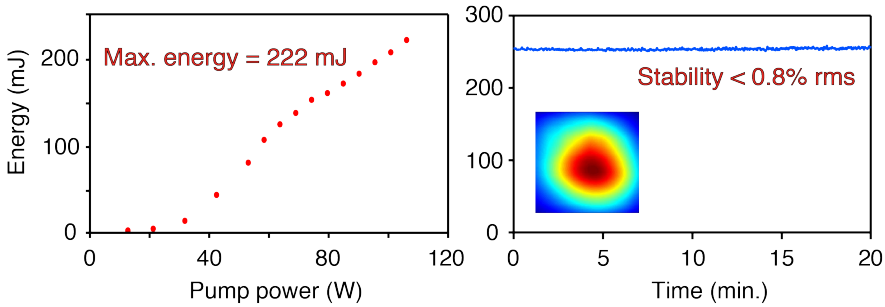

Figure 20: Performance of the cryogenic Ho:YLF three-pass amplifier: (left) output energy vs pump power and (right) power stability showing fluctuations smaller than 0.8% of the rms. The beam profile at the output of the amplifier measured with a micro-bolometer array camera can be seen in inset. The maximum output energy of 260 mJ was achieved by optimising the pump and seed overlap at full power.

The large CVBG used to compress the output of the single-pass amplifier was not suited to handle energies higher than 50 mJ due to the onset of self-phase modulation. At the time these experiments were performed, a larger CVBG could not be produced due to manufacturing constraints. Therefore, in order to compress the 100 mJ pulses, diffraction gratings designed for operation at 2 µm were required. Our previous experience with off-the shelf diffraction gratings for 2 µm was that commercially available components suffered from a low diffraction efficiency when used far from the Littrow angle that was necessary to keep a reasonable footprint. As an example, a test Treacy compressor with commercial gratings with a groove density of 600 l/mm yielded an overall efficiency of less than 10%. In order to overcome these limitations, a set of high diffraction efficiency dielectric coated gratings were developed specifically for this system (Fraunhofer IOF). Typically, grating compressors for narrow-bandwidth, picosecond pulses require large propagation distances between the gratings to achieve compression. In order to minimise the footprint of the compressor, a high groove density of 900 l/mm was specified for the diffraction gratings. The dimensions of the gratings were set to 100x75 mm^2, large enough to accommodate the full bandwidth for the picosecond pulses and in principle to handle compression of 300

mJ energy pulses.

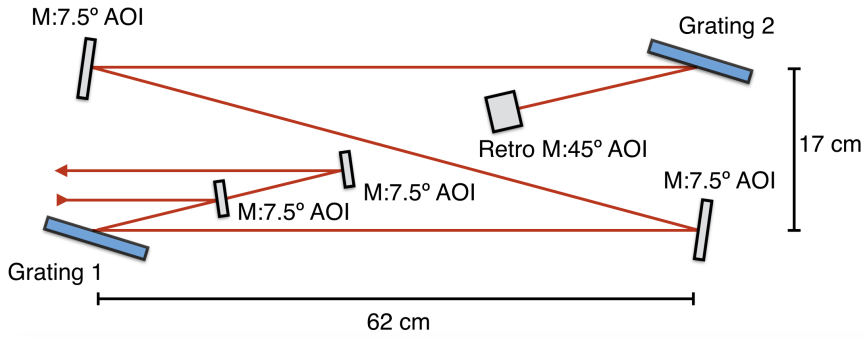

Figure 21: Layout of the 2 μm Treacy compressor featuring coated diffraction gratings and all-reflective optics.

The design of the Treacy compressor was assisted by ray-tracing calculations using a commercial software (Optica, Mathematica). The compressor was designed to compensate the 760 ps^2 of GDD introduced by the CVBG stretcher. Since several meters of propagation were required in order to achieve compression, the Treacy assembly was folded in order to keep the footprint to a reasonable area. Fig. 21 shows the layout of the compressor with a footprint of 100 cm by 25 cm. The angle of incidence on the gratings was 62° (Littrow was 67.5°) and the distance between the gratings was 1.88 m. The single reflection efficiency on the gratings was measured to be above 97% and the overall efficiency was 85%. A first test of the compressor was undertaken using an output energy of 100 mJ, yielding compressed pulses with an energy of 85 mJ. The temporal characterisation of the high energy picosecond pulses was measured using an intensity autocorrelator. The resulting measurement can be seen in Fig. 22. The AC trace exhibited a FWHM of 20 ps, corresponding to a Gaussian pulse duration of 14 ps. Experiments carried out while this thesis was being written showed the suitability of the gratings for operation at full power, delivering compressed pulses with an energy of 220 mJ [36].

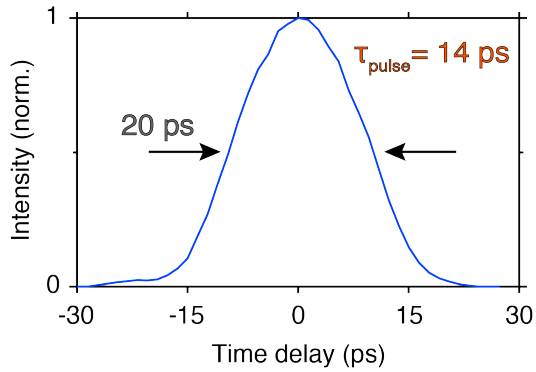

Figure 22: Intensity autocorrelation trace of the compressed pulses from the multi-pass amplifier. The FWHM of the trace was 20 ps, corresponding to an 14 ps pulse duration

5

HIGH INTENSITY, MID-IR OPCPA

5.1 INTRODUCTION

The development of pulsed sources has advanced at high speed since the early 60s. Only two years after the first experimental demonstration of the laser by Maiman in 1960 [2, 3], the first Q-switched lasers were developed [166] and soon after, in 1964, mode-locked operation was first demonstrated [167]. This breakthrough technique, which would have tremendous influence on various domains of experimental science, enabled for the first time the generation of pulses with peak powers in the GW regime, 6 orders of magnitude higher than the first laser demonstrated only four years before.

For over a decade these high peak powers set a practical limit to amplification schemes due to self-focusing effects leading to optical damage of the gain medium and optical elements. Employing techniques used in radar transmission, this obstacle was overcome in 1985 with the development of CPA [170]. Making use of schemes to tailor spectral chirp [168, 169], this technique allowed control of peak power during amplification. CPA was first demonstrated using Nd:Glass as the amplifier medium to generate 2 ps, 1 mJ pulses at a a centre wavelength of 1.06 μm. The application of this technique to new architectures and laser materials, most importantly for ultrafast science Ti:Sapphire [171, 172], extended the capability of CPA based systems to amplify a range of wavelengths to peak powers beyond the PW level [173, 174, 175, 176]. The importance of the development of CPA was recently recognised with the Nobel Prize in Physics 2018, which was awarded in part to Gérard Mourou and Donna Strickland "for their method of generating high intensity, ultra-short optical pulses".

There are however some limitations to CPA which are unlikely to be solved in the foreseeable future. Despite numerous efforts [177, 178, 179], spectral gain narrowing is still an issue in CPA which limits the amplification bandwidth of these systems, in turn limiting the peak power scalability of this architecture. A further limitation, inherent to stimulated emission based amplifiers, stems from the fact that suitable gain materials for CPA can access only a relatively small part of the optical spectrum. Many processes and application that require specific wavelength ranges would greatly benefit from having high intensity laser sources that are flexible in operating wavelength. Finally, detrimental heat-related effects such as thermal lensing and thermally induced depolarisation pose a fundamental challenge to the scalability of CPA to higher average powers.

Some of the limitations affecting CPA can be avoided using parametric processes instead of amplification via stimulated emission. The main process used to this end is OPA [180, 181], which was described theoretically in Chapter 2. The are several important differences with stimulated emission-based amplification. The amplification bandwidth and operating wavelength is not determined by laser transitions but rather by the dispersive properties and transparency of the nonlinear medium. This gives far greater flexibility in terms of operating wavelength. In practice, this flexibility also means that there are several degrees of freedom available which can enable enormous gain bandwidths. This property makes OPA extremely attractive for applications that require the amplification of large bandwidths and/or wavelengths that cannot be accessed by conventional laser media. In addition, parametric gain per unit length can exceed laser gain by several orders of magnitude. This leads to simplified experimental setups that only require a few millimetres of propagation in the nonlinear medium, therefore eliminating the need for complex multi-pass arrangements. Finally, in OPA the energy transfer is instantaneous and there is no energy storage in the amplification medium. Consequently the generation of heat in the amplifier is greatly reduced, given that the nonlinear medium can be chosen to be transparent at the wavelength of the pump as well as the signal and idler. The phenomenon know as quantum defect in conventional laser amplifiers inevitably leads to heat deposition in the medium. The equivalent in OPA is the generation of a third wave, which will not lead to heat if the medium is also transparent at this wavelength. Thus, the heat produced in an OPA is

caused only by parasitic absorption.

The concept of OPCPA is the integration of OPA and CPA. This technique was first demonstrated in 1992 [129] and it quickly became clear that it could be used to overcome some of the limitations of conventional laser amplifiers [182]. OPCPA technology has experienced remarkable progress in the last 25 years. It has enabled the amplification of few-cycle pulse supporting bandwidths up to energy levels of hundreds of millijoules [133, 134, 183] and unprecedented repetition rates [131, 184]. Most importantly in the context of this thesis, OPCPA has enabled the development of laser systems operating at wavelengths previously inaccessible to high intensity laser systems [29, 30, 31, 32]. In the last few years, OPCPA has become an established technology and it is becoming clear to the ultrafast community that these systems are capable of competing with Ti:Sapphire lasers.

The topic of this chapter is the demonstration of mid-IR OPCPA pumped by a 2 µm wavelength laser. To the best of our knowledge, this was the first demonstration of an OPCPA pumped directly at 2 µm and is currently the OPCPA with the longest operating wavelength. The main results of this chapter were published in [35]. The chapter structure is as follows: first, the target specifications for the laser system as a driver for strong-field experiments are discussed. Next, an overview of the architecture is given as well as a summary of the results presented in the previous chapters relating to the pump and seed laser sources. The design aspects of the amplification line are discussed next. This includes the stretch factor for the seed pulses, the choice of the nonlinear crystal and the geometry and nonlinear interaction used in the OPAs. The amplifier line, consisting of three ZGP based OPAs pumped by the 2 µm laser, is described. The design and implementation of a grating based compressor is discussed. Finally, the characterisation of the mid-IR OPCPA output is presented.

5.2 TARGET PARAMETERS

The main application envisioned for this laser is as a driver for strong-field experiments. The target parameters listed below were chosen to satisfy typical requirements for these experiments, particularly as a

driving source for HHG.

Pulse duration
Strong-field experiments require laser sources delivering short, energetic pulses to reach the high intensities needed to drive extreme nonlinear processes. Pulses with a temporal width comparable to the duration of an optical cycle are highly desirable for many experiments [48] . This is particularly relevant for processes that are directly sensitive to the electric field [185, 186] since the added effect of multiple optical cycles in longer pulse will tend to wash out the direct influence of the electric field. The definition of the so-called few-cycle regime is somewhat arbitrary. Typically, it is considered to apply to pulses containing less than 4 optical cycles in their intensity envelope FWHM. An optical cycle at a wavelength of 7 μm is 23.5 fs in duration, therefore the target is amplifying sufficient bandwidth to support a compressed pulse duration below 100 fs.

Pulse energy
The cut-off frequency in HHG can be extended by driving the process using long wavelength pulses [12, 14]. However, theoretical and experimental studies have shown that this comes at the cost of decreasing the harmonic yield, which is already low when the process is driven in the near-IR. This decrease is due to multiple effects, most importantly the spreading of the electron wavepacket and the effect of the magnetic field component for high values of U_p. This can be partially compensated for by taking advantage of more favourable phase-matching conditions at longer wavelengths [13], but even in these favourable conditions it is expected that the process will have a comparatively low conversion efficiency. It is therefore highly advantageous to have a high energy driver. For first demonstration, the target for the system is to deliver at least a hundred microjoules of energy in the compressed mid-IR pulses.

CEP stability
The capability of delivering a reproducible electric field from pulse to pulse is crucial in laser systems operating in the few cycle-regime [53]. This can be a necessity for the investigation of strong-field phenomena that depend on the electric field rather than on the in-

tensity envelope. Active control of the CEP can be obtained through feed-back loop stabilisation schemes that measure the CEP drift and correct it by adding a controlled amount of dispersion or adjusting the cavity length [54]. As shown in Chapter 2, passive CEP stabilisation on the other hand, consists of directly generating CEP stable pulses exploiting the phase properties of DFG [187, 55]. The latter approach was chosen for the seed laser described in Chapter 3 since it leads to a simpler and more robust architecture. Given that OPA is a phase-preserving nonlinear process, the output of the laser system is expected to be CEP stable.

5.3 OVERVIEW OF LASER ARCHITECTURE

A schematic diagram of the mid-IR OPCPA is shown in Fig. 23. The OPCPA described in this chapter relied on the laser systems presented in chapters 3 and 4: a fibre-driven broadband mid-IR seed source and a high energy picosecond 2 μm pump laser respectively. The front-end of the system was an all-fibre laser based on a 1.55 μm Er:fibre oscillator. The fibre laser delivered three outputs originating from the common Er:fibre oscillator. Two of these outputs, at 1.55 μm and 2.03 μm, were broadband and used to drive the mid-IR DFG stage, while the third output at 2052 nm was narrowband and used to seed the pump amplifier line. This arrangement based an all optical synchronisation guaranteed optimum temporal overlap and gave the overall system robustness in comparison to other OPCPAs relying on electronic synchronisation between seed and pump pulses. The pump laser used in this first demonstration of the OPCPA had two amplification stages. The first was a ring regenerative amplifier amplifying the output of the fibre laser by several orders of magnitude from nanojoule to millijoule energy levels followed by a cryogenically cooled single pass amplifier boosting the energy to several hundreds of millijoules. After temporal stretching using bulk dispersive media, the seed generated in the DFG stage was directed to the amplifier line, consisting of three OPAs pumped by the 2 μm laser. Due to the driving pulse for the DFG originating from a common oscillator, it was expected that the seed for the OPA line would be CEP stable.

As discussed in Chapter 2, OPA is a phase-preserving process and therefore should not affect the seed CEP stability. After amplification the mid-IR pulses were re-compressed using a positive dispersion grating compressor assembly. The setup was kept in a low humidity controlled environment in order to avoid absorption in the mid-IR from ambient water vapor.

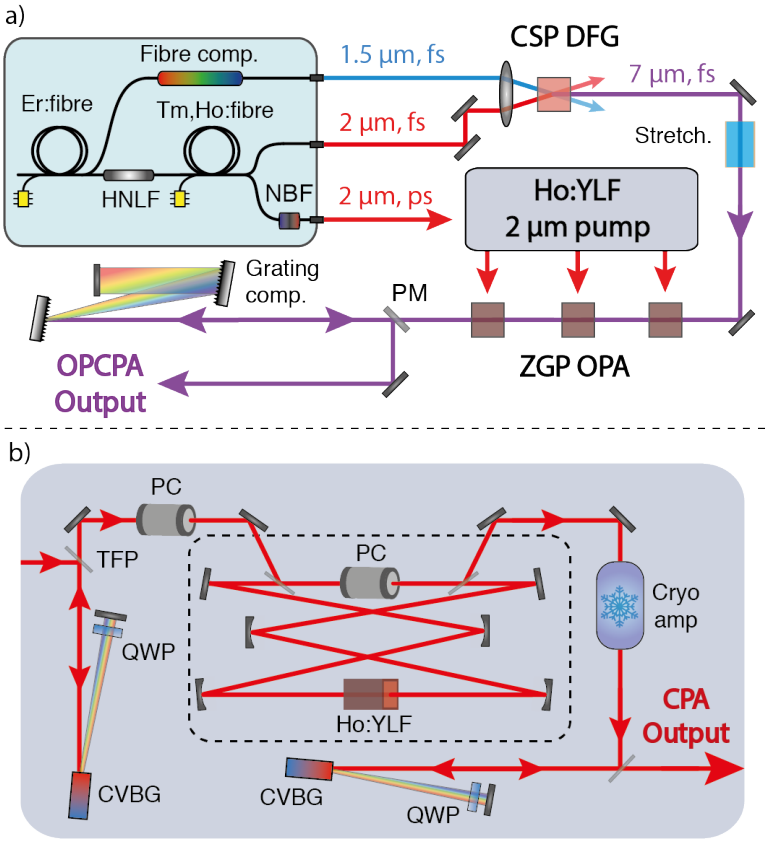

Figure 23: Layout of the mid-IR OPCPA; HNLF, highly nonlinear fibre; NBF, narrow-bandwidth filter, Stretch., stretcher; PM, pick-off mirror; Comp., compressor. b) Detailed layout of the Ho:YLF pump laser; QWP, quarter-wave plate; CVBG, chirped volume Bragg grating; PC, Pockels cell; TFP, thin-film polariser [35].

5.4 PARAMETRIC AMPLIFICATION

5.4.1 *Pump-to-seed pulse duration ratio*

OPCPA architecture requires the seed pulses to be temporally stretched prior to amplification. The pump-to-seed pulse duration ratio is an important design aspect of the OPCPA and has a large impact on the overall performance of the laser system due to the quasi-instantaneous nature of OPA. Moreover, the amplified bandwidth is also dependent on the pump-to-seed pulse duration ratio due to the chirp in the seed pulses. Parasitic superfluorescence, which is typically generated in an OPA and can become a problem in high gain amplifiers, is also strongly related to temporal/spatial overlap. The design of a stretcher scheme is a trade-off, since in general one-to-one matching of the pump and seed pulse durations leads to a greater efficiency, while a shorter seed pulse leads to broader amplification bandwidths. In order to choose the optimum stretch factor for the seed, a nonlinear wave propagation code [122] was used to numerically simulate the DFG and OPA processes. In agreement with the experimental measurements presented in previous chapters, the pump was assumed to be a transform limited gaussian pulse with a temporal duration of 11 ps while the seed was modelled using the measured DFG spectrum. The target was amplification of enough bandwidth to support a sub-100 fs pulse in an undepleted, 5 mm ZGP based OPA. The simulations suggested that a seed pulse duration of 6 ps together with an 11 ps pump pulse allows amplifying sufficient bandwidth to support a sub-100-fs pulse.

Various experimental schemes have been used in CPA-based architectures to temporally stretch the seed pulses. Systems operating in the near-IR typically use grating-based positive dispersion stretchers and negative dispersion compressors, the so-called Martinez and Treacy assemblies respectively [168, 169]. Other arrangements using bulk material, chirped mirrors, pulse shapers, fibre stretchers usually in combination with gratings are also used. Working in the mid-IR however, places some practical constraints on the materials and components that can be used for stretching and compressing. Gratings, mirrors and other optical components generally exhibit

a worse performance in the mid-IR than in more common spectral ranges, particularly for ultrafast applications. Practical limitations such as the lack of fluorescent cards must also be taken into account. In the setup described in this chapter, the average power of the seed from the DFG at the stretcher was measured to be around 15 mW, which would be sufficient for the fluorescent alignment cards used in the near-IR. At 7 μm however, the use of detector cards based on thermochromic liquid crystals, which are far less convenient to use, is required. In addition the dispersion inside the stretcher causes the beam to spread, lowering the fluence even further. As a consequence, alignment in the mid-IR at low average powers is particularly difficult, making construction of a grating or prism based stretcher/-compressor a challenge.

For these reasons, bulk media was chosen for stretching, while a grating assembly was chosen for compression where we expected to have higher average power levels. Several materials which are transparent in the mid-IR can be used for bulk stretching. Table 3 shows a list of commercially available materials. Bulk BaF_2 was chosen for stretching due to its low Fresnel losses, its isotropic structure and high GVD in the mid-IR (700 fs^2/mm at 6.5 μm). In addition, BaF_2 is extensively used as an optical component for long wavelength applications and large aperture, high quality polished samples can be obtained commercially. According to calculations based on the dispersive properties of BaF_2, propagation through 12 cm of this material stretch the seed to the target pulse duration of 6 ps. An uncoated 6 cm long piece with an aperture of 2.5x2.5 cm^2 was obtained in order to be used in a two-pass arrangement.

5.4.2 *Choice of nonlinear crystal*

Due to the large bandwidths and high intensities involved, the nonlinear crystals used for broadband OPA need to be chosen carefully. This is particularly true for mid-IR applications where commercially available crystals and coatings are scarce. The available nonlinear crystals for mid-IR applications were discussed in Chapter 3 (see

Dispersive medium	GDD (fs^2)	TOD (fs^3)	GDD/TOD
Ge	$6{\cdot}10^4$	$2.5{\cdot}10^5$	0.24
GaAs	$6{\cdot}10^3$	$4{\cdot}10^5$	0.02
BaF_2	$-7{\cdot}10^4$	$8{\cdot}10^5$	0.086
ZnSe	$-2{\cdot}10^4$	$3.5{\cdot}10^5$	0.059
KBr	$1{\cdot}10^3$	$4{\cdot}10^3$	0.28
KCl	$-2{\cdot}10^4$	$2{\cdot}10^5$	0.087
NaCl	$-3{\cdot}10^4$	$3.5{\cdot}10^5$	0.08
CsI	$-1.5{\cdot}10^3$	$4.5{\cdot}10^5$	0.03
CaF_2	$-6{\cdot}10^3$	$2.5{\cdot}10^5$	0.41

Table 3: List of dispersive materials for mid-IR bulk stretching. The dispersion coefficients shown correspond to a centre wavelength of 7 µm. The GDD/TOD ratio is useful for the choosing the appropriate grating compressor design.

Table 1). The use of a 2 µm pump laser permits the use of the positive uniaxial nonlinear crystal ZGP [102]. As a mid-IR OPA crystal, ZGP exhibits excellent linear and nonlinear properties. It has a large nonlinear coefficient (d_{eff} = 75 pm/V) and a wide transparency range reaching deep into the mid-IR (2 µm to 8.5 µm). It also has the highest thermal conductivity (36 W/mK) of any of the nonlinear crystals discussed in Chapter 3. Recent advances in fabrication have lead to the availability of high quality, polished and AR-coated samples with apertures larger than 2x2 cm^2.

Figure 24 shows the computed phase-matching curves for ZGP corresponding to the OPA process 2.052 µm - 3 µm = 6.5 µm, where the pump wavelength is fixed and the signal and idler are broadband. The calculation were performed using the SNLO software [89]. Phase-matching the shorter wavelengths of the seed spectrum, below 6.5 µm, is only possible in a Type I (o-e=e) configuration. In order to take full advantage of the broad bandwidth provided by the DFG, we resort to non-collinear geometry for the OPA in a Type I phase-matching configuration. The broadest phase-matching is obtained for

an internal non-collinear angle of α_{int}=4.3°, which corresponds to an external angle of α_{ext}=13.5° (note that α refers to the angle between the pump and the idler). For Type I interaction in a positive uniaxial crystal, the pump is the o-polarised wave while the signal and idler are e-polarised. The non-collinear geometry is usually contained in the horizontal plane for practical reasons, which forces the pump to be s-polarised and the signal and idler to be p-polarised. The geometric arrangement of the beams is shown in Fig. 24.

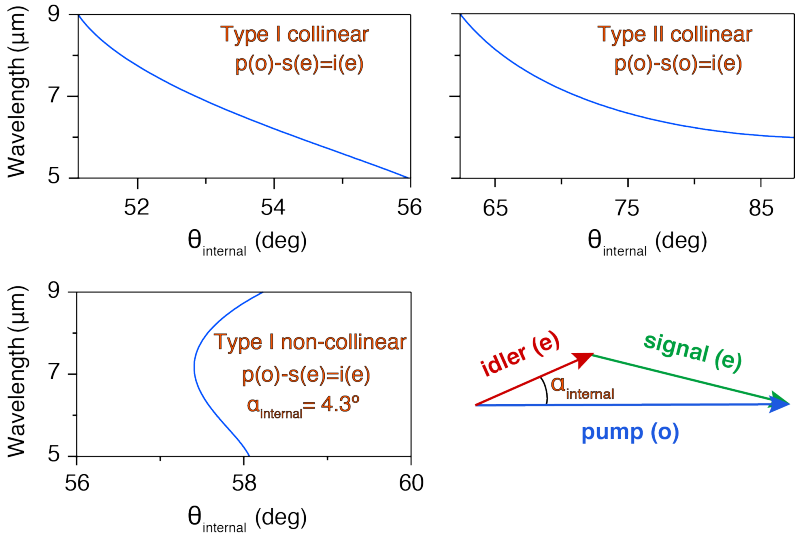

Figure 24: Phase-matching curves for ZGP corresponding to the OPA process 2.052 μm - 3 μm = 6.5 μm where the pump wavelength is fixed while the signal and idler are broadband: a) in collinear Type I, b) collinear Type II and c) non-collinear Type I phase-matching with α_{int}=4.3°; p, pump; s, signal; i, idler; o, ordinary polarisation, e, extraordinary polarisation.

5.4.3 *OPAs*

Before seeding the amplifier line, the collimated output of the DFG was directed toward a stretcher setup, which consisted of a two-pass arrangement through a 6 cm BaF_2 piece using a gold coated mirror as roof-top. Due to the low energy of the seed pulses, which was

measured to be 100 pJ after the stretcher, the pulse duration could not be measured directly before amplification. The polarisation of the DFG was rotated from s to p-polarisation before the OPA stages using a polarisation-rotating periscope arrangement featuring gold-coated mirrors.

The parametric amplifier chain was composed of three non-collinear OPAs using ZGP as the nonlinear medium. All of the crystals were AR coated for the three interacting wavelengths. Throughout the amplifier stages, the beams were conditioned using uncoated BaF_2 lenses for the seed and AR coated CaF_2 lenses for the pump beam. Due to the lack of commercial HR dielectric coatings in the mid-IR, all the reflective optics for the seed were gold coated. Damage test on the AR coated ZGP crystals revealed a LIDT of approximately 20 GW/cm^2 for the 2 μm pump pulses at 11 ps pulse duration. Taking this result into account, the peak intensity in the OPA stages was kept to approximately 16 GW/cm^2.

The first OPA consisted of a 5 mm long ZGP crystal with a usable aperture of 5x5 mm^2. The pump and seed beams were focused to 400 μm at FWHM with a non-collinear angle of α_{ext}=13.5°. The crystal was cut such that the incident seed beam was normal to the surface of the crystal. The input seed and pump energies were 100 pJ and 200 μJ respectively. After amplification an energy of 2 μJ in the mid-IR pulses was measured. This corresponds to a gain of $2{\cdot}10^4$. The second OPA consisted of a 5 mm ZGP crystal with an aperture of 6x8 mm^2. Both beams were focused to 1.8 mm FWHM. The seed and pump energies were 2 μJ and 4 mJ respectively. At the output of the amplifier, 100 μJ in the mid-IR pulses was measured. Finally, the last OPA consisted of a 3 mm ZGP crystal with an aperture of 6x8 mm^2. The beams were focused to 3 mm FWHM. The seed and pump energies were 100 μJ and 8 mJ respectively. The amplified output was measured to be 550 μJ. This corresponds to a pump energy conversion efficiency of 18 % into signal plus idler in the last OPA stage. A superfluorescence background of 5% was measured by blocking the seed. Small changes in the non-collinear angle (<1°) were found to have little impact on amplification efficiency and amplified bandwidth and the results were reproducible from day-to-day. At the

time these experiments were performed, further amplification using the full pump power was hampered by the aperture of the available OPA crystals, which allowed a maximum pump energy of 8 mJ.

Measurements of the amplified spectrum with an FTIR spectrometer were not possible due to the repetition rate. The available FTIR required repetition rates above 10 kHz. Instead a scanning monochrometer equipped with a liquid N_2 cooled MCT detector was used. Figure 25 shows the measured spectrum at the output of the OPA line. As expected, some narrowing of the seed bandwidth can be observed between the DFG and the amplified output. The spectrum measured at the output of the OPCPA was centred at 7 µm with a bandwidth of 1360 nm at $1/e^2$, which supports a transform limited pulse duration of 85 fs. This corresponds to a sub-four cycles pulse at the centre wavelength of 7 µm.

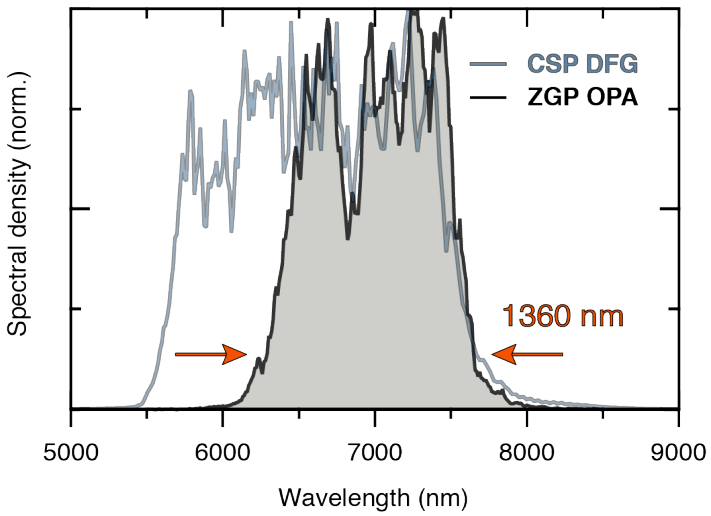

Figure 25: Amplified spectrum (black line, shaded) measured using a scanning monochromator and seed spectrum from the CSP DFG stage (gray line) measured with an FTIR. The spectral width of the OPCPA supports an 85 fs transform limited duration [35].

5.5 COMPRESSION AND CHARACTERISATION

A preliminary test for compressibility was undertaken using a standard folded positive-dispersion grating-based compressor scheme. A commercial ray tracing software (Optica for Mathematica) was used to design the compressor to compensate for -8.4·10^4 fs^2 and 9.6·10^5 fs^3 of second-order and third-order dispersion respectively introduced by the BaF_2 stretcher. The dispersion introduced by the ZGP crystals was considered to be negligible. The folded Martinez-style compressor consisted of a reflective Al-coated diffraction grating with a groove density 150 l/mm, an uncoated CaF_2 lens and gold coated mirrors. The incident angle on the grating was 65° from normal (Littrow is 32° at 7 μm). A small angle between the first and second pass and a pickoff mirror to separate input and output was used. The total energy throughput of the compressor was 35 %, yielding a compressed energy of 200 μJ. The main source of losses in this compressor was the diffraction gratings themselves, which was nearly 20 % per pass.

In order to take advantage of the full potential of the source to generate few-cycle pulses, diagnostic capabilities allowing retrieval of amplitude and phase at 7 μm in a reasonable time-frame are required. Unfortunately implementation of routine methods such as FROG are not straightforward in this spectral range. This is mostly due to the unavailability of mid-IR array detectors with sufficient spatial/spectral resolution for fast spectral acquisition. Other methods, such as electro-optical sampling would be ideally suited for direct and relatively fast waveform measurements in the mid-IR. In a recent work outside of the scope of this thesis, we showed the convenience of this method for complete spectral and temporal characterisation of a few-cycle laser source spanning the wavelength range from 6.8 μm to 16.4 μm [111]. The implementation of an electro-optical sampling scheme on the setup described in this thesis is left for future improvements on the system.

A background-free intensity autocorrelation was used as a first measurement of the temporal profile of the compressed pulses. The auto-correlator used ZGP as the nonlinear medium and all reflective

gold-coated optics to avoid introducing additional dispersion and losses in the compressed pulses. Figure 26 shows the measured trace, exhibiting an autocorrelation width of 360 fs. Sech^2, Gaussian and Lorentzian line shapes were fitted to the measured autocorrelation trace for its deconvolution. The autocorrelation traces were best fitted with a Lorentzian temporal profile. This unusual pulse shape was believed to be caused by residual absorption of small water content in the purged enclosure, which would give rise to modification of the sech^2 autocorrelation profile in favour of a Lorentzian shape. Under this assumption, the AC trace corresponds to a pulse duration of 180 fs, which is shorter than eight optical cycles. Pulse duration measurements performed during the writing of this thesis confirmed the pulse duration using third-harmonic FROG [36].

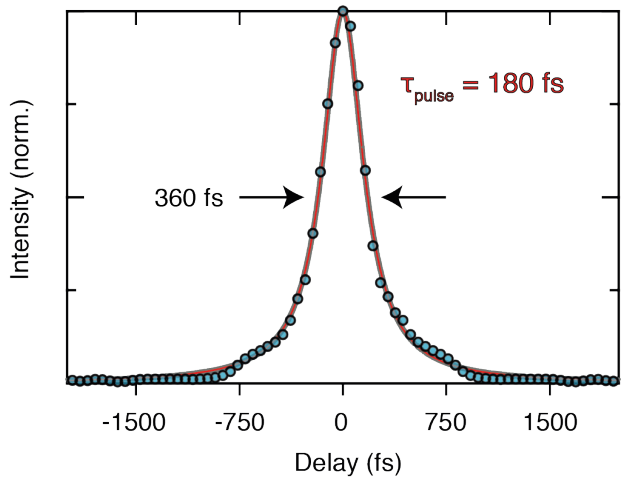

Figure 26: Autocorrelation trace from a background free intensity autocorrelation of the compressed pulses: measured trace (blue circle) and Lorentzian profile (solid red line). The deconvolution resulted in a pulse duration of 180 fs [35].

The semiconductor materials required to manufacture mid-IR detectors exhibit a bandgap small enough to be sensitive to thermal energy as well as mid-IR light. As en example, the photon energy at 7 µm is 170 meV, comparable to k_BT = 25 meV at room temperature. Consequently, the photodetectors need to be cooled to reduce

noise from thermally excited current carriers, typically to cryogenic temperatures. The most common semiconductor used for mid-IR applications is MCT. However even though MCT photodetectors can be obtained commercially, they are expensive and require active and constant cooling for operation. In particular MCT detector arrays, such as are required to build cameras, are so expensive and complex that their use is mostly restricted to military applications.

An alternative to MCT based devices for beam profiling are microbolometer cameras. These devices consist of a grid of absorptive elements with temperature dependent resistance. Their main drawback is an extremely low heat-induced damage threshold, which requires them to be used only with strongly attenuated beams. Using such a device the near and far field beam profile of the amplified output was measured (Fig. 27). The collimated beam was slightly oval, a small distortion which was expected due to the non-collinear interaction in the OPAs. Upon focusing the beam exhibited a symmetric profile. Finally, the stability of the compressed output was measured using a pyroelectric detector (Ophir Nova). A measurement of the output power over 30 min revealed a stability with fluctuations of less than 2.5% rms and no drift due to the passive stabilisation of the laser architecture (see Fig. 27).

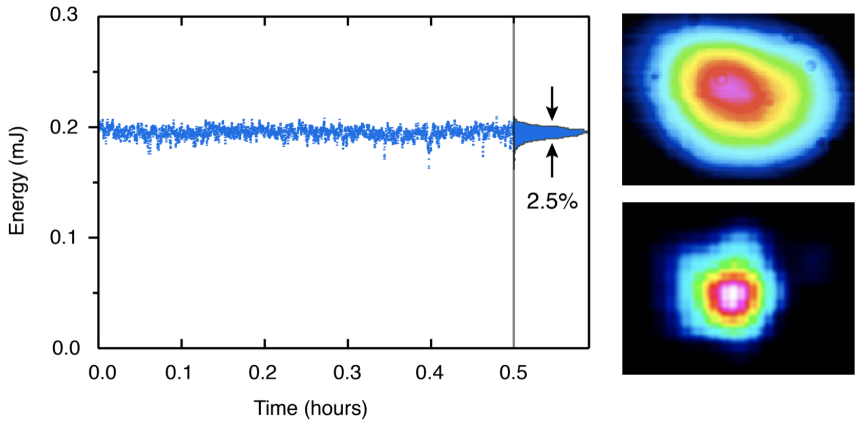

Figure 27: Stability and beam profile at the output of the OPCPA: (left) Power stability measured over 30 min, (top, right) collimated beam with a beam size if 1x0.85 mm^2 radius at FWHM and (bottom, right) beam focused with a 40 cm uncoated BaF_2 lens with a beam size of 70x70 μm^2 radius at FWHM.

6

SUMMARY AND OUTLOOK

The laser system described in this thesis represents an important step towards the realisation of a multi-mJ source of few-cycle duration, CEP-stable mid-IR pulses. The output parameters presented in this work are already suitable for strong-field experiments, enabling a ponderomotive force 77 times larger than an 800 nm wavelength source. Potential applications include driving source for HHG producing coherent X-rays in the multi-keV range and possibly sub-attosecond waveforms. A different approach to conventional laser design was necessary to develop this laser system. We chose an OPCPA architecture requiring the development of two novel sub-systems: a seed source of CEP-stable ultra-broadband pulses with a centre wavelength of 7 μm and a high energy picosecond pump source operating at 2 μm wavelength. The successful integration of these two sub-systems into a mid-IR OPCPA has proven the feasibility of this concept for generating high intensity pulses in the mid-IR, overcoming many of the drawbacks limiting other approaches. The main achievements of this thesis are summarised below.

Fibre-based source of ultra-broadband mid-IR pulses
We have developed a compact source of broadband mid-IR pulses relying on fibre-driven DFG in a CSP nonlinear crystal. The outstanding properties of CSP enabled us to generate spectra covering the 5.5 - 8 μm spectral range and carrying energies up to 150 pJ at 100 MHz, a several fold improvement from previously reported results. The bandwidth supported a transform-limited pulse duration of 50 fs, corresponding to less than 3 optical cycles at the centre wavelength. A fibre laser based on a mode-locked Er oscillator and Tm/Ho:fibre

amplifiers was specifically developed as driving source for the DFG stage. The use of a fibre laser guaranteed a compact and stable front-end, allowing turn-key operation of the laser system and requiring minimal maintenance. In addition, the use of a single, mode-locked oscillator to seed the DFG enabled the direct generation of CEP stable pulses, thus freeing the laser from active stabilisation schemes. At the time these experiments were undertaken, this was the broadest bandwidth generated using CSP and the first time this crystal was used in a critically phase-matched configuration. The suitability of this system as a seed source for a mid-IR OPCPA was shown in the last chapter of this thesis. The relatively high pulse energy as an OPA seeder made this source particularly well suited for a high gain amplifier line, as a high seed energy leads to increased stability and relaxes the gain requirements on the OPAs. While this laser source was envisioned as a seeder for a mid-IR OPCPA, the compact design, stability and broad bandwidth covering a spectral region of great interest for biology and medicine, also highlights the suitability of this source for spectroscopic applications.

260 mJ pump source for mid-IR OPCPA

We have developed a novel pump source for OPCPA, based on a Ho:YLF CPA pumped by commercial Tm-fibre laser. Ho:YLF was chosen as laser gain medium due to its high emission cross-section, long excited state lifetime allowing high energy extraction and CW pumping, weak thermal lens and natural birefringence. The system delivered 260 mJ energy pulses at a wavelength of 2052 nm at 100 Hz repetition rate. A grating-based compressor with a throughput of 85% yielded compressed pulses with a duration of 14 ps. To date, this is the highest energy 2 μm source of picosecond pulses. The laser system consisted of two Ho:YLF based amplifiers. The first was a regenerative amplifier seeded by the same fibre laser used to drive the DFG stage described in Chapter 3. A CVBG was used to stretch the 4 nJ energy seed pulses to 340 ps prior to amplification. The regenerative amplifier used a ring resonator geometry and delivered 4 mJ energy pulses using 9.2 W of CW pump power. The second amplifier relied on a multi-pass geometry using cryogenically cooled Ho:YLF. Cryogenic cooling was chosen as it improves the spectroscopic properties of Ho.YLF, effectively turning the crystal from a

quasi-three-level to four-level gain medium. Using 106.2 W of pump power, a 3-pass arrangement delivered pulse energies of 260 mJ. The stability, robustness and excellent beam quality of this laser system made it perfectly suited for pumping the mid-IR OPCPA described in Chapter 5. However, only a small fraction of the total pump energy could be used during the experimental work of this thesis due to constraints in the OPA crystals. The demonstration of this source represents a milestone in long-wavelength high energy pump lasers, a crucial component in the development of mid-IR OPCPA.

High intensity, mid-IR OPCPA
We have demonstrated, to the best of our knowledge, the first OPCPA operating at a centre wavelength of 7 μm. It was also the first demonstration of an OPCPA pumped directly at 2 μm. The use of long wavelength pump allowed us to resort to highly nonlinear non-oxide crystals that could not have been employed using a 1 μm pump source. The nonlinear crystal chosen for the OPAs was ZGP, a crystal which exhibits exceptional linear and nonlinear properties. The OPCPA was seeded with a single fibre laser. This approach guaranteed optical synchronisation between the seed and pump pulses in the amplifiers and therefore no active synchronisation was required. The OPA line, which consisted of three ZGP OPAs, delivered 0.55 mJ pulses - corresponding to an energy conversion efficiency of 18% from pump to signal and idler. A total pump energy of 12 mJ was used to achieve these result. After compression using a grating-based assembly, the system delivered pulses with an energy of 200 μJ with a temporal duration of 180 fs at 100 Hz repetition rate. The output parameters lead to a peak power of 1.1 GW and a peak intensity of $7{\cdot}10^{14}$ W/cm^2 if focused to the diffraction limit.

The OPCPA presented in this thesis is currently being upgraded and several notable improvements have been implemented while this thesis was being written [36]. The DFG stage has been modified to a collinear geometry to avoid the angular dispersion introduced in the non-collinear DFG. While this does lead to a loss of spectrum in the seed pulse, it still remains within the amplification bandwidth of the OPAs, and therefore has little effect on the final pulse duration. In order to circumvent the unavoidable losses in a long-wavelength

grating compressor, an intermediate grating stretcher has been added to change the sign of the chirp of the stretched pulses before the final OPAs. This allows compression using bulk dielectric media, with a measured efficiency of 93.5%. The current output of the laser system is 0.7 mJ pulses with a duration of 188 fs. Pulse diagnostics have been improved by changing the intensity autocorrelation used to retrieve the pulse duration in this work for third harmonic FROG. This allows unambiguous determination of the intensity profile of the output. Finally, the suitability of this source for strong-field experiments has been proven by driving HHG in bulk media. A thin polycrystalline sample of ZnSe has been pumped with peak intensities of 500 GW/cm^2, yielding a harmonic spectrum consisting of 13 harmonics, ranging from the mid-IR to the visible.

Further work mainly involves scaling of the output energy which should, in principle, be straightforward. The pump energy used for the results shown in this thesis constitute less than 5% of the current available energy. The limiting factor at the time the experiments were performed was the aperture of the ZGP crystals used in the OPAs. The ZGP samples we had available allowed using only 8 mJ of pump energy in the last OPA stage. Advances in the fabrication of large-aperture ZGP that happened in parallel to this work, have allowed the acquisition of ZGP crystals with a clear aperture bigger than 2.5 x 2 cm^2, allowing the use of up to 100 mJ of pulse energy per OPA. A conservative estimate is that pulse energies at 7 μm between 5 mJ and 10 mJ are feasible in the near future. Finally, the implementation of electro-optic sampling into the setup would allow improved diagnostics of the mid-IR pulses by directly measuring the electric field of the pulses and drifts in the CEP. The main challenge is the short probe pulse required for this technique, which needs to have a pulse duration comparable to a cycle of the electric field. This is the main obstacle limiting the extension of electro-optical sampling as a pulse measurement technique to the near-IR. For this laser system, with a centre wavelength of 7 μm, a probe pulse with a duration shorter than 20 fs would be required. This can be realised experimentally using highly-nonlinear fibres for additional compression of the 1.55 μm output of the fibre laser.

BIBLIOGRAPHY

[1] A. L. Schawlow, C. H. Townes, "Infrared and Optical Masers," Phys. Rev. **112**, 1940 (1958).

[2] T. H. Maiman, "Stimulated optical radiation in ruby," Nature **187**, 493 (1960).

[3] T. H. Maiman, "Optical and microwave-optical experiments in Ruby," Phys. Rev. Lett. **4**, 564 (1960).

[4] P. A. Franken, A. E. Hill, C. W. Peters, G. Weinreich, "Generation of Optical Harmonics," Phys. Rev. Lett. **7**, 118 (1961).

[5] A. McPherson, G. Gibson, H. Jara, U. Johann, T. S. Luk, I. A. McIntyre, K. Boyer, C. K. Rhodes, "Studies of multiphoton production of vacuum-ultraviolet radiation in the rare gases," J. Opt. Soc. Am. B **4**, 595 (1987).

[6] P. Agostini, F. Fabre, G. Mainfray, G. Petite, N. K. Rahman, "Free-Free Transitions Following Six-Photon Ionization of Xenon Atoms," Phys. Rev. Lett. **42**, 1127 (1979).

[7] T. Zuo, A. D. Bandrauk, P. B. Corkum, "Laser-induced electron diffraction: a new tool for probing ultrafast molecular dynamics," Chem. Phys. Lett. **259**, 313 (1996).

[8] M. Hentschel, R. Kienberger, C. Spielmann, G. A. Reider, N. Milosevic, T. Brabec, F. Krausz, "Attosecond metrology," Nature **414**, 509 (2001).

[9] B. Wolter, M. G. Pullen, M. Baudisch, M. Sclafani, M. Hemmer, A. Senftleben, C. D. Schroter, J. Ullrich, R. Moshammer, J. Biegert, "Strong-field physics with mid-IR fields," Phys. Rev. X **5**, 021034 (2015).

[10] P. Corkum, "Plasma Perspective on Strong-Field Multiphoton Ionization," Phys. Rev. Lett. **71**, 1994 (1993).

[11] Ariel Gordon, Franz X. Kartner, "Scaling of keV HHG photon yield with drive wavelength," Opt. Express **13**, 2941 (2005).

[12] J. Tate, T. Auguste, H.G. Muller, P. Salières, P. Agostini, L.F DiMauro, "Scaling of Wave-Packet Dynamics in an Intense Midinfrared Field," Phys. Rev. Lett. **98**(1), 013901 (2007).

[13] V. Yakovlev, M. Ivanov, F. Krausz, "Enhanced phase-matching for generation of soft X-ray harmonics and attosecond pulses in atomic gases," Opt. Express **15**, 15351 (2007).

[14] T. Popmintchev, M. C. Chen, P. Arpin, M. Murnane, H. Kapteyn, "The attosecond nonlinear optics of bright coherent X-ray generation," Nat. Photonics **4**, 822 (2010).

[15] T. Popmintchev, M. C. Chen, D. Popmintchev, P. Arpin, S. Brown, S. Alisauskas, G. Andriukaitis, T. Balciunas, O. D. Mücke, A. Pugzlys, A. Baltuska, B. Shim, S. E. Schrauth, A. Gaeta, C. Hernández-García, L. Plaja, A. Becker, A. Jaron-Becker, M. M. Murnane, H. C. Kapteyn, "Bright Coherent Ultrahigh Harmonics in the keV X-ray Regime from Mid-Infrared Femtosecond Lasers," Science **336**, 1287 (2012).

[16] C. Hernández-García, J. A. Pérez-Hernández, T. Popmintchev, M. M. Murnane, H. C. Kapteyn, A. Jaron-Becker, A. Becker, L. Plaja, "Zeptosecond High Harmonic keV X-Ray waveforms driven by midinfrared laser pulses," Phys. Rev. Lett. **111**, 033002 (2013).

[17] A. Emelina, M. Emelin, M. Ryabikin "On the possibility of the generation of high harmonics with photon energies greater than 10 keV upon interaction of intense mid-IR radiation with neutral gases," Quantum Electron. **44**, 470 (2014).

[18] P. Whalen, P. Panagiotopoulos, M. Kolesik, J. V. Moloney, "Extreme carrier shocking of intense long-wavelength pulses," Phys. Rev. A **89**, 023850 (2014).

[19] T. Auguste, P. Salières, A. S. Wyatt, A. Monmayrant, I. A. Walmsley, E. Cormier, A. Zaïr, M. Holler, A. Guandalini, F. Schapper, J. Biegert, L. Gallmann, U. Keller, "Theoretical and experimental analysis of quantum path interferences in high-order harmonic generation," Phys. Rev. A **80**, 033817 (2009).

[20] H. R. Reiss, "Limits on Tunneling Theories of Strong-Field Ionization," Phys. Rev. Lett. **101**, 043002 (2008).

[21] I. Jovanovic, G. Xy, S. Wandel, "Mid-Infrared Laser System Development for Dielectric Laser Accelerators," Phys. Proc. **52**, 68 (2014).

[22] S. L. Cousin, F. Silva, S. Teichmann, M. Hemmer, B. Buades, J. Biegert, "High-flux table-top soft x-ray source driven by sub-2-cycle, CEP stable, 1.85-um 1-kHz pulses for carbon K-edge spectroscopy," Opt. Lett. **39**, 5383 (2014).

[23] F. Silva, S. M. Teichmann, S. L. Cousin, M. Hemmer, J. Biegert, "Spatiotemporal isolation of attosecond soft X-ray pulses in the water window," Nature Commun. **6**, 6611 (2015).

[24] S. M. Teichmann, F. Silva, S. L. Cousin, M. Hemmer, J. Biegert, "0.5-keV Soft X-ray attosecond continua," Nature Commun. **7**, 11493 (2016).

[25] S. L. Cousin, N. Di Palo, B. Buades, S. M. Teichmann, M. Reduzzi, M. Devetta, A. Kheifets, G. Sansone, J. Biegert, "Attosecond streaking in the water window: A new regime of attosecond pulse characterization," Phys. Rev. X **7**, 041030 (2017).

[26] M. G. Pullen, B. Wolter, A. T. Le, M. Baudisch, M. Hemmer, A. Senftleben, C. D. Schröter, J. Ullrich, R. Moshammer, C. D. Lin, J. Biegert, "Imaging an aligned polyatomic molecule with laser-induced electron diffraction," Nature Commun. **6**, 7262 (2015).

[27] B. Wolter, M. G. Pullen, A.-T. Le, M. Baudisch, K. Doblhoff-Dier, A. Senftleben, M. Hemmer, C. D. Schröter, J. Ullrich, T. Pfeifer, R. Moshammer, S. Gräfe, O. Vendrell, C. D. Lin, J. Biegert, "Ultrafast electron diffraction imaging of bond breaking in di-ionized acetylene," Science **354**, 308 (2016).

[28] K. Amini, M. Sclafani, T. Steinle, A. Le, A. Sanchez, C. Müller, J. Steinmetzer, L. Yue, J. R. Martínez Saavedra, M. Hemmer, Maciej Lewenstein, Robert Moshammer, Thomas Pfeifer, M. G. Pullen, J. Ullrich, B. Wolter, R. Moszynski, F. J. García de Abajo, C. D. Lin, S. Gräfe, J. Biegert, "Imaging the Renner-Teller effect using laser-induced electron diffraction," PNAS **116** (17), 8173 (2019).

[29] O. Chalus, P. Bates, M. Smolarski, J. Biegert, "Mid-IR short-pulse OPCPA with micro-Joule energy at 100kHz," Opt. Express **17**, 3587 (2009).

[30] C. Erny, C. Heese, M. Haag, L. Gallmann, U. Keller, "High-repetition-rate optical parametric chirped-pulse amplifier producing 1-μJ, sub-100-fs pulses in the mid-infrared," Opt. Express **17**, 1340-1345 (2009).

[31] G. Andriukaitis, T. Balciunas, S. Ališauskas, A. Pugžlys, A. Baltuška, T. Popmintchev, MC. Chen, M. Murnane, H. Kapteyn, "90 GW peak power few-cycle mid-infrared pulses from an optical parametric amplifier," Opt. Lett. **36**, 2755 (2011).

[32] N. Thiré, R. Maksimenka, B. Kiss, C. Ferchaud, P. Bizouard, E. Cormier, K. Osvay, N. Forget, "4-W, 100-kHz, few-cycle mid-infrared source with sub-100-mrad carrier-envelope phase noise," Opt. Express **25**, 1505 (2017)

[33] M. Baudisch, B. Wolter, M. Pullen, M. Hemmer, J. Biegert, "High power multicolor OPCPA source with simultaneous femtosecond deep-UV to mid-IR outputs," Opt. Lett. **41**, 3583-3586 (2016)

[34] U. Elu, M. Baudisch, H. Pires, F. Tani, M. Frosz, F. Köttig, A. Ermolov, P. Russell, Jens Biegert, "High average power and single-cycle pulses from a mid-IR optical parametric chirped pulse amplifier," Optica **4**, 1024 (2017).

[35] D. Sanchez, M. Hemmer, M. Baudisch, S. L. Cousin, K. Zawilski, P. Schunemann, O. Chalus, C. Simon-Boisson, J. Biegert, "7 μm, ultrafast, sub-millijoule-level mid-infrared optical parametric chirped pulse amplifier pumped at 2 μm," Optica **3**, 147 (2016).

[36] U. Elu, T. Steinle, D. Sánchez, L. Maidment, K. Zawilski, P. Schunemann, U. D. Zeitner, C. Simon-Boisson, J. Biegert, "Table-top high-energy 7 μm OPCPA and 260 mJ Ho:YLF pump laser," Manuscript submitted for publication (2019).

[37] T. Kanai, P. Malevich, S. Kangaparambil, K. Ishida, M. Mizui, K. Yamanouchi, H. Hoogland, R. Holzwarth, A. Pugzlys, A. Baltuska, "Parametric amplification of 100 fs mid-infrared pulses in $ZnGeP_2$ driven by a Ho:YAG chirped-pulse amplifier," Opt. Lett. **42**, 683 (2017).

[38] M. Bock, L. Grafenstein, U. Griebner, T. Elsaesser, "Generation of millijoule few-cycle pulses at 5 μm by indirect spectral shaping of the idler in an optical parametric chirped pulse amplifier," J. Opt. Soc. Am. B **35**, C18-C24 (2018).

[39] Armstrong J.A. Armstrong, N. Bloembergen, J. Ducuing, P.S. Pershan, "Interactions between Light Waves in a Nonlinear Dielectric," Phys. Rev. **127**,1918 (1962).

[40] J-C Diels, W. Rudolph, "Ultrashort Laser Pulse Phenomena," 2nd ed., Academic Press, (2006).

[41] R.W. Boyd, "Nonlinear Optics," 3rd ed., Academic Press, Orlando, (2008).

[42] R. Baumgartner, R. Byer, "Optical parametric amplification," IEEE JQE **15** (6), 432 (1979).

[43] I. N. Ross, P. Matousek, G. H. C. New, K. Osvay, "Analysis and optimization of optical parametric chirped pulse amplification," J. Opt. Soc. Am. B **19**, 2945-2957 (2002)

[44] Manley J. M and Rowe, H. E., "Some General Properties of Nonlinear Elements Part I: General Energy Relations", Proceedings of the IRE, 904 (1956).

[45] A. Shirakawa, I. Sakane, M. Takasaka, T. Kobayashi, "Sub-5-fs visible pulse generation by pulse-front-matched noncollinear optical parametric amplification", Appl. Phys. Lett. **74** (16), 2268 (1999).

[46] D. N. Schimpf, J. Rothhardt, J. Limpert, A. Tünnermann, D. C. Hanna, "Theoretical analysis of the gain bandwidth for noncollinear parametric amplification of ultrafast pulse," J. Opt. Soc. Am. B **24** (11), 2837 (2007).

[47] I. P. Christov, M. M. Murnane, H. C. Kapteyn, "High-Harmonic Generation of Attosecond Pulses in the Single-Cycle Regime," Phys. Rev. Lett. **78**, 1251 (1997).

[48] T. Brabec, F. Krausz, "Intense few-cycle laser fields: Frontiers of nonlinear optics", Rev. Mod. Phys. **72**, 545 (2000).

[49] T. Udem, J. Reichert, R. Holzwarth, T.W. Hänsch, "Accurate measurement of large optical frequency differences with a mode-locked laser," Opt. Lett. **24**, 881(1999).

[50] J. Reichert, R. Holzwarth, T. Udem, T Hänsch, "Measuring the frequency of light with mode-locked lasers," Opt. Commun. **172**, 59 (1999).

[51] M. Kakehata, H. Takada, Y. Kobayashi, K. Torizuka, Y. Fujihira, T. Homma, H. Takahashi, "Single-shot measurement of carrier-envelope phase changes by spectral interferometry," Opt. Lett. **26**, 1436 (2001).

[52] C. A. Haworth, L. E. Chipperfield, J. S. Robinson, P. L. Knight, J. P. Marangos, J. W. G. Tisch, "Half-cycle cutoffs in harmonic spectra and robust carrier-envelope phase retrieval," Nature Phys. **3**, 52 (2007).

[53] L. Xu, Ch. Spielmann, A. Poppe, T. Brabec, F. Krausz, T. W. Hänsch, "Route to phase control of ultrashort light pulses," Opt. Lett. **21**, 2008 (1996).

[54] D. J. Jones, S. Diddams, J. Ranka, A. Stentz, R. Windeler, J. Hall, S. Cundiff, "Carrier-Envelope Phase Control of Femtosecond Mode-Locked Lasers and Direct Optical Frequency Synthesis," Science **288**(5466), 635 (2000).

[55] T. Fuji, A. Apolonski, F. Krausz, "Self-stabilization of carrier-envelope offset phase by use of difference-frequency generation," Opt. Lett. **29**, 632 (2004).

[56] P. R. Griffiths, J. A. d. Haseth, "Fourier Transform Infrared Spectroscopy," 2nd ed., Wiley-Interscience, (2007).

[57] F. K. Tittel, D. Richter, A. Fried, "Mid-Infrared laser applications in spectroscopy," Top. Appl. Phys. **89**, 458 (2003).

[58] W. Petrich, "Mid-Infrared and Raman spectroscopy for medical diagnostics," Appl. Spectrosc. Rev. **36**, 181 (2001).

[59] C. Petibois, G. M. Deleris, "Chemical mapping of tumor progression by FT-IR imaging: towards molecular histopathology," Trends Biotechnol. **24**, 455 (2006).

[60] P. Colarusso, L.H. Kidder, I.W. Levin, J.C.Fraser, J.F. Arens, E.N. Lewis, "Infrared Spectroscopic Imaging: From Planetary to Cellular Systems," Appl. Spectrosc. **52**, 106A (1998).

[61] R. Bhargava, "Infrared spectroscopic imaging: the next generation," Appl. Spectrosc. **66**, 1091 (2012).

[62] E.N. Lewis, P.J. Treado, R.C. Reeder, G.M. Story, A.E. Dowrey, C. Marcott, I.W. Levin, "Fourier-transform spectroscopic imaging using an infrared focal-plane array detector," Anal. Chem. **67**, 3377 (1995).

[63] W. D. Duncan, G. P. Williams, "Infrared synchrotron radiation from electron storage rings," Appl. Opt. **22**, 2914 (1983).

[64] L. M. Miller, P. Dumas, "Chemical imaging of biological tissue with synchrotron infrared light," Biochimica et Biophysica Acta (BBA) **1758**(7), 846 (2006).

[65] C. Petibois, G. Deleris, M. Piccinini, M. Cestelli-Guidi, A. Marcelli, "A bright future for synchrotron imaging," Nat. Photonics **3**, 179 (2009).

[66] Y. Yu, X. Gai, P. Ma, D.-Y. Choi, Z. Yang, R. Wang, S. Debbarma, S. J. Madden, B. Luther-Davies, "A broadband, quasi-continuous, mid-infrared supercontinuum generated in a chalcogenide glass waveguide," Laser Photon. Rev. **8**, 792 (2014).

[67] T. Steinle, F. Neubrech, A. Steinmann, X. Yin, H. Giessen, "Mid-infrared Fourier-transform spectroscopy with a high-brilliance tunable laser source: investigating sample areas down to 5 μm diameter," Opt. Express **23**, 11105 (2015).

[68] H. Hoogland, A. Thai, D. Sanchez, S. L. Cousin, M. Hemmer, M. Engelbrecht, J. Biegert, R. Holzwarth, "All-PM coherent 2.05 um Thulium/Holmium fiber frequency comb source at 100 MHz with up to 0.5 W average power and pulse duration down to 135 fs," Opt. Express **21**, 31390 (2013).

[69] D. Sánchez, M. Hemmer, M. Baudisch, K. Zawilski, P. Schunemann, H. Hoogland, R. Holzwarth, J. Biegert, "Broadband mid-IR frequency comb with $CdSiP_2$ and $AgGaS_2$ from an Er,Tm:Ho fiber laser," Opt. Lett. **39**, 6883 (2014).

[70] L.D. DeLoach, R.H. Page, G.D. Wilke, S.A. Payne, W.P. Krupke, "Transition metal-doped zinc chalcogenides: spectroscopy and laser demonstration of a new class of gain media," IEEE JQE **32**, 885 (1996).

[71] J. J. Adams, C. Bibeau, R. H. Page, D. M. Krol, L. H. Furu, S. A. Payne, "4.0-4.5 μm lasing of Fe:ZnSe below 180 K, a new mid-infrared laser material," Opt. Lett. **24**, 1720 (1999).

[72] I. T. Sorokina, E. Sorokin, T. Carrig, "Femtosecond pulse generation from a SESAM mode-locked Cr:ZnSe Laser," CLEO/QELS, Technical Digest on CD, (OSA, 2006) paper CMQ2.

[73] Sorokin, E., Sorokina, I. T., Mandon, J., Guelachvili, G. Picqué, N., "Sensitive multiplex spectroscopy in the molecular fingerprint 2.4 μm region with a Cr2+:ZnSe femtosecond laser," Opt. Express **15**, 16540 (2007).

[74] M. Cizmeciyan, H. Cankaya, A. Kurt, A. Sennaroglu, "Kerr-lens mode-locked femtosecond Cr^2:ZnSe laser at 2420 nm," Opt. Lett. **34**, 3056 (2009).

[75] Nikolai Tolstik, Evgeni Sorokin, and Irina T. Sorokina, "Graphene mode-locked Cr:ZnS laser with 41 fs pulse duration," Opt. Express **22**, 5564 (2014).

[76] I. Sorokina, E. Sorokin, "Femtosecond Cr^2 based lasers," IEEE J. Sel. Top. Quantum Electron. **21**, 273 (2015).

[77] J. Kernal, V. V. Fedorov, A. Gallian, S. B. Mirov, V. V. Badikov, "3.9-4.8 μm gain-switched lasing of Fe:ZnSe at room temperature," Opt. Express **13**, 10608 (2005).

[78] V.V. Fedorov, S.B. Mirov, A. Gallian, D.V. Badikov, M.P. Frolov, Y.V. Korostelin, V.I. Kozlovsky, A.I. Landman, Y.P. Podmarkov, V.A. Akimov, A.A. Voronov, "3.77 - 5.05 μm tunable solid-state lasers based on Fe^2 doped ZnSe crystals operating at low and room temperatures," IEEE J. Quant. Electron. **42**, 907 (2006).

[79] A.W. Smith, N. Braslau, "Observation of an Optical Difference Frequency," J. Appl. Phys. **34**(7), 2105 (1963).

[80] J. A. Giordmaine, R. C. Miller, "Tunable coherent parametric oscillation in $LiNbO_3$ at optical frequencies," Phys. Rev. Lett. **14** (24), 973 (1965).

[81] M. Ebrahim-Zadeh, "Mid-infrared ultrafast and continuous wave optical parametric oscillators," Solid-State Mid-Infrared Laser Sources, Springer-Verlag Science Series, Topics Appl. Phys. **89**, 184 (2003).

[82] S. Chaitanya Kumar, A. Esteban-Martin, T. Ideguchi, M. Yan, S. Holzner, T.W. Hänsch, N. Picqué, M. Ebrahim- Zadeh, "Few-cycle, broadband, mid-infrared optical parametric oscillator pumped by a 20-fs Ti:sapphire laser," Laser Photon. Rev. **8**(5), L86 (2014).

[83] S. M. Foreman, D. J. Jones, J. Ye, "Flexible and rapidly configurable femtosecond pulse generation in the mid-IR," Opt. Lett. **28**, 370 (2003).

[84] C. Erny, K. Moutzouris, J. Biegert, D. Kühlke, F. Adler, A. Leitenstorfer, U. Keller, "Mid-infrared difference-frequency generation of ultrashort pulses tunable between 3.2 and 4.8 μm from a compact fiber source," Opt. Lett. **32**, 1138 (2007).

[85] A. Ruehl, A. Gambetta, I. Hartl, M. E. Fermann, K. S. E. Eikema, M. Marangoni, "Widely-tunable mid-infrared frequency comb source based on difference frequency generation," Opt. Lett. **37**, 2232 (2012).

[86] V. Petrov, "Parametric down-conversion devices: The coverage of the mid-infrared spectral range by solid-state laser sources," Opt. Mater. **34**, 536 (2012).

[87] P. G. Schunemann, "New Nonlinear Optical Crystals for the Mid-Infrared," in Advanced Solid State Lasers, OSA Technical Digest (OSA, 2015), paper AM2A.2.

[88] D. N. Nikogosyan, "Nonlinear Optical Crystals: A Complete Survey," Springer-Verlag New York, (2005).

[89] A. V. Smith, "SNLO software for simulating nonlinear frequency conversion in crystals," free download, http://www.as-photonics.com/snlo, from AS-Photonics.

[90] P. Kupecek, C. Schwartz, D. Chemla, "Silver thiogallate ($AgGaS_2$) - Part 1: Nonlinear optical properties," IEEE J. Quantum Electron. **10**(7), 540 (1974).

[91] E. Takaoka, K. Kato, "Thermo-optic dispersion formula for $AgGaS_2$," Appl. Opt. **38**, 4577 (1999).

[92] D. Roberts, "Dispersion equations for nonlinear optical crystals: KDP, $AgGaSe_2$, and $AgGaS_2$," Appl. Opt. **35**, 4677 (1996).

[93] K. Kato, "High-power difference-frequency generation at 5-11 μm in $AgGaS_2$," IEEE J. Quantum Electron. **20**(7), 698 (1984).

[94] N. P. Barnes, D. J. Gettemy, J. R. Hietanen, R. A. Iannini, "Parametric amplification in $AgGaSe_2$," Appl. Opt. **28**, 5162 (1989).

[95] G. B. Abdullaev, L. A. Kulevskii, A. M. Prokhorov, A. D. Savelev, E. Yu. Salaev, V. V. Smirnov, "GaSe, a new effective crystal for nonlinear optics," JETP Lett. **16**, 90 (1972).

[96] K. L. Vodopyanov, "Parametric generation of tunable infrared radiation in $ZnGeP_2$ and GaSe pumped at 3 μm," J. Opt. Soc. Am. B **10**, 1723 (1993).

[97] R. Huber, A. Brodschelm, F. Tauser, A. Leitenstorfer, "Generation and field-resolved detection of femtosecond electromagnetic pulses tunable up to 41 THz," Appl. Phys. Lett., **76**(22), 3191 (2000).

[98] G. D. Boyd, E. Buehler, F. G. Storz, "Linear and nonlinear properties of $ZnGeP_2$ and CdSe," Appl. Phys. Lett. **18**(7), 301 (1971)

[99] P.D. Mason, D.J. Jackson, E.K. Gorton, "CO_2 laser frequency doubling in $ZnGeP_2$," Opt. Commun. **110**, 163 (1994).

[100] V. Petrov, F. Rotermund, F. Noack, P. Schunemann, "Femtosecond parametric generation in $ZnGeP_2$," Opt. Lett. **2**(4), 414 (1999).

[101] K. L. Vodopyanov, F. Ganikhanov, J. P. Maffetone, I. Zwieback, W. Ruderman, "$ZnGeP_2$ optical parametric oscillator with 3.8-12.4 μm tunability," Opt. Lett. **25**, 841 (2000).

[102] K. T. Zawilski, P. G. Schunemann, S. D. Setzler, T. M. Pollak, "Large aperture single crystal $ZnGeP_2$ for high-energy applications," J. Cryst. Growth, **310**(7-9), 1891 (2008).

[103] N. Itoh, T. Fujinaga, T. Nakau, "Birefringence in $CdSiP_2$," Jap. J. Appl. Phys. **17**, 951 (1978) .

[104] P. G. Schunemann, K. T. Zawilski, T. M. Pollak, V. Petrov, D. E. Zelmon, "$CdSiP_2$: a new nonlinear optical crystal for 1 and 1.5 micron-pumped mid-IR generation," in Advanced Solid-State Photonics, OSA Technical Digest Series (CD) (OSA, 2009), paper TuC6.

[105] K. T. Zawilski, P. G. Schunemann, T. C. Pollak, D. E. Zelmon, N. C. Fernelius, F. Kenneth Hopkins, "Growth and characterization of large $CdSiP_2$ single crystals," J. Cryst. Growth, **312**(8), 1127 (2010).

[106] O. Chalus, P. G. Schunemann, K. T. Zawilski, J. Biegert, and M. Ebrahim-Zadeh, "Optical parametric generation in $CdSiP_2$," Opt. Lett. **3**, 4142 (2010).

[107] Z. Zhang, D. T. Reid, S. C. Kumar, M. Ebrahim-Zadeh, P. Schunemann, K. Zawilski, C. R. Howle, "Femtosecond-laser pumped $CdSiP_2$ optical parametric oscillator producing 100 MHz pulses centered at 6.2 μm," Opt. Lett. **38**, 5110 (2013).

[108] F. Rotermund, V. Petrov, F. Noack, L. Isaenko, A. Yelisseyev, S. Lobanov, "Optical parametric generation of femtosecond pulses up to 9 μm with $LiInS_2$ pumped at 800 nm," Appl. Phys. Lett. **78**(18), 2623 (2001).

[109] V. Petrov, A. Yelisseyev, L. Isaenko, S. Lobanov, A. Titov, J. J. Zondy, "Second harmonic generation and optical parametric amplification in the mid-IR with orthorhombic biaxial crystals $LiGaS_2$ and $LiGaSe_2$," Appl. Phys. B **78**(5), 543 (2004).

[110] M. Beutler, I. Rimke, E. Buttner, V. Petrov, L. Isaenko, "Femtosecond mid-IR difference-frequency generation in $LiInSe_2$," Opt. Mater. Express **3**, 1834 (2013).

[111] I. Pupeza, D. Sánchez, J. Zhang, N. Lilienfein, M. Seidel, N. Karpowicz, T. Paasch-Colberg, I. Znakovskaya, M. Pescher, W. Schweinberger, V. Pervak, E. Fill, O. Pronin, Z. Wei, F. Krausz, A. Apolonski, J. Biegert, "High-power sub-two-cycle mid-infrared pulses at 100 MHz repetition rate," Nat. Photonics **9**, 721 (2015).

[112] P. Schunemann, K. Zawiliski, L. Pomeranz, D. Creeden, P. Budni, "Advances in nonlinear optical crystals for mid-infrared coherent sources," JOSA B **33**, D36 (2016).

[113] L.E. Myers, G.D. Miller, R.C. Eckardt, M.M. Fejer, R.L. Byer, "Quasi-phase-matched 1.064-mm-pumped optical parametric oscillator in bulk periodically poled $LiNbO_3$," Opt. Letters **20**, 52 (1995).

[114] M. Ebrahim-Zadeh, S. Chaitanya Kumar, and K. Devi, "Yb-Fiber-Laser-Pumped Continuous-Wave Frequency Conversion Sources from the Mid-Infrared to the Ultraviolet," IEEE J. Sel. Top. Quantum Electron. **20**, 0902823 (2014).

[115] R. Bhatt, I. Bhaumik, S. Ganesamoorthy, R. Bright, M. Soharab, A. K. Karnal, P. K. Gupta, "Control of intrinsic defects in lithium niobate single crystals for optoelectronic applications," Crystals **7**(2), 23 (2017).

[116] C. B. Ebert, L. A. Eyres, M. M. Fejer, and J. S. Harris, "MBE growth of antiphase GaAs films using GaAs/Ge/GaAs heteroepitaxy," J. Cryst. Growth **201**, 187 (1999).

[117] O. Levi, T. J. Pinguet, T. Skauli, L. A. Eyres, K. R. Parameswaran, J. S. Harris, M. M. Fejer, T. J. Kulp, S. E. Bisson, B. Gerard, E. Lallier, L. Becouarn, "Difference frequency generation of 8-μm radiation in orientation-patterned GaAs," Opt. Lett. **27**, 2091 (2002)

[118] K. L. Vodopyanov, E. Sorokin, I. T. Sorokina, P. G. Schunemann, "Mid-IR frequency comb source spanning 4.4-5.4 μm based on subharmonic GaAs optical parametric oscillator," Opt. Lett. **36**, 2275 (2011).

[119] T. Matsushita, T. Yamamoto, T. Kondo, "Epitaxial growth of spatially inverted GaP for quasi phase matched nonlinear optical devices," Jpn. J. Appl. Phys. **46**, L408 (2007).

[120] E. Sorokin, A Marandi, P. Schunemann, M. M. Fejer, R. Byer, I. Sorokina, "Efficient half-harmonic generation of three-optical-cycle mid-IR frequency comb around 4 μm using OP-GaP," Opt. Express **26**, 9963 (2018).

[121] K. Devi, A. Padhye, P. G. Schunemann, M. Ebrahim-Zadeh, "Multimilliwatt, tunable, continuous-wave, mid-infrared generation across 4.6-4.7," μm based on orientation-patterned gallium phosphide," Opt. Lett. **43**, 2284 (2018)

[122] G. Arisholm, "General numerical methods for simulating second-order nonlinear interactions in birefringent media," J. Opt. Soc. Am. B **14**, 2543 (1997).

[123] A. Thai, C. Skrobol, P. K. Bates, G. Arisholm, Z. Major, F. Krausz, S. Karsch, and J. Biegert, "Simulations of petawatt-class few-cycle optical-parametric chirped-pulse amplification, including nonlinear refractive index effects," Opt. Lett. **35**, 3471 (2010).

[124] V. Kemlin, P. Brand, B. Boulanger, P. Segonds, P. G. Schunemann, K. T. Zawilski, B. Ménaert, J. Debray, "Phase-matching properties and refined Sellmeier equations of the new nonlinear infrared crystal CdSiP2," Opt. Lett. **36**, 1800 (2011).

[125] V. Petrov, F. Noack, I. Tunchev, P. Schunemann, K. Zawilski, "The nonlinear coefficient d_{36} of $CdSiP_2$," Proc. SPIE 7197, 71970M (2009).

[126] A.Shirakawa, I.Sakane, T.Kobayashi, "Pulse-front-matched optical parametric amplification for sub-10-fs pulse generation tuneable in the visible and near infrared," Opt. Lett. **23**, 1292 (1998).

[127] Z. Heiner, V. Petrov, G. Steinmeyer, M. J. J. Vrakking, M. Mero, "100-kHz, dual-beam OPA delivering high-quality, 5-cycle angular-dispersion-compensated mid-infrared idler pulses at 3.1 μm," Opt. Express **26**, 25793 (2018).

[128] Rothman LS, Gordon IE, Barbe A, Benner DC, Bernath PF, Birk M, *et al.*, "The HITRAN 2008 molecular spectroscopic database," J Quant. Spectrosc. Radiat. Transfer. **110**, 533 (2009).

[129] A. Dubietis, G. Jonusauskas, A. Piskarskas, "Powerful femtosecond pulse generation by chirped and stretched pulse parametric amplification in BBO crystal," Opt. Commun. **88**, 437 (1992).

[130] A. Vaupel, N. Bodnar, B. Webb, L. Shah, M. C. Richardson, "Concepts, performance review, and prospects of table-top, few-cycle optical parametric chirped-pulse amplification," Opt. Eng. **53**(5), 051507 (2013).

[131] J. Rothhardt, S. Demmler, S. Hädrich, J. Limpert, A. Tünnermann, "Octave-spanning OPCPA system delivering CEP-stable few-cycle pulses and 22 W of average power at 1 MHz repetition rate," Opt. Express **20**, 10870-10878 (2012).

[132] M. Krebs, S. Hädrich, S. Demmler, J. Rothhardt, A. Zaïr, L. Chipperfield, J. Limpert, A. Tünnermann, "Towards isolated attosecond pulses at megahertz repetition rates," Nat. Photonics **7**, 555 (2013).

[133] F. Tavella, A. Marcinkeviius, F. Krausz, "90 mJ parametric chirped pulse amplification of 10 fs pulses," Opt. Express **14**(26), 12822 (2006).

[134] D. Herrmann, L. Veisz, R. Tautz, F. Tavella, K. Schmid, V. Pervak, F. Krausz, "Generation of sub-three-cycle, 16 TW light pulses by using noncollinear optical parametric chirped-pulse amplification," Opt. Lett. **34**, 2459 (2009).

[135] S. Prinz, M. Schnitzenbaumer, D. Potamianos, M. Schultze, S. Stark, M. Häfner, C. Y. Teisset, C. Wandt, K. Michel, R. Kienberger, B. Bernhardt, T. Metzger, "Thin-disk pumped optical parametric chirped pulse amplifier delivering CEP-stable multi-mJ few-cycle pulses at 6 kHz," Opt. Express **26**, 1108 (2018).

[136] L. E. Zapata, F. Reichert, M. Hemmer, F. X. Kärtner, "250 W average power, 100 kHz repetition rate cryogenic Yb:YAG amplifier for OPCPA pumping," Opt. Lett. **41**, 492 (2016).

[137] L. F Johnson, "Optical Maser Characteristics of Rare-Earth Ions in Crystals. J. Appl. Phys **34**(4), 897 (1963).

[138] L. F. Johnson, J. E. Geusic, L. G. Van Uitert, "Efficient, high-power coherent emission from Ho^{3+} ions in Yttrium Aluminum Garnet, assisted by energy transfer," Appl. Phys. Lett. **8**, 200 (1966).

[139] S. A. Payne, L. L. Chase, L. K. Smith, W. L. Kway, W. F. Krupke, "Infrared cross-section measurements for crystals doped with Er^{3+}, Tm^{3+}, and Ho^{3+}," IEEE J. Quantum Electron. **28**(11), 2619 (1992).

[140] B.M. Walsh, N.P. Barnes, B. Di Bartolo, "Branching ratios, cross sections, and radiative lifetimes of rare earth ions in solids: Application to Tm^{3+} and Ho^{3+} ions in $LiYF_4$," J. Appl. Phys. **83**(5), 2772 (1998).

[141] D.Y. Shen, A. Abdolvand, L.J. Cooper, W.A. Clarkson, "Efficient Ho: YAG laser pumped by a cladding-pumped tunable Tm: silica- fibre laser," Appl. Phys. B **79**, 559 (2004).

[142] E. Lippert, S. Nicolas, G. Arisholm, K. Stenersen, G. Rustad, "Mid-infrared laser source with high power and beam quality," Appl. Opt. **45**, 3839 (2006).

[143] A. Dergachev, D. Armstrong, A. Smith, T. Drake, M. Dubois, "3.4-μm ZGP RISTRA nanosecond optical parametric oscillator pumped by a 2.05-μm Ho:YLF MOPA system," Opt. Express **15**, 14404 (2007).

[144] W. Koen, C. Bollig, H. Strauss, M. Schellhorn, C. Jacobs, M.J.D Esser, "Compact fibre-laser-pumped Ho:YLF oscillator-amplifier system," Appl. Phys. B, **99**(1-2), 101 (2009).

[145] P. Malevich, G. Andriukaitis, T. Flöry, A. J. Verhoef, A. Fernández, S. Ališauskas, A. Pugžlys, A. Baltuška, L. H. Tan, C. F. Chua, P. B. Phua, "High energy and average power femtosecond laser for driving mid-infrared optical parametric amplifiers," Opt. Lett. **38**, 2746 (2013).

[146] H. Fonnum, E. Lippert, M. W. Haakestad, "550 mJ Q-switched cryogenic Ho:YLF oscillator pumped with a 100 W Tm:fiber laser," Opt. Lett. **38**, 1884 (2013).

[147] L. von Grafenstein, M. Bock, D. Ueberschaer, U. Griebner, T. Elsaesser, "Ho:YLF chirped pulse amplification at kilohertz repetition rates - 4.3 ps pulses at 2 μm with GW peak power," Opt. Lett. **41**, 4668 (2016).

[148] M. Hinkelmann, D. Wandt, U. Morgner, J. Neumann, D. Kracht, "High repetition rate, μJ-level, CPA-free ultrashort pulse multipass amplifier based on Ho:YLF," Opt. Express **26**, 18125 (2018).

[149] M. Hemmer, D. Sánchez, M. Jelínek, Vadim Smirnov, H. Jelinkova, V. Kubeek, J. Biegert, "2 μm wavelength, high-energy Ho:YLF chirped-pulse amplifier for mid-infrared OPCPA," Opt. Lett. **40**, 451 (2015).

[150] B. Walsh, "Review of Tm and Ho materials; Spectroscopy and lasers," Laser Physics **19**, 855 (2009).

[151] G. P. Frith, D. G. Lancaster, "Power scalable and efficient 790 nm pumped Tm-doped fiber lasers," Proc. SPIE **6102**, 610208 (2006).

[152] E. Slobodtchikov, P. F. Moulton, and G. Frith, "Efficient, High-Power, Tm-doped Silica Fiber Laser," in Advanced Solid-State Photonics, OSA Technical Digest Series (CD) (OSA, 2007), paper MF2.

[153] N. P. Barnes, E. D. Filer, C. A. Morrison, C. J. Lee, "Ho:Tm lasers I: Theoretical," IEEE J. Quantum Electr. **32**, 92 (1996).

[154] C. J. Lee, G. Han, and N. P. Barnes, "Ho:Tm lasers II: Experiments," IEEE J. Quantum Electron. **32**, 104 (1996).

[155] M. Jelínek, V. Kubecek, W. Ma, B. Zhao, D. Jiang, L. Su, "Cryogenic Ho:CaF_2 laser pumped by Tm:fiber laser," Laser Phys. Lett. **13**(6), 065004 (2016).

[156] M. Nemec, J. Šulc, M. Jelínek, V. Kubecek, H. Jelínková, M. E. Doroshenko, O. K. Alimov, V. A. Konyushkin, A. N. Nakladov, V. V. Osiko, "Thulium fiber pumped tunable Ho:CaF_2 laser," Opt. Lett. **42**, 1852 (2017).

[157] W. T. Silfvast, "Laser Fundamentals," Second Edition, Cambridge University Press (1999).

[158] W. Koechner, "Solid-State Laser Engineering," Springer Series in Optical Sciences (1999).

[159] J. Dörring, A. Killi, U. Morgner, A. Lang, M. Lederer, D. Kopf, "Period doubling and deterministic chaos in continuously pumped regenerative amplifiers," Opt. Express **12**, 1759 (2004).

[160] M. Grishin, V. Gulbinas, A. Michailovas, "Bifurcation suppression for stability improvement in Nd:YVO_4 regenerative amplifier," Opt. Express **17**, 15700 (2009).

[161] P. Kroetz, A. Ruehl, G. Chatterjee, A. Calendron, K. Murari, H. Cankaya, P. Li, F. X. Kärtner, I. Hartl, R. J. D. Miller, "Overcoming bifurcation instability in high-repetition-rate Ho:YLF regenerative amplifiers," Opt. Lett. **40**, 5427 (2015).

[162] P. Kroetz, A. Ruehl A.L. Calendron, G. Chatterjee, H. Cankaya, K. Murari, F. X. Kärtner, I. Hartl, R. J. D. Miller, "Study on laser characteristics of Ho:YLF regenerative amplifiers: Operation regimes, gain dynamics, and highly stable operation points," Applied Physics B: Lasers and Optics, **123**(4) 1 (2017).

[163] L. von Grafenstein, M. Bock, U. Griebner, "Bifurcation Analysis in High Repetition Rate Regenerative Amplifiers," IEEE Journal of Selected Topics in Quantum Electronics, **24**(5), 1 (2018).

[164] T. Y. Fan, D. J. Ripin, R. L. Aggarwal, J. R. Ochoa, B. Chann, M. Tilleman, J. Spitzberg, "Cryogenic Yb^{3+}-Doped Solid-State Lasers," IEEE J. Sel. Top. Quantum Electron. **13**, 448 (2007).

[165] M. Ganija, A. Hemming, N. Simakov, K. Boyd, J. Haub, P. Veitch, J. Munch, "High power cryogenic Ho:YAG laser," Opt. Express **25**, 31889 (2017).

[166] F. J. McClung, R. W. Hellwarth, "Giant optical pulsations from ruby", J. Appl. Phys. **33** (3), 828 (1962).

[167] L. E. Hargrove, R. L. Fork, M. A. Pollack, "Locking of He-Ne laser modes induced by synchronous intracavity modulation", Appl. Phys. Lett. **5**, 4 (1964).

[168] E. B. Treacy, "Optical Pulse Compression With Diffraction Gratings," IEEE Journal of Quantum Electronics **5** (1969).

[169] R. L. Fork, O. E. Martinez, and J. P. Gordon, "Negative dispersion using pairs of prisms," Opt. Lett. **9** (1984).

[170] D. Strickland, and G. Mourou, "Compression of amplified chirped optical pulses," Opt. Commun. **55** (1985).

[171] P. F. Moulton, "Spectroscopic and laser characteristics of Ti:Al_2O_3," J. Opt. Soc. Am. B **3**, 125 (1986).

[172] G. Vaillancourt, T. B. Norris, J. S. Coe, P. Bado, G. A. Mourou, "Operation of a 1 kHz pulse-pumped Ti:Sapphire regenerative amplifier," Opt. Lett. **15**, 317 (1990).

[173] K. Yamakawa, H. Shiraga, Y. Kato, C. P. J. Barty, "Prepulse-free 30-TW, 1-ps Nd:glass laser," Opt. Lett. **16**, 1593 (1991).

[174] A. Sullivan, H. Hamster, H. C. Kapteyn, S. Gordon, W. White, H. Nathel, R. J. Blair, R. W. Falcone, "Multiterawatt, 100-fs laser," Opt. Lett. **16**, 1406 (1991).

[175] T. Ditmire, M. D. Perry, "Terawatt Cr:LiSrAlF_6 laser system," Opt. Lett. **18**, 426 (1993).

[176] M. Perry, "Crossing the petawatt threshold," Sci. Tech. Rev. **12**, 4 (1996).

[177] C. P. J. Barty, G. Korn, F. Raksi, C. Rose-Petruck, J. Squier, A.-C. Tien, K. R. Wilson, V. V. Yakovlev, K. Yamakawa, "Regenerative pulse shaping and amplification of ultrabroadband optical pulses," Opt. Lett. **21**(3), 219 (1996).

[178] K. Yamakawa, M. Aoyama, S. Matsuoka, H. Takuma, C. P. J. Barty, D. Fittinghoff, "Generation of 16-fs, 10-TW pulses at a 10-Hz repetition rate with efficient Ti:sapphire amplifiers," Opt. Lett. **23**, 525-527 (1998).

[179] U. Buenting, H. Sayinc, D. Wandt, U. Morgner, D. Kracht, "Regenerative thin disk amplifier with combined gain spectra producing 500 μJ sub 200 fs pulses," Opt. Express **17**(10), 8046 (2009).

[180] Norman M. Kroll, "Parametric Amplification in Spatially Extended Media and Application to the Design of Tuneable Oscillators at Optical Frequencies," Phys. Rev. **127**(4), 1207 (1962).

[181] C. C. Wang, G. W. Racette, "Measurement of parametric gain accompanying optical difference frequency generation," Appl. Phys. Lett. **6**(8), 169 (1965).

[182] I. Ross, P. Matousek, M. Towrie, A. Langley, J. Collier, "The prospects for ultrashort pulse duration and ultrahigh intensity using optical parametric chirped pulse amplifiers," Opt. Commun. **144**, 125 (1997).

[183] O. D. Mücke, D. Sidorov, P. Dombi, A. Pugžlys, S. Ališauskas, V. Smilgeviius, N. Forget, J. Posius, L. Gininas, R. Danielius, A. Baltuška, "10-mJ optically synchronized CEP-stable chirped parametric amplifier at 1.5 μm ", Opt. Spectrosc **108**, 456 (2010).

[184] R. Riedel, A. Stephanides, M. J. Prandolini, B. Gronloh, B. Jungbluth, T. Mans, F. Tavella, "Power scaling of supercontinuum seeded megahertz-repetition rate optical parametric chirped pulse amplifiers," Opt. Lett. **39**, 1422 (2014).

[185] S. E. Irvine, P. Dombi, Gy. Farkas, A. Y. Elezzabi, "Influence of the Carrier-Envelope Phase of Few-Cycle Pulses on Ponderomotive Surface-Plasmon Electron Acceleration," Phys. Rev. Lett. **97**(14) (2006).

[186] A. Apolonski, P. Dombi, G. G. Paulus, M. Kakehata, R. Holzwarth, Th. Udem, Ch. Lemell, K. Torizuka, J. Burgdorfer, T.W. Hansch, F. Krausz, "Observation of Light-Phase-Sensitive Photoemission from a Metal," Phys. Rev. Lett." **92**(7), 073902 (2004).

[187] A. Baltuska, T. Fuji, T. Kobayashi, "Controlling the Carrier-Envelope Phase of Ultrashort Light Pulses with Optical Parametric Amplifiers," Phys. Rev. Lett. **88**, 133901 (2002).